NAVAL POSTGRADUATE SCHOOL

MONTEREY, CALIFORNIA

THESIS

TWO-SENSOR SYNTHETIC APERTURE GEOLOCATION TECHNIQUES

by

Kyle A. Elam

June 2014

Thesis Advisor:	Weilian Su
Second Reader:	Tri Ha

Approved for public release; distribution is unlimited

REPORT DOCUMENTATION PAGE	*Form Approved OMB No. 0704–0188*

1. AGENCY USE ONLY *(Leave blank)*	**2. REPORT DATE** June 2014	**3. REPORT TYPE AND DATES COVERED** Master's Thesis

4. TITLE AND SUBTITLE TWO-SENSOR SYNTHETIC APERTURE GEOLOCATION TECHNIQUES	**5. FUNDING NUMBERS**
6. AUTHOR(S) Kyle A. Elam	
7. PERFORMING ORGANIZATION NAME(S) AND ADDRESS(ES) Naval Postgraduate School Monterey, CA 93943–5000	**8. PERFORMING ORGANIZATION REPORT NUMBER**
9. SPONSORING /MONITORING AGENCY NAME(S) AND ADDRESS(ES) N/A	**10. SPONSORING/MONITORING AGENCY REPORT NUMBER**

11. SUPPLEMENTARY NOTES The views expressed in this thesis are those of the author and do not reflect the official policy or position of the Department of Defense or the U.S. Government. IRB Protocol number ____N/A____.

12a. DISTRIBUTION / AVAILABILITY STATEMENT Approved for public release; distribution is unlimited	**12b. DISTRIBUTION CODE**

13. ABSTRACT (maximum 200 words)

Geolocation technology with the ability to locate an unknown beacon signal in three-dimensional space has been engrafted into numerous modern electronic systems. Indeed, the marketplace is anxious for more accurate and more accessible geolocation data. A primary limiting factor of the growth of geolocation systems is the stringent physical resource requirements needed for existing geolocation algorithms.

Popular geolocation algorithms measure the time-of-arrival, time-difference-of-arrival, and frequency-difference-of-arrival of an incoming beacon signal from an unknown emitter at a given time. For these techniques, accurate solutions require a minimum of three airborne sensors; if available, a fourth sensor often significantly improves the accuracy. This resource requirement is excessive; we aim to relax it to two airborne sensors by applying a synthetic aperture technique. By fusing together data from multiple subsequent time samples, one can boost the overall resolution of the geolocation estimate.

We propose using a series of geolocation measurements collected between two sensors according to a synthetic aperture model. System performance dependence on sensor velocity and aperture size is assessed. Additionally, a brief treatment of noise tolerance and estimation theory is given. Lastly, the overall feasibility of a synthetic-aperture-based geolocation algorithm is summarily addressed.

14. SUBJECT TERMS Geolocation, time-of-arrival, time-difference-of-arrival, frequency-difference-of-arrival, synthetic aperture, data fusion, estimation	**15. NUMBER OF PAGES** 125
	16. PRICE CODE

17. SECURITY CLASSIFICATION OF REPORT Unclassified	**18. SECURITY CLASSIFICATION OF THIS PAGE** Unclassified	**19. SECURITY CLASSIFICATION OF ABSTRACT** Unclassified	**20. LIMITATION OF ABSTRACT** UU

NSN 7540–01–280–5500

Standard Form 298 (Rev. 2–89)
Prescribed by ANSI Std. 239–18

THIS PAGE INTENTIONALLY LEFT BLANK

TWO-SENSOR SYNTHETIC APERTURE GEOLOCATION TECHNIQUES

Kyle A. Elam
Ensign, United States Navy
B.S., United States Naval Academy, 2013

Submitted in partial fulfillment of the
requirements for the degree of

MASTER OF SCIENCE IN ELECTRICAL ENGINEERING

from the

NAVAL POSTGRADUATE SCHOOL
June 2014

Author:	Kyle A. Elam
Approved by:	Weilian Su Thesis Advisor
	Tri Ha Second Reader
	Clark Robertson Chair, Department of Electrical and Computer Engineering

THIS PAGE INTENTIONALLY LEFT BLANK

ABSTRACT

Geolocation technology with the ability to locate an unknown beacon signal in three-dimensional space has been engrafted into numerous modern electronic systems. Indeed, the marketplace is anxious for more accurate and more accessible geolocation data. A primary limiting factor of the growth of geolocation systems is the stringent physical resource requirements needed for existing geolocation algorithms.

Popular geolocation algorithms measure the time-of-arrival, time-difference-of-arrival, and frequency-difference-of-arrival of an incoming beacon signal from an unknown emitter at a given time. For these techniques, accurate solutions require a minimum of three airborne sensors; if available, a fourth sensor often significantly improves the accuracy. This resource requirement is excessive; we aim to relax it to two airborne sensors by applying a synthetic aperture technique. By fusing together data from multiple subsequent time samples, one can boost the overall resolution of the geolocation estimate.

We propose using a series of geolocation measurements collected between two sensors according to a synthetic aperture model. System performance dependence on sensor velocity and aperture size is assessed. Additionally, a brief treatment of noise tolerance and estimation theory is given. Lastly, the overall feasibility of a synthetic-aperture-based geolocation algorithm is summarily addressed.

THIS PAGE INTENTIONALLY LEFT BLANK

TABLE OF CONTENTS

LIST OF FIGURES

LIST OF TABLES

THIS PAGE INTENTIONALLY LEFT BLANK

LIST OF ACRONYMS AND ABBREVIATIONS

AOA	angle-of-arrival
CCMC	community coordinated modeling center
CEM	computational electromagnetic
CRLB	Cramér-Rao lower bound
EKF	extended Kalman filter
EM	electromagnetic
FDOA	frequency-difference-of-arrival
FOV	field-of-view
GAIM	global assimilation of ionospheric measurements
GMM	Gaussian mixture measurement
GNSS	global navigation satellite system
GPS	global positioning system
IID	independent and identically distributed
ISM	industrial, scientific, and medical
LOS	line-of-sight
LS	least-squares
ML	maximum-likelihood
MSE	mean-square error
PDF	probability density function
RF	radio frequency
RMS	root-mean-square
RMSE	root-mean-square error
SAR	synthetic aperture radar
SAS	synthetic aperture sonar
TDOA	time-difference-of-arrival
TOA	time-of-arrival
UAV	unmanned aerial vehicle
UKF	unscented Kalman filter

THIS PAGE INTENTIONALLY LEFT BLANK

EXECUTIVE SUMMARY

In recent years, the number of electronic systems using geolocation data has proliferated. A wide variety of growing applications is driving researchers to consider methods of extending coverage areas and boosting spatial resolution. Commonly used geolocation algorithms, including time-of-arrival (TOA), time-difference-of-arrival (TDOA), and frequency-difference-of-arrival (FDOA), require numerous airborne sensors—whether a constellation of satellites or a temporary network of aircraft—to deliver accurate results. In regions of operation with limited aerial view, such as canyons and valleys, it may be difficult to establish a line-of-sight communications link with many airborne sensors. The main research goal of this work is to reduce the number of required airborne sensors for accurate geolocation to two sensors. We seek to accomplish this using a synthetic aperture technique to combine subsequent geolocation measurements in time and develop a refined geolocation estimate.

To lay an initial theoretical framework, we first consider the two- and three-dimensional solutions for the three primary algorithms under consideration: TOA, TDOA, and FDOA. The associated solution curves or surfaces are presented and discussed. To model these algorithms as random processes, we also introduce and define time- and frequency-domain noise models for various cases based on the sensor altitudes. For satellite-based sensors, we consider the effects of signal propagation through the ionosphere and the associated time delay and Doppler shift variations. For lower-altitude sensors onboard an unmanned aerial vehicle (UAV), we consider the time delay characteristics of lower-atmospheric propagation. For each scenario, an additive noise model is defined for TOA, TDOA, and FDOA measurements.

The main thrust of our work is directed toward the implementation of a synthetic aperture algorithm with a two-sensor system. Accordingly, we first propose a homogeneous synthetic aperture TOA algorithm. It is considered homogeneous since both geolocation measurements collected at a given time step in the synthetic aperture are TOA measurements; there is only one type of measurement included in the algorithm. With TOA, we may collect one measurement per sensor in the network. In this case, we

collect two TOA measurements per time step. Using a synthetic aperture of length N, we systematically combine pairs of TOA measurements from subsequent time steps t_n and t_{n+1}. When the full duration of the synthetic aperture has passed, a refined estimate of the unknown emitter position is generated. Our numerical results for the synthetic aperture TOA algorithm show that, for accurate usage in a satellite-sensor system, future implementations will need to incorporate some noise mitigation techniques to improve the geolocation accuracy to useful levels. For UAV-based systems at altitude 10,000 feet, the results are more promising. Especially in low-noise scenarios, root-mean-square (RMS) estimation errors as low as 12.0 meters are achieved using the synthetic aperture technique. On the whole, we find that estimation error decreases as the number of synthetic aperture samples N increases; however, there is a diminishing return for large N as the RMS error asymptotically approaches zero meters. In such UAV-based systems, the synthetic aperture TOA algorithm is very promising.

The second synthetic aperture algorithm we propose is a heterogeneous combination of one TDOA and one FDOA measurement at each time step in the aperture. For both the TDOA and FDOA geolocation techniques, we may collect one measurement per two sensors; thus, with two sensors, we have one TDOA and one FDOA measurement available at a given point in time. We again apply the synthetic aperture concept to synthesize data collected at subsequent steps in time and generate a refined geolocation estimate. A result of the complexity of the FDOA equation, we do not attempt an analytical solution to the TDOA-FDOA fusion problem and instead consider an iterative numerical solution. Our results for various conditions show that our proposed algorithm was limited by the excessive computational demands of our solution strategy. An iterative search through three-dimensional space scales as $O\left(K^3\right)$, where K is the number of discrete points in each dimension and $O\left(\cdot\right)$ represents traditional big O notation. We are limited in our ability to adequately sample the region of interest. Accordingly, the Nyquist sampling criterion bounds our ability to discern high-resolution spatial information.

Future implementations of a heterogeneous synthetic aperture TDOA-FDOA fusion algorithm will require reducing computational demand and addressing the Nyquist sampling limitation if it is to be suitable for high-accuracy applications. Some potential improvements to this end are suggested and discussed. Summarily, we find that a synthetic aperture TOA algorithm is both feasible and useful for reducing the physical resource requirement to two sensors for low-altitude UAV-based systems. The more complicated synthetic aperture TDOA-FDOA fusion algorithm will require a more optimized solution strategy to yield high-accuracy results.

THIS PAGE INTENTIONALLY LEFT BLANK

I. INTRODUCTION

A. BACKGROUND MOTIVATION

In recent decades, terrestrial geolocation systems have shifted from the domain of academic research and niche military applications to that of the average household consumer. From the automotive industry to cellular phones, geolocation hardware and algorithms are now embedded onboard many everyday devices. Public access to the Global Positioning System (GPS) infrastructure has largely engrained into the popular mind that GPS is the only prominent geolocation system; however, the general topic of geolocation encompasses a much larger variety of systems, algorithms, and applications than GPS alone. Early competitors to GPS, including LORAN C, GLONASS, OMEGA, and GEOSTAR, all operated based on different geolocation methods and thus reported various performance characteristics [1].

Not all geolocation system applications are conventional or mundane. Researchers in Australia track the locations and frequency of lightning strikes in remote regions to improve wildfire containment strategies [2]. Geolocation data has been used extensively in seismologic research near the San Andreas Fault in California [3]. The E-911 system implemented in 2001 incorporates available GPS data with any proximate cellular infrastructure to offer emergency response services accurate locations of victims in distress [4]. In short, users from the military to the commercial marketplace are investing time and resources into developing geolocation-dependent systems. To support this growing demand, geolocation technologies must continue to progress and innovate. Without a readily available and robust technological infrastructure, geolocation applications may begin to stagnate.

B. GEOLOCATION FUNDAMENTALS

In general, a passive geolocation system consists of three conceptual components: the physical infrastructure, the geolocation measurement method, and the post-processing algorithm. The common physical scenario considered in the literature is that of a network of N airborne sensors with known position and velocity attempting to geolocate a single emitter of unknown position and velocity. The emitter generates an electromagnetic beacon signal that propagates by line-of-sight (LOS) transmission to all sensors in view. Depending on the measurement method implemented by the system designers, the emitter and sensors may or may not be synchronized in time. The sensors may be satellites at various orbital altitudes or, as is the more recent trend in small-scale portable systems, the sensors may be unmanned aerial vehicles (UAVs).

A variety of geolocation measurement methods are available, depending on system constraints. Angle-of-arrival (AOA) techniques use spatially-sensitive antenna arrays onboard each sensor to determine the direction from which an incoming signal arrives. With sufficient angular measurements, the sensors can determine the emitter location. The AOA method has largely been set aside in favor of others due to the complex array design necessary to achieve high angular resolution [5]. Time-of-arrival (TOA) techniques compute the absolute propagation time of the beacon signal from the emitter to each distinct sensor. From the propagation time, the distance from the emitter to each sensor is known; the emitter position can then be solved geometrically [6]. The GPS system employs the TOA measurement method [5]. Time-difference-of-arrival (TDOA) techniques compute the temporal difference between the beacon signal's arrival time at multiple sensors. Here, no information is required of the emitter's timing information; only the difference in arrival time between two sensors is of concern. Solving the TDOA measurement equation in three dimensions is more computationally intensive than AOA or TOA, but less a priori information is required of the emitter in order to geolocate [7]. Perhaps the most complicated method presented in this overview, the frequency-difference-of-arrival (FDOA) technique computes the emitter position based on the Doppler shifts seen at each individual sensor. Because of its Doppler dependency, the FDOA method requires some relative radial movement between the emitter and at least one sensor [8]. To be sure, other geolocation measurement methods exist, but the four discussed above cover a sufficiently wide topical breadth to suffice for introductory purposes.

Much of the accuracy of the geolocation system can be attributed to the post-processing algorithms run following the measurement collection. There are typically two stages of processing. First, an estimator algorithm fuses all the noisy measurements together and determines the best estimate of emitter position. For a noise-free environment, all measurements would coincide at a single spatial coordinate and estimation is unnecessary, as an exact solution is available. Unfortunately, all real implementations of geolocation systems suffer signal corruption due to noise. Resolving the measurement inconsistencies is traditionally done using one of two classes of estimators: least-squares (LS) estimators and maximum-likelihood (ML) estimators [7]. Each has its advantages and disadvantages, depending on the system specifics. Second, a tracking algorithm constructs predictions of future emitter position and velocity based on past measurement and estimation data. Many tracking filters have been presented in the literature, but two seem to have been established as field standards. The Extended Kalman Filter (EKF) attempts to linearize nonlinear measurements using Taylor expansions. For mild circumstances, the EKF works well in tracking applications; however, if the pertinent geolocation equations become severely nonlinear, EKF performance diminishes rapidly [9]. In response to some of the shortcomings of the EKF, the Unscented Kalman Filter (UKF) was developed as an alternative to avoid some of those linearization issues [9]. Other tracking filters have been proposed, to include various particle filters (see [10] and [11] for further discussion) and the Gaussian Mixture Measurement (GMM) filter [8]; however, one of the simpler Kalman Filter designs is often the more popular choice.

C. RESEARCH GOAL

Regardless of the specific geolocation method used, it is a general rule that N available sensors only allow geolocation in N-dimensional space with any degree of accuracy. So, in three dimensions, a constellation of at least three airborne sensors performing geolocation calculations is required to locate an unknown emitter. A system with only three sensors is said to be critically-determined. Many estimators allow for—or even prefer—more than three measurements in order to increase accuracy and spatial resolution; this is an over-determined condition. Alternatively, assumptions may be made about the physical environment; assuming a known emitter altitude, for instance, narrows the three-dimensional search to two dimensions, namely the horizontal plane at the known altitude. This, in turn, relaxes the requirement on number of measurements and sensors [12].

For many conventional operating scenarios, the minimum resource requirement of three visible airborne sensors is a nonissue. Often either geographic landscapes offer a sufficiently wide aerial field-of-view (FOV) to accommodate LOS transmissions with three or more sensors, or the end user is willing to suffer gaps in geolocation coverage areas. Accordingly, little effort to date has been directed toward assessing techniques to relax the resource requirement; however, it is not difficult to imagine a situation where the three-sensor requirement is unacceptable. For instance, one can easily imagine an urgent search and rescue application that demands accurate geolocation fixes in mountainous terrain with limited FOV and limited sensor availability. Currently, when a system is below this critically-determined threshold, it will fail to provide geolocation information with any helpful degree of accuracy; until the resource requirement can be met, the emitter must bear the burden of estimating its own position. Depending on the application, local onboard solutions may be available. For instance, automobile navigation systems couple inertial sensor data and accurate road maps to help interpolate an automobile's position between intermittent GPS fixes. The inertial sensors provide information on course changes, while the road maps restrict possible vehicle movements along known paths. Together with recent GPS data, this additional local information helps offer a seamless position estimate in real time [13]. Still, if size and power requirements for the emitter are strict, inertial sensor suites and significant onboard processing power is an excessive demand. Rather than push the requirement complexity from the sensors to the end user's emitter, a new accurate geolocation technique with only two required airborne sensors is preferable.

In 2007, Fletcher, Ristic, and Musicki proposed using the TDOA measurements from only two moving UAVs to geolocate an emitter [14]. They proposed a recursive estimator, which updates the estimated emitter position following each successive measurement rather than entirely recalculating the emitter position based on previous measurement history. They examined both the EKF and UKF as potential tracking algorithms for both a stationary and moving emitter. Each filter performed accurately and converged on the Cramér-Rao Lower Bound (CRLB)—the theoretical lower limit for mean-squared error (MSE) of any unbiased estimator [14]. Their result introduced a new concept in reducing the physical resource requirement for accurate geolocation. One can substitute temporal resources for physical resources. An under-determined network of sensors might be able to geolocate an emitter by fusing together a series of successive measurements in time. Moreover, each additional measurement may be incorporated to improve the spatial resolution of the algorithm. This functional concept has been implemented for years by synthetic aperture radars (SAR), which combine many successive returns from a low-resolution radar to generate a very high-resolution image. As with SAR, each successive measurement increases the accuracy of the estimated emitter position.

It should be noted that Fletcher, Ristic, and Musicki collected one TDOA measurement per time step [14]. This homogeneous measurement technique may have advantages in computational efficiency, but it is possible to extract more measurement data from the two available sensors. In this research, we propose and investigate a two-sensor geolocation algorithm that collects at each time step one TDOA measurement and one FDOA measurement. This heterogeneous technique fuses together the TDOA and FDOA measurement types. Incorporating FDOA computations undoubtedly increases the complexity of the solution approach and raises the demand for processing power; nevertheless, doubling the number of measurements per time period may offer worthwhile improvement in overall accuracy. As a preliminary step toward pursuing the TDOA/FDOA data fusion, we first consider the simpler case of fusing together two TOA measurements as a proof of concept.

THIS PAGE INTENTIONALLY LEFT BLANK

II. TIME-OF-ARRIVAL

A. GOVERNING EQUATION

On the heels of the widespread success of GPS, TOA-based geolocation algorithms have risen in prominence. The solution method is simple when compared with methods such as TDOA and FDOA. Still, achieving simplicity in an algorithm often demands more numerous or detailed algorithm inputs. One key aspect of the TOA algorithm is that absolute timing information is necessary. Namely, when each individual sensor i receives the emitter signal, it must be able to determine the absolute one-way signal propagation time. This is the TOA measurement τ_i. Multiplying by the propagation speed c_0, we relate propagation time to the range between the emitter and sensor i. Assuming a noise-free environment and a constellation of N TOA sensors, the emitter position must fall within the set of all points that satisfy

$$\left\|\boldsymbol{r}_e - \boldsymbol{r}_i\right\| = \left\|\boldsymbol{r}_{ei}\right\| = c_0\tau_i, \quad i = 1, 2, \ldots, N, \tag{1}$$

where $\boldsymbol{r}_e$ and $\boldsymbol{r}_i$ are the range vectors from the coordinate system origin to the emitter and to sensor i, respectively. The vector $\boldsymbol{r}_{ei}$ is simply the difference between vectors $\boldsymbol{r}_e$ and $\boldsymbol{r}_i$. Unless specified otherwise, bold-faced font hereafter indicates a vector. Additionally, the $\left\|\cdot\right\|$ operator hereafter denotes the Euclidean norm of a vector.

B. TWO-DIMENSIONAL SOLUTION

Consider a two-dimensional scenario as depicted in Figure 1. The two sensors labeled s_1 and s_2 attempt to geolocate an emitter of unknown position labeled e. In this TOA geolocation scenario, there are no restrictions on sensor or emitter movement. The specific choices of sensor position, emitter position, and units are arbitrary, so convenient values are chosen for presentation's sake. The sensors are located at the known Cartesian coordinates $(-5, 0)$ km and $(5, 0)$ km; the unknown emitter is located at $(1, 7)$ km.

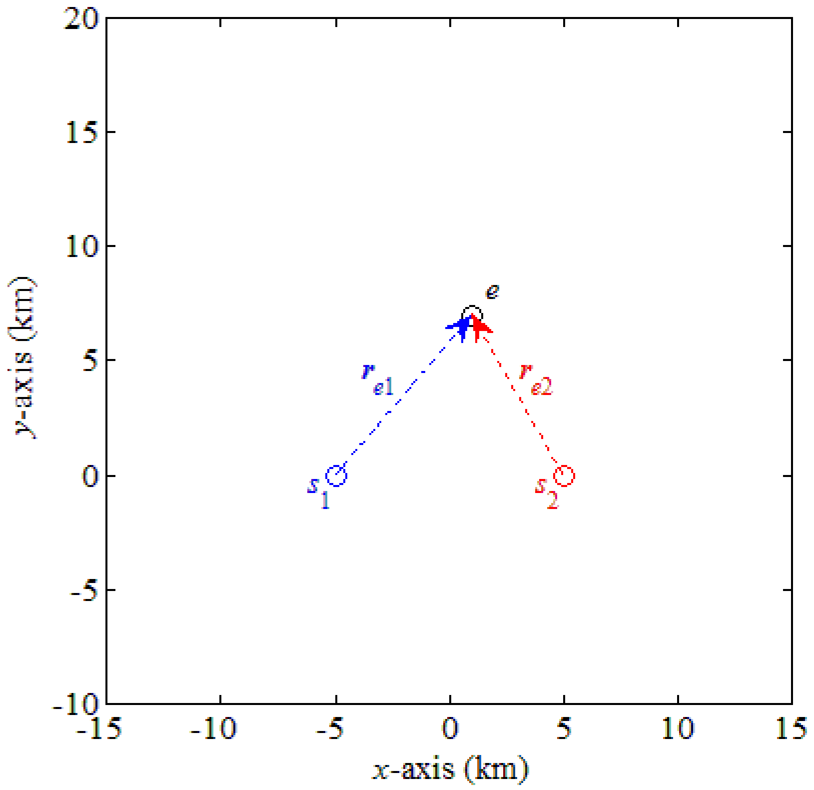

Figure 1. Two TOA sensors s_1 and s_2 attempt to locate an emitter of unknown position.

As in the general case for TOA geolocation, the emitter generates an omnidirectional beacon signal that propagates toward each sensor. Upon signal arrival, each sensor determines the total transmission time of the signal from emitter to that respective sensor. The TOA measurement collected by sensor s_i in turn gives the radial range $c_0\tau_i$ to the emitter position. This restricts the emitter position to the set of all points on the circle with radius $c_0\tau_i$ and centered at the corresponding sensor. This circle may be referred to as a constant-TOA curve; an emitter located at any point on the curve generates the same TOA measurement value at sensor s_i.

For the two-sensor scenario ($N = 2$), the resultant circular emitter position curves are shown in Figure 2. Encouragingly, both circles intersect at the emitter location; however, there is a point of ambiguity where both circles intersect at a point other than the emitter location. As such, even in two-dimensional space, two TOA measurements alone are insufficient to unambiguously locate the emitter. More measurements are required to give a singular solution.

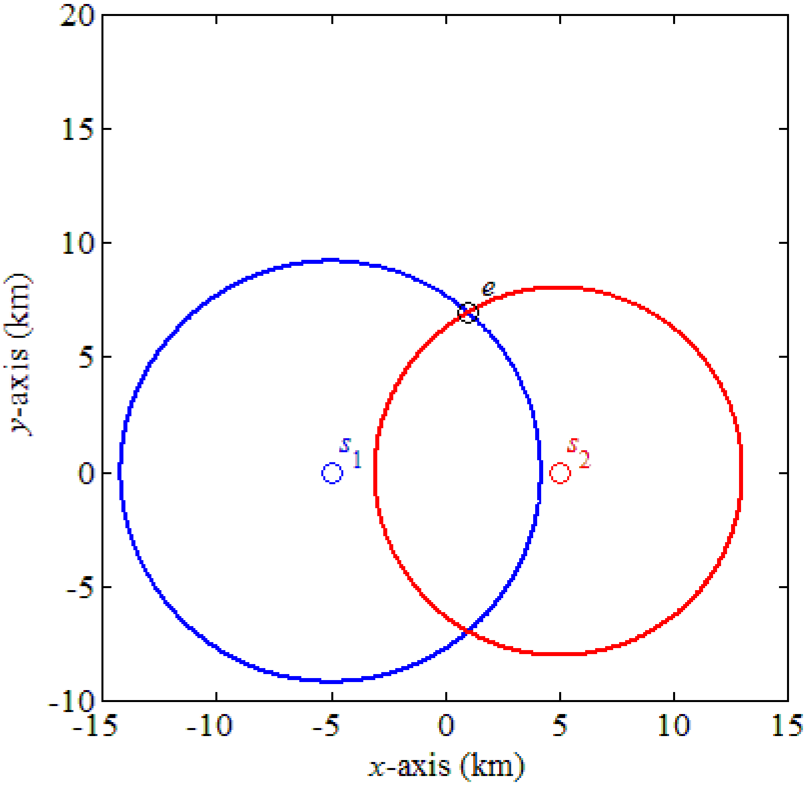

Figure 2. Two TOA emitter position curves are color-coded to match the corresponding sensor.

To solve the ambiguity problem, an additional sensor s_3 is positioned at $(-5,10)$ km and calculates an additional TOA measurement based on the received emitter signal. As with the other sensors, we solve the TOA measurement for the emitter position curve. The additional position circle from sensor s_3 is shown in Figure 3 atop the previous measurements from sensors s_1 and s_2.

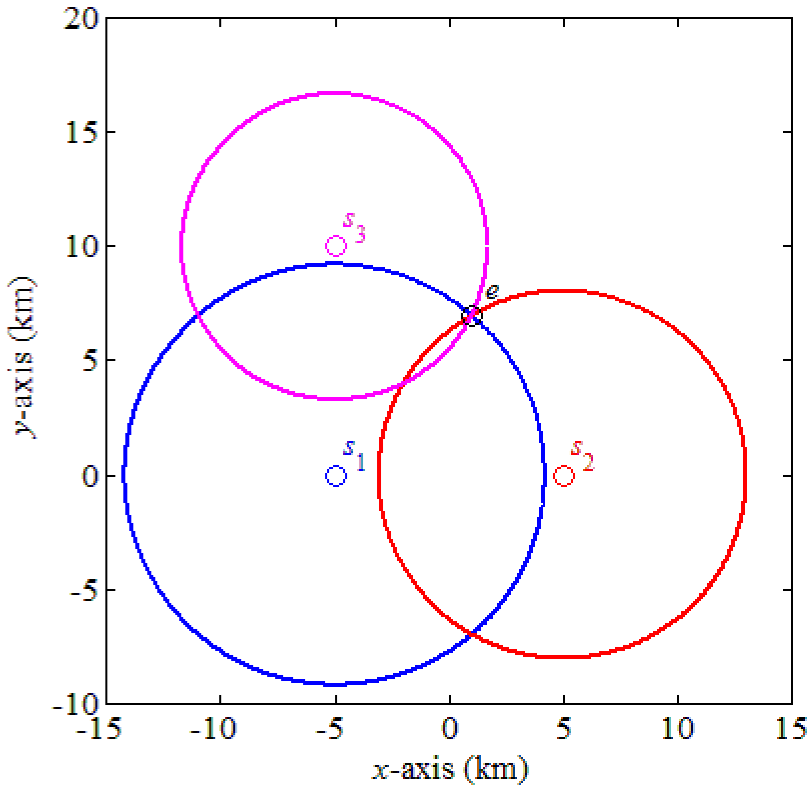

Figure 3. Three TOA emitter position curves unambiguously geolocate the unknown emitter.

Here, the third sensor has resolved the ambiguity issue. There are still multiple points where two of the three position curves intersect, but there is only one single location where each position curve intersects all others. So, with three sensors we have accurately and unambiguously located the unknown emitter in a two-dimensional, noiseless environment using circular TOA measurements.

Still, even without noise corruption, there are situations in which no number of TOA sensors can unambiguously located an emitter. Consider the scenario wherein sensor s_3 is placed at $(0,0)$ km and calculates a TOA measurement as expected. The resulting emitter position curves are plotted in Figure 4.

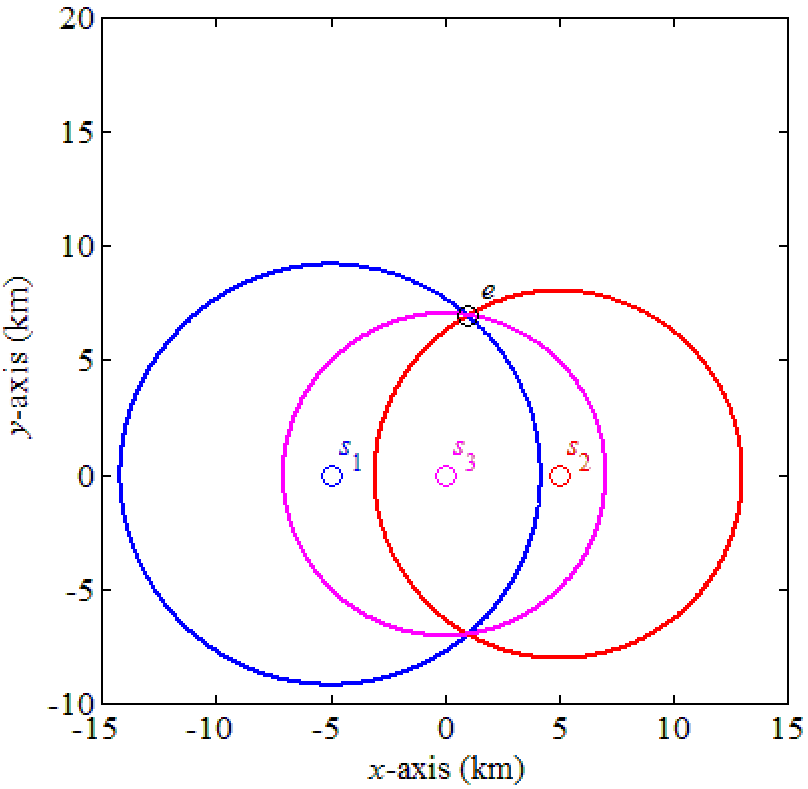

Figure 4. Three TOA emitter position curves unsuccessfully attempt to resolve emitter location ambiguity.

Clearly, the addition of the third sensor does not resolve points of ambiguity under all circumstances. In fact, for any collinear arrangement of TOA sensors, we are always left with an ambiguous solution, irrespective of the number of sensors present. This is a point of great concern; the physical arrangement of geolocation sensors can have a severe impact on the performance and capability of the geolocation system. Moving forward, it is important to characterize the capabilities of various geolocation techniques with respect to physical orientation and movement of the sensor constellation.

C. THREE-DIMENSIONAL SOLUTION

Extension of the TOA solution to three dimensions is not complicated. Rather than a two-dimensional circle, the solution to Equation 1 is now a sphere centered around the i-th sensor position with radius $c_0\tau_i$. The emitter's unknown position is necessarily restricted to the set of points lying on the resultant spherical TOA surface. A second TOA measurement generates another spherical emitter surface. In general, the intersection of any two spheres is either a single point or a circle. If the spheres intersect tangentially, there will be only a single point of intersection, but this condition is effectively a theoretical singularity that does not occur in practice. Alternatively, two spheres may intersect to form a circular intersection curve. This principle is illustrated in Figure 5.

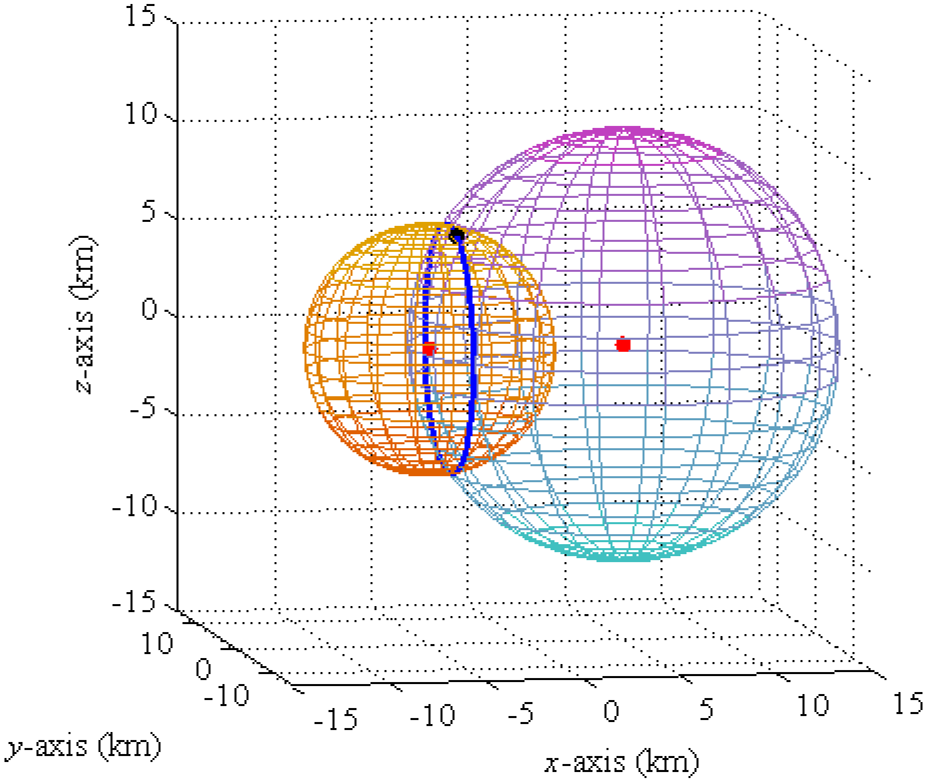

Figure 5. Two TOA emitter position surfaces restrict the potential emitter location to a circular curve.

Here, two arbitrarily positioned TOA sensors are placed at the Cartesian coordinates $(-5,0,0)$ km and $(5,0,0)$ km and depicted as red markers. The emitter is located at $(-4,-2,6)$ km and depicted as a black marker. The sensors receive the TOA beacon signal and calculate the associated spherical emitter surfaces. The circular intersection of the two spheres is shown as a dark blue curve. Here, since the TOA sensors are both located directly on the *x*-axis, the circular intersection curve is contained in a vertical plane perpendicular to the *x*-axis. In fact, for the two-sensor condition, the circular intersection curve is always contained within a plane perpendicular to the sensor axis, regardless of sensor orientation. Notice further that combining two TOA sensor measurements effectively brings us back to a two-dimensional scenario as discussed previously. It follows, then, that an additional TOA sensor positioned away from the existing sensor axis further restricts the emitter position to two potential points. Finally, a fourth TOA sensor positioned away from all existing sensor axes solves for the unambiguous emitter position at a single three-dimensional coordinate. We add the caveat that additional sensors are placed away from existing sensor axes to avoid the insoluble ambiguity problem that arises from all sensors being placed on the same sensor axis, as discussed previously. Altogether, extension of the TOA solution method into a third dimension increases the sensor requirement by one sensor in order to preserve the same degree of accuracy.

THIS PAGE INTENTIONALLY LEFT BLANK

III. TIME-DIFFERENCE-OF-ARRIVAL

A. GOVERNING EQUATION

A less restrictive alternative to TOA is TDOA, which does not require knowledge of the absolute propagation time of the emitter's beacon signal. Instead, the TDOA geolocation technique uses highly synchronized clocks onboard all devices in the sensor constellation to monitor the relative difference in arrival time between sensors. Each TDOA emitter position curve or surface is defined as the set of all points satisfying

$$\left\| \boldsymbol{r}_e - \boldsymbol{r}_i \right\| - \left\| \boldsymbol{r}_e - \boldsymbol{r}_j \right\| = c_0 \tau_{ij}, \quad i, j = 1, 2, \ldots, N, \quad i \neq j, \tag{2}$$

where the time-difference-of-arrival measurement given by

$$\tau_{ij} = \left(\tau_i - \tau_0\right) - \left(\tau_j - \tau_0\right) = \tau_i - \tau_j \tag{3}$$

may be defined in reference to the absolute time of transmission τ_0 or simply as the relative difference in arrival time at sensors s_i and s_j , denoted $\tau_i - \tau_j$. Note that the TDOA measurement τ_{ij} may take on any real value, either positive or negative. From the study of analytical conics, recall that the set of all points such that the difference in distance to two foci is constant is a hyperbolic curve [15]. Accordingly, if the problem is cast in two-dimensional space, the particular solution curve for Equation 2 is a hyperbola; if it is cast in three-dimensional space, the particular solution surface for Equation 2 is a hyperboloid of two sheets. Sensors s_i and s_j are located along the major axis of the hyperbola or hyperboloid and function as the hyperbolic foci.

B. TWO-DIMENSIONAL SOLUTION

In the two-dimensional *x*-*y* plane, two sensors of known position attempt to locate the position of an unknown emitter using TDOA measurements. In the following section, sensors s_1 and s_2 are located at the generic Cartesian coordinates $\left(x_1, y_1\right)$ and $\left(x_2, y_2\right)$, respectively. It is again assumed that the environment is noise-free and all measurement values are exact.

In this scenario, the emitter begins transmitting an omnidirectional beacon signal at some unknown time τ_0. This signal arrives at sensor s_1 at time τ_1 and at sensor s_2 at time τ_2. The lack of knowledge of the originating time τ_0 prohibits the use of TOA measurements in this case; however, a TDOA measurement may still be collected. Comparing the difference in signal arrival time at each sensor, we solve (3) for the single TDOA measurement $\tau_{21} = \tau_2 - \tau_1$. With a known TDOA measurement value, we may solve (2) analytically.

The following derivation is an algebraic solution to (2) based on the proof given in [16], with some appropriate modifications. We solve for the set of all Cartesian coordinates (x, y) that satisfy the TDOA measurement. Using the distance formula, we rewrite the TDOA equation

$$\left\|\boldsymbol{r}_e - \boldsymbol{r}_2\right\| - \left\|\boldsymbol{r}_e - \boldsymbol{r}_1\right\| = c_0\tau_{21} \tag{4}$$

as

$$\sqrt{(x-x_2)^2 + (y-y_2)^2} - \sqrt{(x-x_1)^2 + (y-y_1)^2} = c_0\tau_{21}. \tag{5}$$

We next orient our coordinate systems such that sensors s_1 and s_2 are located at the Cartesian coordinates $(-d, 0)$ and $(d, 0)$, respectively. The problem then reduces to

$$\sqrt{(x-d)^2 + y^2} - \sqrt{(x+d)^2 + y^2} = c_0\tau_{21}. \tag{6}$$

Rearranging terms and squaring both sides of the equation gives

$$\left(\sqrt{(x-d)^2 + y^2}\right)^2 = \left(c_0\tau_{21} + \sqrt{(x+d)^2 + y^2}\right)^2. \tag{7}$$

We subsequently expand to get

$$x^2 - 2dx + d^2 + y^2 = (c_0\tau_{21})^2 + 2c_0\tau_{21}\sqrt{x^2 + 2dx + d^2 + y^2} + x^2 + 2dx + d^2 + y^2. \tag{8}$$

Collecting all linear terms and constants on the left-hand side of the equation, we are left with

$$-4dx-\left(c_0\tau_{21}\right)^2=2\left(c_0\tau_{21}\right)\sqrt{x^2+2dx+d^2+y^2}. \tag{9}$$

To condense the notation, we introduce the parameter

$$a=\frac{c_0\tau_{21}}{2}, \tag{10}$$

which carries the same sign as the TDOA measurement τ_{21}. Substituting (10) into (9) gives

$$-dx-a^2=a\sqrt{x^2+2dx+d^2+y^2}. \tag{11}$$

We then square both sides of the equation and expand to get

$$d^2x^2+2da^2x+a^4=a^2\left(x^2+2dx+d^2+y^2\right). \tag{12}$$

Note that the sign information associated with parameter a—and thus the TDOA measurement τ_{21}—is now lost from the squaring operation. We shall revisit this issue below. Collecting terms and factoring leaves

$$\left(d^2-a^2\right)x^2-a^2y^2=a^2\left(d^2-a^2\right). \tag{13}$$

We then divide through by $a^2\left(d^2-a^2\right)$ to give

$$\frac{x^2}{a^2}-\frac{y^2}{d^2-a^2}=1. \tag{14}$$

Introduction of the traditional hyperbolic parameter

$$b=\sqrt{d^2-a^2} \tag{15}$$

into (14) gives the recognizable form of a hyperbola with foci lying along the *x*-axis, namely

$$\frac{x^2}{a^2}-\frac{y^2}{b^2}=1. \tag{16}$$

To recast the hyperbola in terms of quantifiable TDOA parameters, we substitute out the intermediate parameters a and b, given by (10) and (15), respectively, to get

$$\frac{4x^2}{\left(c_0\tau_{21}\right)^2}-\frac{4y^2}{4d^2-\left(c_0\tau_{21}\right)^2}=1. \tag{17}$$

Note that (17) is fully expressed in terms of the spatial Cartesian coordinates (x, y), the known propagation speed c_0, the known spatial parameter d, and the calculated TDOA measurement τ_{21}. Altogether, we have sufficient information to localize the unknown emitter to a two-dimensional hyperbolic curve.

One final point requires discussion. The hyperbolic equation in (17) is satisfied by two branches. Let us term these the positive and negative branches. The positive branch is that half of the hyperbola nearest in space to sensor s_1, and the negative branch is that half nearest in space to sensor s_2. Since spatial distance directly correlates to time delay, we know that an emitter located at any point on the positive branch corresponds to a TDOA measurement $\tau_{21} = \tau_2 - \tau_1 > 0$. Conversely, an emitter located at any point on the negative branch must correspond to $\tau_{21} < 0$. We noted above that the sign information associated with the TDOA measurement τ_{21} was lost in (12) due to the squaring operation. We may now retroactively go back and rule out one of the two hyperbolic branches. In short, choose the single branch that corresponds to the sign of the received TDOA measurement and discard the other branch as an invalid solution.

To illustrate the TDOA solution curve, we consider an example two-sensor TDOA problem depicted in Figure 6. The sensor and emitter positions in Figure 6 are arbitrarily chosen to aid visualization; the sensors s_1 and s_2 are positioned at coordinates $(-5, 0)$ km and $(5, 0)$ km, and the emitter is positioned at the coordinates $(4, 7)$ km. The sensors are unaware of the emitter location prior to the arrival of the TDOA signal.

We assume each sensor has preexisting knowledge of the spatial coordinates of all other sensors in the constellation. From the problem statement, the spatial parameter $d = 5$ km is known. The speed of propagation of the emitter signal is taken to be the free-space value 2.998×10^8 m/s. Assuming ideal LOS signal transmission, the TDOA measurement between sensors s_1 and s_2 upon arrival is $\tau_{21} = \left(\|\boldsymbol{r}_{e2}\| - \|\boldsymbol{r}_{e1}\| \right) / c_0 = -14.44\ \mu\text{s}$. With only knowledge of these three parameters and measurements, the sensors can solve for a particular solution to Equation 17. Figure 7 is a two-dimensional plot of the corresponding hyperbolic emitter curve. The solid blue trace denotes the valid solution branch; the dashed blue trace is invalid according to a sign difference with the TDOA measurement and may be discarded.

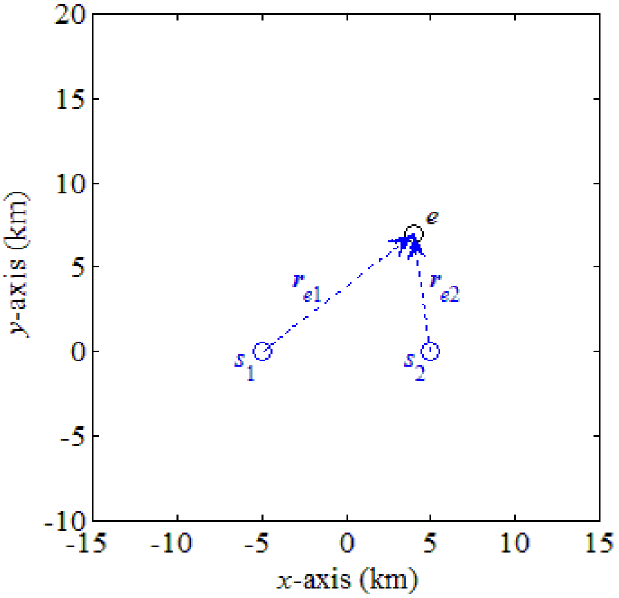

Figure 6. Two TDOA sensors attempt to locate an emitter of unknown position.

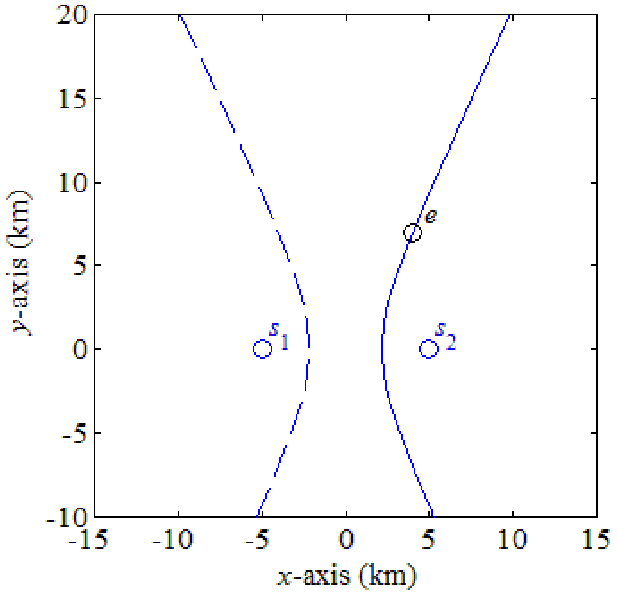

Figure 7. A single TDOA solution curve localizes the emitter to a hyperbolic curve.

As with the TOA technique, inclusion of a second measurement helps narrow the search for the emitter. Building on the previous example, we consider a third TDOA sensor s_3 positioned at coordinates $(-3,10)$ km. With three sensors in the constellation, there are three potential sensor pairs. As a first step, we include the measurement generated by the arrival time difference between sensors s_1 and s_3. Since this sensor pair is no longer solely located along the *x*-axis or centered at the origin, the hyperbolic solution derived above must be rotated and translated to accommodate the new sensor orientation.

To compute the required rotation matrix, we begin with the dot product expression

$$\boldsymbol{r}_{31} \cdot \hat{\boldsymbol{x}} = \left\|\boldsymbol{r}_{31}\right\| \left\|\hat{\boldsymbol{x}}\right\| \cos\left(\theta_{rot}\right), \tag{18}$$

where $\boldsymbol{r}_{31}$ is the position vector originating at sensor s_1 and terminating at sensor s_3, $\hat{\boldsymbol{x}}$ is the positive *x*-direction unit vector, and θ_{rot} is the angle of rotation between these two vectors. Understanding that $\left\|\hat{\boldsymbol{x}}\right\| = 1$, (18) may be rearranged as

$$\cos\left(\theta_{rot}\right) = \frac{\boldsymbol{r}_{31} \cdot \hat{\boldsymbol{x}}}{\left\|\boldsymbol{r}_{31}\right\|}. \tag{19}$$

We temporarily restrict the rotation angle to the range $(0°,180°)$ and solve:

$$\theta_{rot} = \arccos\left(\frac{\boldsymbol{r}_{31} \cdot \hat{\boldsymbol{x}}}{\left\|\boldsymbol{r}_{31}\right\|}\right). \tag{20}$$

To include rotation angles in the range $(-180°,180°)$, we must account for the inherent quadrant ambiguity of the arccosine function. Consider the signum function that is piecewise-defined as

$$\operatorname{sgn}\left(\alpha\right) = \begin{cases} -1, & \alpha < 0 \\ 0, & \alpha = 0. \\ 1, & \alpha > 0 \end{cases} \tag{21}$$

Note that the expression $\operatorname{sgn}\left(\boldsymbol{r}_{31} \cdot \hat{\boldsymbol{y}}\right)$ is positive for all points in the first and second quadrants and negative for all points in the third and fourth quadrants. We may accordingly compensate for the aforementioned arccosine quadrant ambiguity by writing

$$\theta_{rot} = \operatorname{sgn}\left(\boldsymbol{r}_{31} \cdot \hat{\boldsymbol{y}}\right) \arccos\left(\frac{\boldsymbol{r}_{31} \cdot \hat{\boldsymbol{x}}}{\left\|\boldsymbol{r}_{31}\right\|}\right). \tag{22}$$

Based on the rotation angle θ_{rot}, we define the rotation matrix [17]

$$R = \begin{bmatrix} \cos\left(\theta_{rot}\right) & -\sin\left(\theta_{rot}\right) \\ \sin\left(\theta_{rot}\right) & \cos\left(\theta_{rot}\right) \end{bmatrix}. \tag{23}$$

We further define the translation matrix

$$T = \begin{bmatrix} \left(\dfrac{\boldsymbol{r}_3 + \boldsymbol{r}_1}{2}\right) \cdot \hat{\boldsymbol{x}} \\ \left(\dfrac{\boldsymbol{r}_3 + \boldsymbol{r}_1}{2}\right) \cdot \hat{\boldsymbol{y}} \end{bmatrix}, \tag{24}$$

which specifies the coordinates of the midpoint between sensors s_1 and s_3 in column vector format. The rotated and translated hyperbola coordinates $\left(x', y'\right)$ are then given by

$$\begin{bmatrix} x' \\ y' \end{bmatrix} = R \begin{bmatrix} x \\ y \end{bmatrix} + T. \tag{25}$$

Following the prescribed rotation and translation procedure, the second TDOA emitter curve generated from the measurement between sensors s_1 and s_3 is shown in Figure 8. This second TDOA hyperbola is depicted as a red trace; the original TDOA hyperbola from Figure 7 is reproduced as a blue trace, sans the invalid branch. For further assurance of an accurate solution, one might use the third sensor pair s_2 and s_3. In Figure 9, the third TDOA solution curve is overlaid on the previous two TDOA curves. For visualization, the third solution curve is depicted as a red trace and the previous curves are reproduced as blue traces.

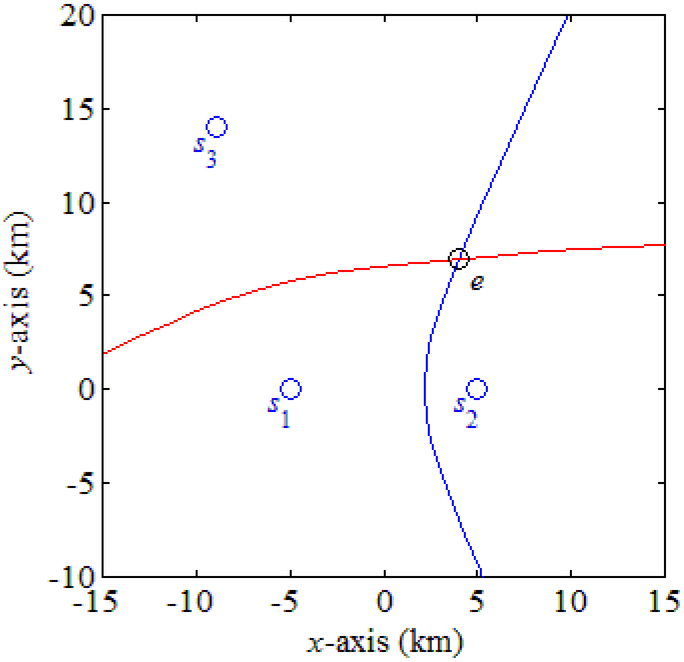

Figure 8. Two TDOA solution curves help locate an unknown emitter.

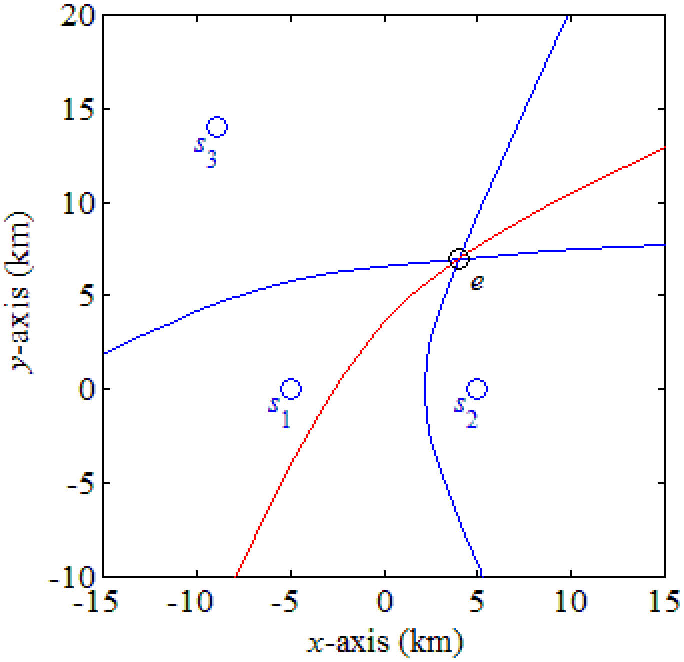

Figure 9. Three TDOA solution curves help locate an unknown emitter.

If more sensors are available, the corresponding measurements may be incorporated into the solution to increase estimation accuracy. In general, the number of possible sensor pair combinations for an N -sensor constellation is

$$p = \binom{N}{2} = \frac{N!}{2!(N-2)!}. \tag{26}$$

As a general trend, one would expect geolocation ambiguity to decrease as the number of TDOA measurements increases; yet, this does not always hold.

Unfortunately, the TDOA geolocation technique is subject to the same orientation-dependent restrictions as the TOA technique. If the TDOA sensors in a given constellation are arranged in a collinear orientation, the system will never be able to unambiguously resolve the emitter location. In two dimensions, all TDOA hyperbolas from collinear sensors intersect at both the true emitter location and its reflection point about the sensor axis. This inherent orientation-dependency is depicted in Figure 10.

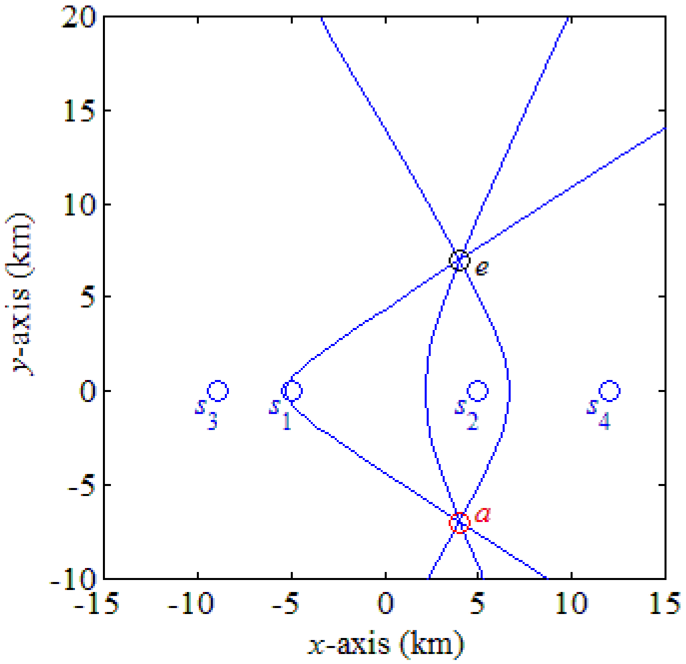

Figure 10. Four TDOA sensors unsuccessfully attempt to resolve geolocation ambiguity.

Here, four sensors are non-uniformly spaced along the *x*-axis, and three of the six possible TDOA hyperbolas are plotted. All emitter curves intersect at both the emitter location and the point of ambiguity a, at coordinates $(4,-7)$ km. As such, the network can never successfully resolve the emitter location.

Intuitively, it makes sense that collinear sensors entail an element of inherent ambiguity. First, note that the TDOA (and TOA) solution curve is always symmetric with respect to the sensor axis. For the TDOA case, the sensor axis is simply the major axis of the hyperbola. Second, note that all sensors lie along the same linear sensor axis (the *x*-axis in Figure 10). Together, these observations leave the sensors without any ability to discern knowledge regarding directions orthogonal to the sensor axis. In two dimensions, only two unit vectors satisfy this orthogonality criterion ($+\hat{y}$ and $-\hat{y}$ in Figure 10); one unit vector corresponds to the true emitter position ($+\hat{y}$) and one to the point of ambiguity ($-\hat{y}$). As we shall see, expanding the collinear ambiguity problem into three dimensions is crippling. In three dimensions, there is now an infinitude of unit vectors that are orthogonal to the sensor axis. As the TDOA problem extends into higher-dimensional scenarios, one must be acutely aware of the spatial dependencies and limitations.

C. THREE-DIMENSIONAL SOLUTION

The three-dimensional solution to the TDOA governing equation (see Equation 2) is, predictably, analogous to the two-dimensional solution. Whereas in two dimensions the emitter curve is a hyperbola, in three dimensions the emitter surface is a hyperboloid of two sheets. Consider a generic scenario with two TDOA sensors s_1 and s_2 located at coordinates $(-d,0,0)$ km and $(d,0,0)$ km, respectively. Assume the parameter $d > 0$. An emitter of unknown location generates a TDOA beacon signal that arrives at sensors s_1 and s_2 with time difference of τ_{21}. It can be shown algebraically (see Appendix for details) that the associated emitter surface is the set of all three-dimensional points (x,y,z) that satisfy the equation

$$\frac{4x^2}{(c_0\tau_{21})^2} - \frac{4y^2}{4d^2 - (c_0\tau_{21})^2} - \frac{4z^2}{4d^2 - (c_0\tau_{21})^2} = 1. \tag{27}$$

As in two dimensions, we refine this solution by selecting only the valid sheet according to the sign information of the TDOA measurement. The invalid sheet—corresponding to a TDOA measurement of the opposite sign—is discarded.

For illustration, we contrive an arbitrary scenario where $d = 5$ km and the unknown emitter is located at $(-6, -4, 5)$ km. The associated TDOA measurement value is calculated by sensors s_1 and s_2 to be $\tau_{21} = 20.84\ \mu\text{s}$. A three-dimensional plot of the hyperboloidal TDOA emitter surface is presented in Figure 11. In the figure, sensors s_1 and s_2 are depicted as red markers; the emitter is depicted as a black marker.

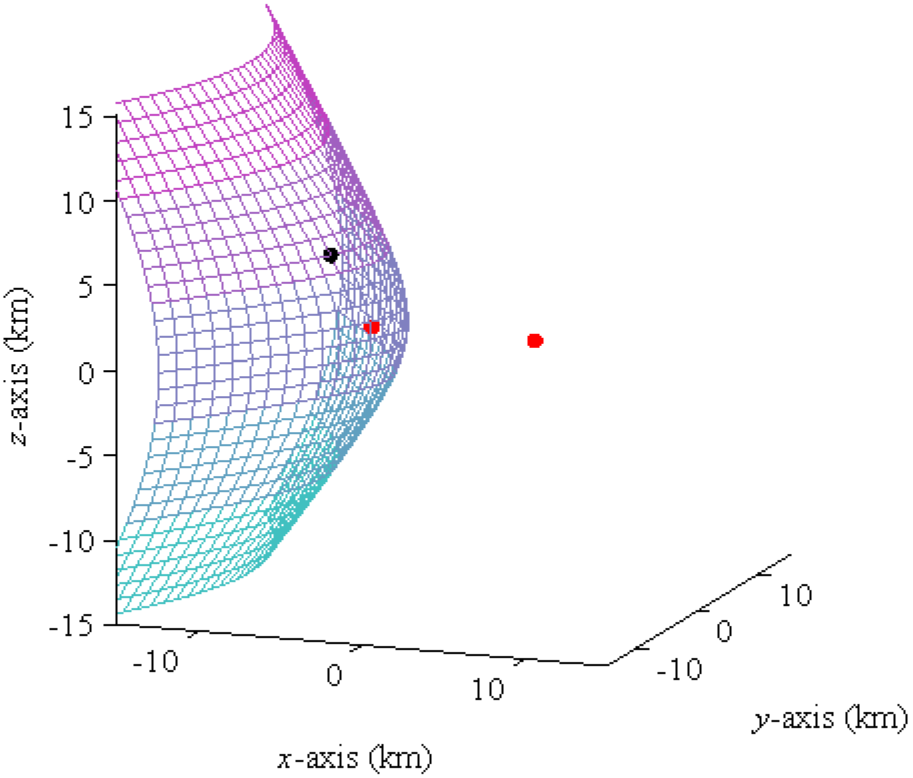

Figure 11. Two sensors generate one TDOA surface in three dimensions.

Including a second TDOA measurement further refines the emitter location. For an unambiguous TDOA solution, it is commonly noted that four or more sensors are required [12]. The use of three sensors at best refines the emitter location to several discrete locations. In this case, a priori information such as altitude or terrain information may be used to resolve the emitter position, but four or more sensors are necessary to ensure an unambiguous solution. Still, this conclusion bears the previously discussed caveat regarding collinear sensor orientation. In the collinear sensor case, the TDOA geolocation technique can only specify a circular curve on which the emitter must lie. Again, an analogy with the two-dimension ambiguity case is helpful. Referring to Figure 10, this circular ambiguity curve is simply the orbit traced by the points e and a when revolved around the sensor axis. It is therefore imperative that a TDOA sensor constellation avoid scenarios in which multiple sensors are arranged in collinear fashion. The associated TDOA measurements will unavoidably be redundant and the solutions ambiguous. Again, we note that the spatial orientation of the sensor constellation acutely affects the accuracy and functionality of the TDOA geolocation technique.

IV. FREQUENCY-DIFFERENCE-OF-ARRIVAL

A. DOPPLER EFFECT

The FDOA geolocation algorithm operates on the basic principle of the Doppler Effect. Consider a simple transmitter and receiver model as illustrated in the Figure 12 system diagram. The transmitter generates a cosinusoidal signal with center frequency f_0 that propagates through free space at the speed of light c_0 and is received by the receiver (classically termed "the observer").

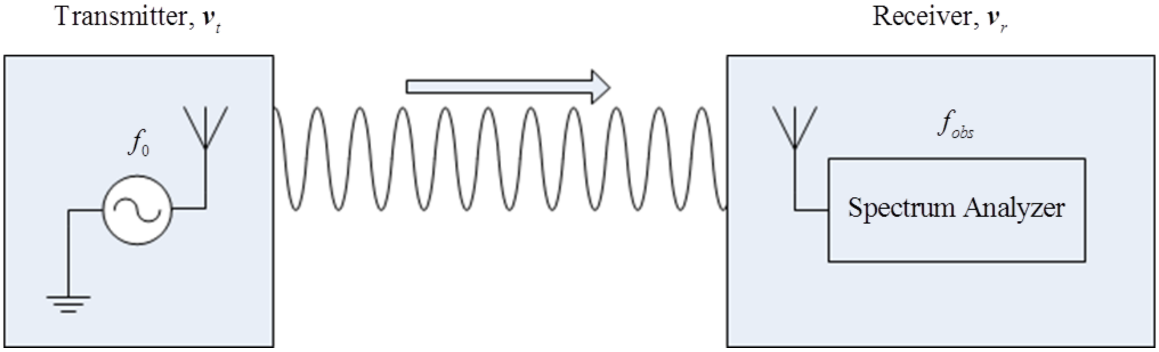

Figure 12. A transmitter/receiver model experiences a Doppler shift.

When both devices are stationary, the received frequency is the same as the transmitted frequency, namely f_0. Yet if the one or both of the devices are in motion with respect to some common reference, the transmitter will have a nonzero relative velocity with respect to the receiver. The obvious exception, of course, is the case when the transmitter and receiver have identical absolute velocities; subsequently, the relative velocity is zero. Mathematically, we define the vectorized transmitter velocity relative to the receiver as

$$\boldsymbol{v}_{tr} = \boldsymbol{v}_t - \boldsymbol{v}_r, \tag{28}$$

where $\boldsymbol{v}_t$ and $\boldsymbol{v}_r$ are the respective transmitter and receiver velocities in vector form. When the relative transmitter velocity contains a nonzero radial component—that is, the transmitter is moving either toward or away from the receiver—the receiver observes a shift in the observed frequency f_{obs}. If the transmitter is moving toward the receiver, the observed waveform appears compressed at the receiver such that $f_{obs} > f_0$. Conversely, if the transmitter is moving away from the receiver, the observed waveform appears elongated at the receiver such that $f_{obs} < f_0$. To quantify the frequency shift, we first define the unit vector

$$\hat{\boldsymbol{i}}_{tr} = \frac{\boldsymbol{r}_t - \boldsymbol{r}_r}{\left\| \boldsymbol{r}_t - \boldsymbol{r}_r \right\|}, \tag{29}$$

where $\boldsymbol{r}_t$ and $\boldsymbol{r}_r$ are vectors from the origin to the transmitter position and receiver position in space, respectively. Thus, the unit vector $\hat{\boldsymbol{i}}_{tr}$ points from the receiver position to the transmitter position. To then extract the radial component of the relative transmitter velocity, we compute the scalar speed

$$v_{tr}^{\hat{i}} = \boldsymbol{v}_{tr} \cdot \hat{\boldsymbol{i}}_{tr}. \tag{30}$$

We define the associated Doppler shift as the difference between the original oscillator frequency and the observed frequency, namely

$$\Delta f_D = f_{obs} - f_0. \tag{31}$$

We then relate the Doppler shift to the radial component of the relative transmitter velocity via the fundamental Doppler relationship [8]

$$\Delta f_D = \frac{f_0}{c_0}\left(v_{tr}^{\hat{i}}\right). \tag{32}$$

Note again that, to achieve a nonzero Doppler shift, we require a nonzero radial component of the transmitter velocity relative to the receiver velocity.

B. GOVERNING EQUATION

The basic premise of the FDOA geolocation algorithm is to use the observed Doppler effect on an unknown emitter's transmitted beacon signal to geolocate it in space. In the following section, we aim to derive a generalized FDOA governing equation based on the method proposed by Musicki and Koch [8]. Consider the generalized two-dimensional scenario depicted in Figure 13 to help illustrate the problem. For a single

FDOA measurement, two sensors are required with narrow frequency resolution. Sensors s_1 and s_2 move with the respective absolute velocities $\boldsymbol{v}_1$ and $\boldsymbol{v}_2$. Assume the propagation medium is isotropic and ideal and the system is noiseless. The emitter e moves with absolute velocity $\boldsymbol{v}_e$ and generates an omnidirectional FDOA beacon signal at the known oscillator center frequency f_0. The signal arrives at sensors s_1 and s_2 with observed center frequencies f_1 and f_2.

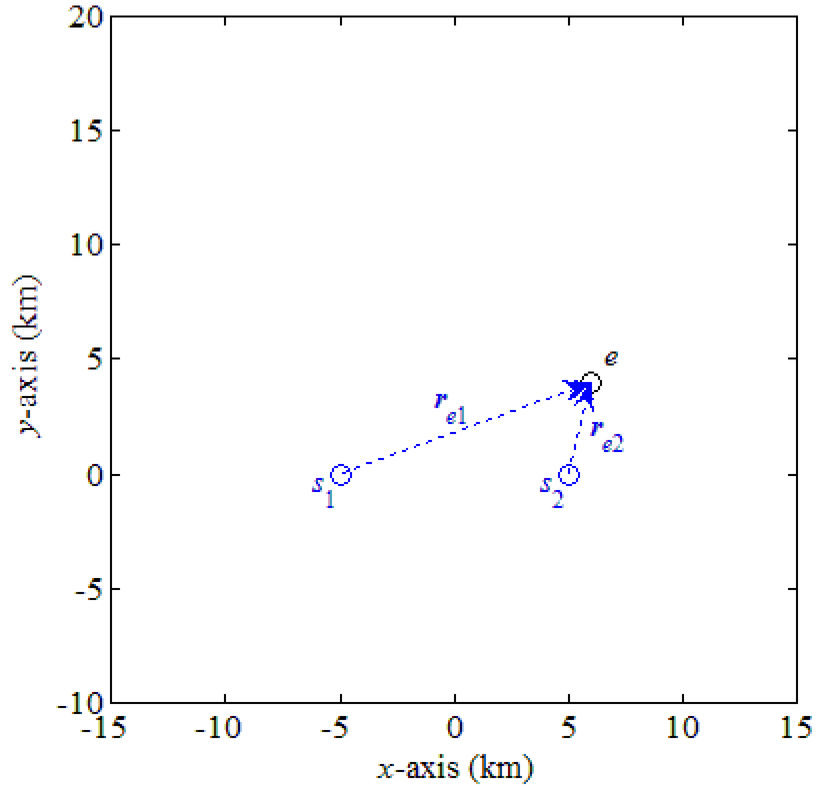

Figure 13. A two-sensor FDOA geolocation scenario is depicted.

From the observed frequencies measured at the two sensors, the FDOA measurement is calculated as

$$\Delta f_{21} = f_2 - f_1. \tag{33}$$

Since f_1 and f_2 are both observed frequencies, (31) enables us to write

$$f_1 = \Delta f_1 + f_0 \tag{34}$$

and

$$f_2 = \Delta f_2 + f_0, \tag{35}$$

where Δf_1 and Δf_2 are the Doppler shifts associated with the arriving signal at sensors s_1 and s_2. Thus, the FDOA measurement may be expressed as the difference in Doppler shifts between the two sensors; substitute (34) and (35) into (33) to give

$$\Delta f_{21} = \left(\Delta f_2 + f_0\right) - \left(\Delta f_1 + f_0\right) = \Delta f_2 - \Delta f_1. \tag{36}$$

To translate this frequency information into position information, we must first express the FDOA measurement in terms of relative velocities. Of particular interest, two relative emitter velocities are defined with respect to sensors s_1 and s_2:

$$\boldsymbol{v}_{e1} = \boldsymbol{v}_e - \boldsymbol{v}_1, \tag{37}$$

$$\boldsymbol{v}_{e2} = \boldsymbol{v}_e - \boldsymbol{v}_2. \tag{38}$$

According the generic form of (29), we next define the two similar unit vectors

$$\hat{\boldsymbol{i}}_{e1} = \frac{\boldsymbol{r}_e - \boldsymbol{r}_1}{\left\|\boldsymbol{r}_e - \boldsymbol{r}_1\right\|} = \frac{\boldsymbol{r}_{e1}}{\left\|\boldsymbol{r}_{e1}\right\|}, \tag{39}$$

and

$$\hat{\boldsymbol{i}}_{e2} = \frac{\boldsymbol{r}_e - \boldsymbol{r}_2}{\left\|\boldsymbol{r}_e - \boldsymbol{r}_2\right\|} = \frac{\boldsymbol{r}_{e2}}{\left\|\boldsymbol{r}_{e2}\right\|}. \tag{40}$$

Referencing (30) and (32), we may now express (36) as

$$\Delta f_{21} = \frac{f_0}{c_0}\left(v_{e2}^{\hat{i}} - v_{e1}^{\hat{i}}\right) = \frac{f_0}{c_0}\left(\boldsymbol{v}_{e2} \cdot \hat{\boldsymbol{i}}_{e2} - \boldsymbol{v}_{e1} \cdot \hat{\boldsymbol{i}}_{e1}\right). \tag{41}$$

Equation 41 may be considered the fundamental governing equation for the FDOA algorithm. Here, the FDOA measurement between sensors s_1 and s_2 is linked with the position information contained in the unit vectors $\hat{\boldsymbol{i}}_{e1}$ and $\hat{\boldsymbol{i}}_{e2}$. With all other system variables assumed to be known, any received FDOA measurement Δf_{21} can only result from a particular set of combinations of $\hat{\boldsymbol{i}}_{e1}$ and $\hat{\boldsymbol{i}}_{e2}$. This set of unit vector combinations describes the constant-FDOA curve. Each pair of associated unit vectors in the set may be thought of as a pair of rays that identify a single point on the constant-FDOA curve. The two rays originate at the known sensor locations and extend in the direction specified by the associated unit vectors. We solve for the intersection of these two rays using a three-dimensional triangulation method.

C. TRIANGULATION

A brief treatment of the triangulation method used in this research will likely be helpful. As may be discerned by cursory inspection, the FDOA governing equation presented in (41) requires a nontrivial solution strategy. To provide helpful illustrations without excessive computational demands, we consider a parametric solution. Such a solution lends itself to discretized rendering in computational software environments (e.g., MATLAB®). Accordingly, we consider the problem of triangulation in parametric terms.

The process of triangulation may be stated as follows. We attempt to determine the singular location in *N*-dimensional space at which two rays of known origination intersect, provided that they do indeed intersect. To begin the mathematical solution, a ray is defined in vector form as

$$\boldsymbol{p}_1(t_1) = \hat{\boldsymbol{i}}_1 t_1 + \boldsymbol{r}_1, \quad t_1 \geq 0, \tag{42}$$

where $\boldsymbol{r}_1$ describes the ray origination point with respect to the coordinate system origin, $\hat{\boldsymbol{i}}_1$ is a unit vector parallel to the direction of the ray's extension from the origination point, and t_1 is a nonnegative parameter. The ray $\boldsymbol{p}_1$ is known to intersect the similarly-defined ray

$$\boldsymbol{p}_2(t_2) = \hat{\boldsymbol{i}}_2 t_2 + \boldsymbol{r}_2, \quad t_2 \geq 0. \tag{43}$$

At the point of intersection, $\boldsymbol{p}_1\left(t_1'\right) = \boldsymbol{p}_2\left(t_2'\right)$. Using primed notation to specify this point of interest, we have

$$\hat{\boldsymbol{i}}_1 t_1' + \boldsymbol{r}_1 = \hat{\boldsymbol{i}}_2 t_2' + \boldsymbol{r}_2. \tag{44}$$

Rearranging gives

$$\boldsymbol{r}_2 - \boldsymbol{r}_1 = \hat{\boldsymbol{i}}_1 t_1' - \hat{\boldsymbol{i}}_2 t_2'. \tag{45}$$

Let us define $\Delta \boldsymbol{r}_{21} = \boldsymbol{r}_2 - \boldsymbol{r}_1$, which may be decomposed into its three-dimensional Cartesian components by

$$\Delta \boldsymbol{r}_{21} = \Delta r_{21x}\hat{x} + \Delta r_{21y}\hat{y} + \Delta r_{21z}\hat{z}. \tag{46}$$

We likewise decompose the unit vectors $\hat{\boldsymbol{i}}_1$ and $\hat{\boldsymbol{i}}_2$ as

$$\hat{\boldsymbol{i}}_1 = \hat{i}_{1x}\hat{x} + \hat{i}_{1y}\hat{y} + \hat{i}_{1z}\hat{z}, \tag{47}$$

$$\hat{\boldsymbol{i}}_2 = \hat{i}_{2x}\hat{x} + \hat{i}_{2y}\hat{y} + \hat{i}_{2z}\hat{z}. \tag{48}$$

Equation 46 may then be expanded into the system of linear equations

$$\Delta r_{21x} = t_1'\hat{i}_{1x} - t_2'\hat{i}_{2x} \tag{49}$$

$$\Delta r_{21y} = t_1'\hat{i}_{1y} - t_2'\hat{i}_{2y} \tag{50}$$

$$\Delta r_{21z} = t_1'\hat{i}_{1z} - t_2'\hat{i}_{2z}. \tag{51}$$

To solve for the two unknown parameters t_1' and t_2', only two of the three equations in the system are required. Rearranging (50) gives

$$t_2' = \left(\frac{1}{\hat{i}_{2y}}\right)\left(t_1'\hat{i}_{1y} - \Delta r_{21y}\right). \tag{52}$$

Substituting (52) into (49) then gives

$$\Delta r_{21x} = t_1'\hat{i}_{1x} - \left(\frac{1}{\hat{i}_{2y}}\right)\left(t_1'\hat{i}_{1y} - \Delta r_{21y}\right)\left(\hat{i}_{2x}\right). \tag{53}$$

Solving, we have

$$t_1' = \frac{\Delta r_{21x} - \left(\dfrac{\hat{i}_{2x}}{\hat{i}_{2y}}\right)\Delta r_{21y}}{\hat{i}_{1x} - \left(\dfrac{\hat{i}_{2x}}{\hat{i}_{2y}}\right)\hat{i}_{1y}} \geq 0. \tag{54}$$

Thus, the two rays defined above intersect at the point specified by $\boldsymbol{p}_1\left(t_1'\right)$, where t_1' is computed as specified in (54).

This parametric solution to the triangulation problem presumes the foreknowledge of both unit vectors that describe the two intersecting rays. In the FDOA problem, there is a pair of unit vectors describing each point along the constant-FDOA solution curve. Hence, to find all points on the continuous FDOA curve, one must perform this parametric triangulation an infinite number of times. This impossibility is obviously avoided. Rather, a sampled solution of the FDOA solution curve shall be computed.

D. TWO-DIMENSIONAL SOLUTION

The complexity of the FDOA solution curve is readily apparent even in the simplified two-dimensional case. We shall consider several scenarios in this section to illustrate the spatial dependencies of the FDOA algorithm. In particular, we demonstrate the impact of sensor motion relative to the sensor axis. Consider a generic scenario with two sensors s_1 and s_2 moving with velocities $\boldsymbol{v}_1$ and $\boldsymbol{v}_2$ and located at coordinates $\left(-d,0,0\right)$ and $\left(d,0,0\right)$, respectively. We illustrate this setup for $d=5$ km in Figure 14.

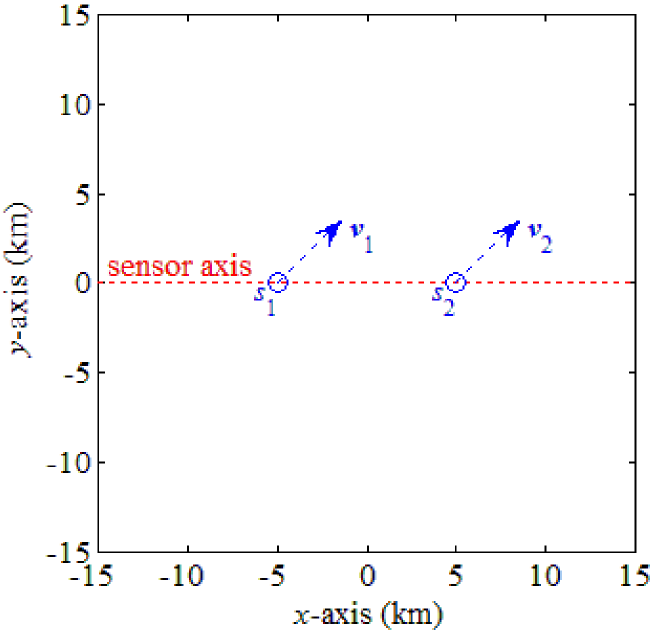

Figure 14. Two sensors move with respect to the sensor axis.

We shall consider two limiting conditions and one transitional condition. First, we shall consider the scenario where sensor velocities are identical and parallel to the sensor axis. Second, we shall consider the scenario where sensor velocities are identical and orthogonal to the sensor axis. Third, we shall consider a transitional scenario where sensor velocities are identical and oriented at $60°$ relative to the sensor axis.

1. Parallel Motion Condition

Consider the case where both sensors s_1 and s_2 have identical velocities directed parallel to the sensor axis (here, the $+\hat{x}$ direction). The magnitude of the velocity is inconsequential; however, for illustration's sake we choose the arbitrary sensor velocity of $+10\hat{x}$ m/s. Sensors s_1 and s_2 are located at $(-5,0)$ and $(5,0)$ km, respectively. The emitter location—recall this information is unknown to the system a priori—is chosen to be $(6,4)$ km. The associated FDOA solution curve is presented in Figure 15. Note that the parallel motion condition yields a continuous constant-FDOA solution curve.

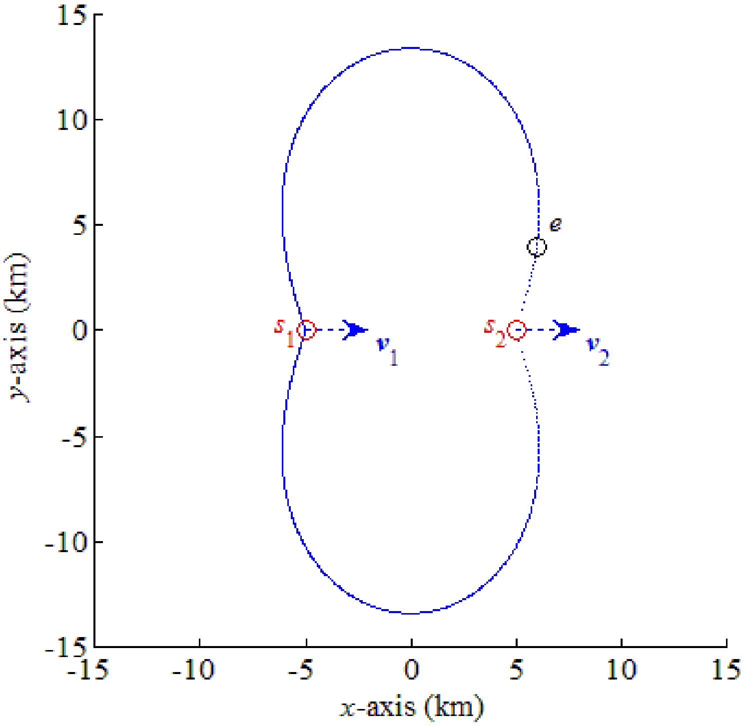

Figure 15. Two FDOA sensors geolocate in the parallel motion condition.

We stated above that the magnitude of the sensor velocities was inconsequential. Indeed, if the FDOA solution curve is computed for a sensor velocity of $+100\hat{x}$ m/s, one finds an identical solution to the $+10\hat{x}$ m/s case. Certainly, with the tenfold increase in sensor velocity, the absolute value of the FDOA measurement increases proportionally; however, the FDOA curve is generated by triangulation of intersecting unit vectors. The issue of concern (see Equation 41) is not the absolute values of the sensor velocities but rather the projection of the sensor velocity vectors onto the associated unit vectors via the dot product. The FDOA solution curve is bound up with the directional information of the sensor velocities relative to the sensor axis. Thus, if the velocities are directed away from the sensor axis, we see a dramatic shift in form for the solution curve.

2. Orthogonal Motion Condition

To that end, we next consider the case where sensors s_1 and s_2 have identical velocities directed orthogonally to the sensor axis, namely the $+\hat{y}$ direction. The magnitude of the velocity is again inconsequential, but we choose the arbitrary sensor velocity of $+10\hat{y}$ m/s. The emitter is at coordinates $(6,4)$ km. See Figure 16 for the associated FDOA solution curve. Here, we see that the orthogonal motion condition yields a non-continuous, multiple-branch FDOA solution curve.

The complexity of the FDOA solution become apparent. Whereas the TDOA algorithm yielded a hyperbola of varying parameter values, the FDOA algorithm may yield a disjointed, piecewise solution depending on the sensor orientation and motion. Parallel motion gave a single continuous solution curve. At some transition point between the parallel and orthogonal conditions, the solution breaks into two distinct non-continuous branches. The transition point is a singularity and makes it difficult to characterize algorithm properties such as the number of required sensors to guarantee unambiguous geolocation solutions. Furthermore, the symmetric properties of the FDOA solution vary. In the parallel motion condition, we found a symmetric solution about the sensor axis. With orthogonal motion, this symmetry fails.

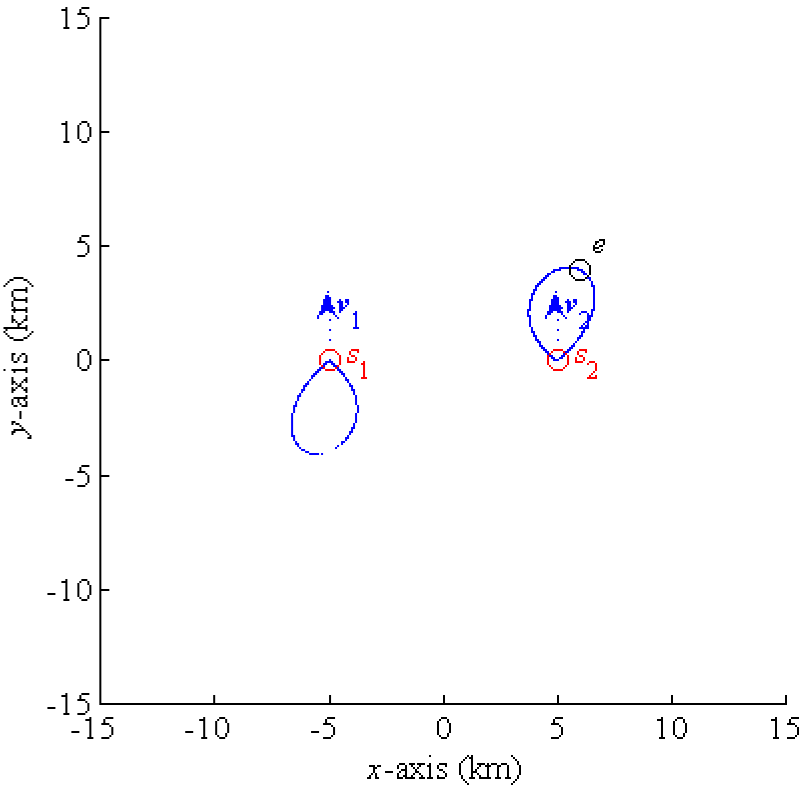

Figure 16. Two FDOA sensors geolocate in the orthogonal motion condition.

3. 60° Sensor Motion Condition

We consider one case in the aforementioned transitional region between parallel and orthogonal sensor motion relative to the sensor axis. The sensors and emitter are located at the same positions described previously. Let us choose, however, the sensor velocity $\boldsymbol{v}_1 = \boldsymbol{v}_2 = \left(5.00\hat{x} + 8.66\hat{y}\right)$ m/s. Such a velocity forms a 60° interior angle with the sensor axis ($+\hat{x}$ orientation). The resulting constant-FDOA solution curve is given in Figure 17. The solution is again a non-continuous, multiple-branch curve. The angular offset effectively skews the direction of the two lobes of the curve. The extent of the FDOA solution dependency on sensor motion direction is readily apparent.

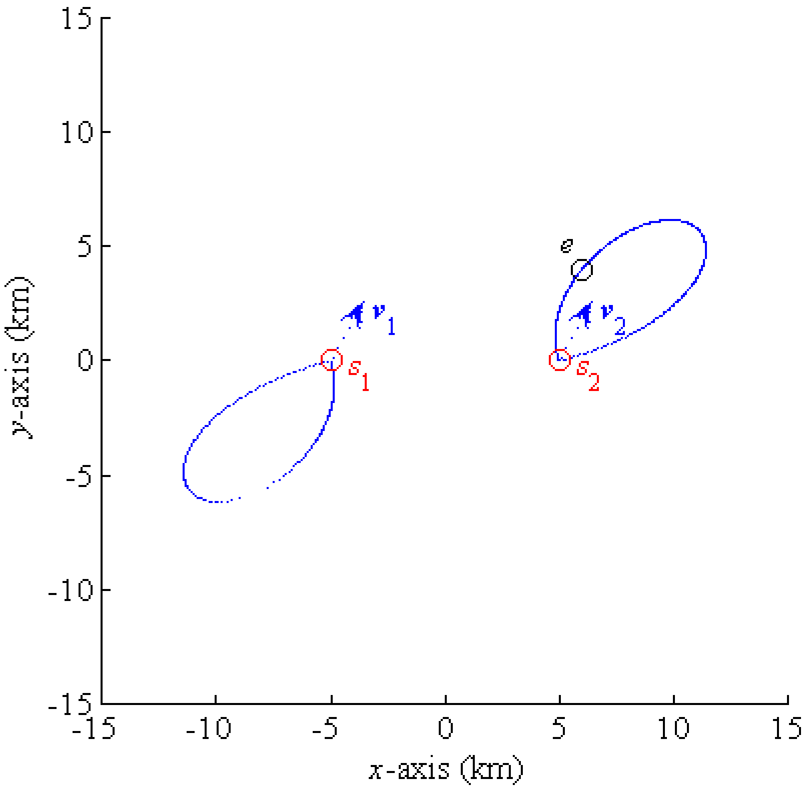

Figure 17. FDOA sensors geolocate for $60°$ motion relative to the sensor axis.

E. THREE-DIMENSIONAL SOLUTION

The mathematical solution for the FDOA equation in three dimensions follows closely that of the two-dimensional case. While not increasing in theoretical complexity, the parametric nature of the proposed solution raises the computational demands significantly. In two dimensions, the *x*-*y* plane is described by the fixed polar angle $\theta = 90°$; consequently, the previous solution only demanded computation time on the order of $O(m)$, where *m* is the number of azimuthal angle samples in the range $[0, 2\pi]$ and $O(\cdot)$ represents the traditional big O notation. Extension into three-dimensional spherical coordinates requires *n* polar angle samples in the range $[0°, 180°]$ per azimuth angle; therefore, the associated computation proceeds as $O(mn)$. For any reasonable degree of spatial precision, significant computational resources are required. Accordingly, it is increasingly difficult to render high-quality three-dimensional images of the FDOA solution surface. Thus, in the figures that follow, only discrete sample points are plotted. An effort has been made to choose a sufficiently small spatial sample size so as to capture the general shape of the FDOA solution surfaces.

1. Parallel Motion Condition

Two sensors s_1 and s_2 are located at coordinates $(-5,0,0)$ and $(5,0,0)$ km and have identical velocities of $+10\hat{x}$ m/s. A stationary emitter is placed at coordinates $(6,4,0)$ km. The corresponding FDOA solution surface is presented in Figure 18. On the left, a three-dimensional view is given. On the right, a top-down view is given from the perspective of the $+z$ axis; all points are therefore projected onto the *x*-*y* plane. The sensors and emitter are depicted as red and black markers, respectively.

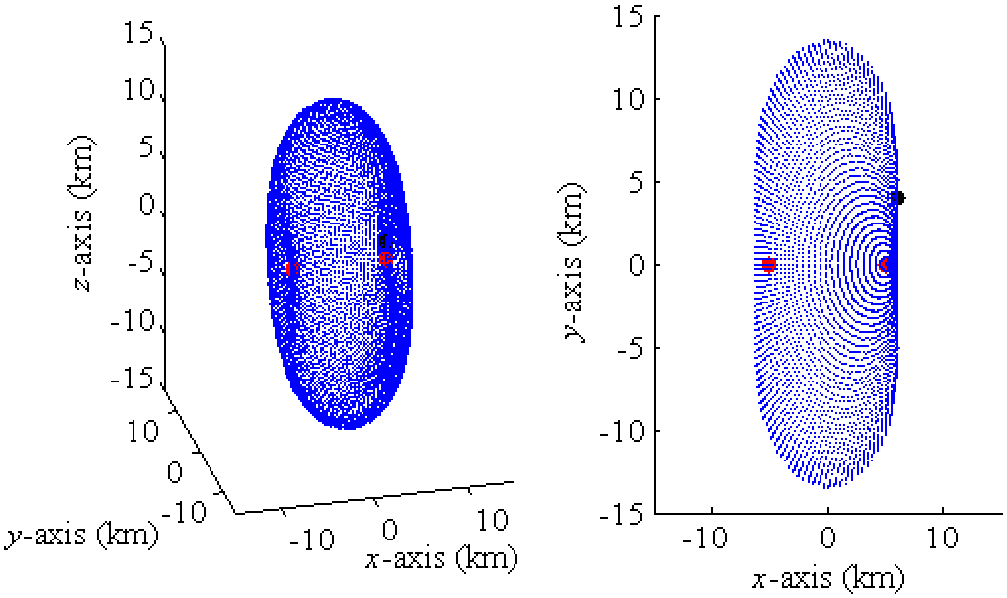

Figure 18. Three- and two-dimensional views are given of the sampled FDOA surface for the parallel motion condition.

Here, the symmetry about the sensor axis is convenient when generating the three-dimensional surface. Indeed, the solution is simply a surface of revolution using the two-dimensional "peanut"-shaped solution found previously. The axis of revolution is the sensor axis; here again, since both sensors are located directly on the *x*-axis, the sensor axis is the *x*-axis. This is the simplest condition for which the FDOA equation may be solved in three dimensions.

2. Orthogonal Motion Condition

Let us reset the sensor velocities in the scenario above to $+10\hat{y}$ m/s. The sensors now move orthogonally with respect to the sensor axis (*x*-axis). With all other environmental parameters held constant, the corresponding FDOA solution surface is given in Figure 19. On the left, a three-dimensional view is given. On the right, a top-down projection onto the *x*-*y* plane is given. Now the axial symmetry is lost. The solution surface is no longer a surface of revolution, and the need for a parametric solution strategy is validated.

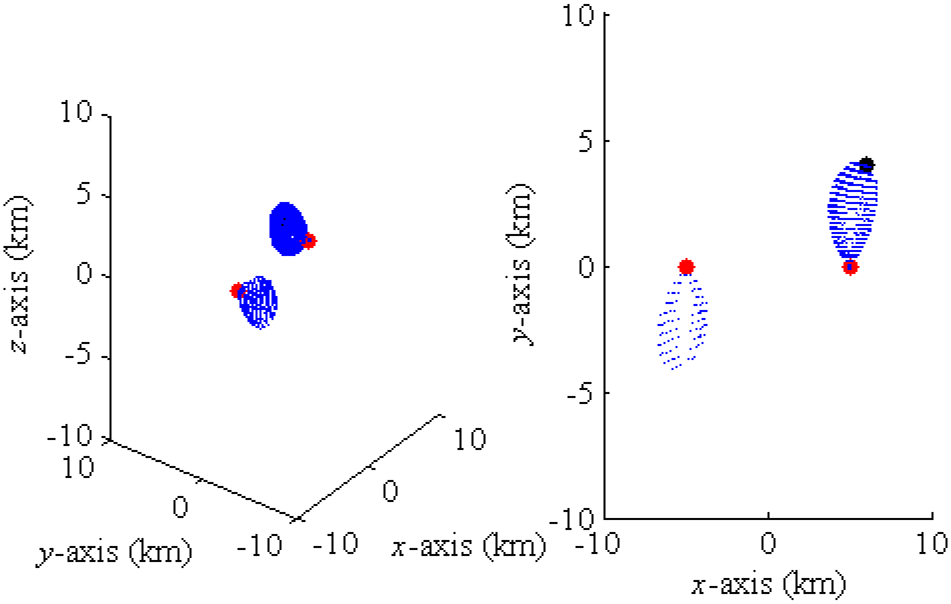

Figure 19. Three- and two-dimensional views are given of the sampled FDOA surface for the orthogonal motion condition.

3. 60° Sensor Motion Condition

Lastly, we revisit the 60° sensor motion condition, where the sensor velocities are set to $\left(5.00\hat{x}+8.66\hat{y}\right)$ m/s. The FDOA surface is shown in Figure 20. As before, a three-dimensional solution is given on the left, and a two-dimensional projection in the *x*-*y* plane is given on the right. Clearly, no symmetry about the sensor axis (*x*-axis) is available; thus, the surface is not the result of revolution. Although the two lobes found in the solution are similar in shape, the symmetry is more difficult to define mathematically and offers little advantage in easing the solution requirements.

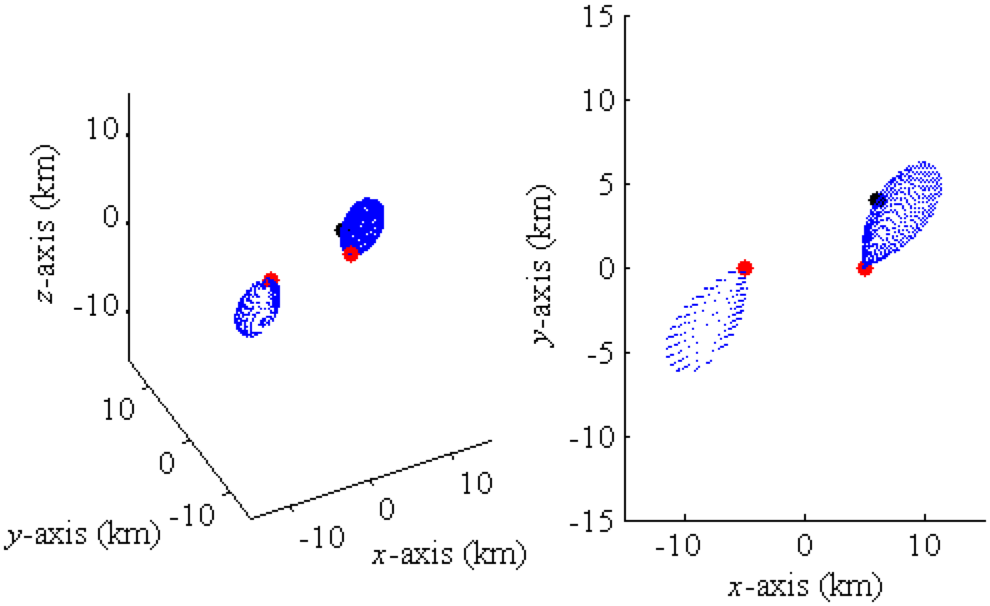

Figure 20. Three- and two-dimensional views are given of the sampled FDOA surface for the 60° relative motion condition.

V. NOISE CONSIDERATIONS

A. SOURCES

As with any real system, noise is an unavoidable complication. Here, the term noise refers to any mechanism by which errors are introduced into a system. Some geolocation systems may be particularly tolerant to various types of noise, yet the corruptive impact of noise is felt to some degree in all facets of a geolocation algorithm. One might broadly categorize noise sources as internal or external to the geolocation system. External errors may arise from such causes as inhomogeneity in the propagation medium, thermal agitation of the medium, nonzero dispersion characteristics of the medium, and nonlinear delay profiles for LOS transmissions. For satellite systems, with significant propagation distances, issues such as scattering and refraction in the ionosphere greatly impact signal quality and delay. Internal errors may arise from thermal receiver noise, inaccurate synchronization to a global clock, assumption inaccuracies, hardware degradation and failure, or computational rounding error. Altogether, the list of potential sources of error is extensive. Thus, accurate statistical characterization of such a complicated system through a simple noise model is a challenge, to say the least.

B. NOISE MODELS

With so many diverse noise sources and environmental parameters to be considered, developing a representative geolocation noise model is an area of significant attention. For instance, the Community Coordinated Modeling Center (CCMC)—a multi-agency space weather partnership led by NASA—provides public access to nine distinct ionospheric computational electromagnetic (CEM) models developed by a variety of universities and research institutions [18]. Modeling these propagation characteristics alone can be extremely complicated, so in order to maintain our research focus of data fusion in time, we initially choose a basic additive noise model.

1. TOA Noise Model

For time-domain measurements, we choose to model the net environmental impact and system errors using a single exponentially-distributed, additive noise parameter specific to a given sensor s_i. The exponential distribution is selected to model the time delay for two reasons. First, the exponential distribution places a hard lower bound on the delay; the beacon signal cannot arrive at sensor s_i with delay smaller than the propagation time associated with the free-space propagation speed c_0. Second, the exponential distribution is relatively simple to handle mathematically, which helps avoid unnecessary complications in the analytical work to follow.

To clarify the notation convention used hereafter, an exponential random variable *x* with the probability density function (PDF)

$$f_X(x) = \begin{cases} 0, & x < 0 \\ \lambda e^{-\lambda x}, & x \geq 0 \end{cases} \tag{55}$$

given in terms of the statistical parameter λ may be alternatively defined using the condensed notation $x \sim Exp(\lambda)$. This generic random variable *x* has mean $\mu_x = \lambda^{-1}$, variance $\sigma_x{}^2 = \lambda^{-2}$, and standard deviation $\sigma_x = \lambda^{-1}$ [19].

Let us define the time-domain noise parameter associated with sensor s_i as $\delta_{\tau i} \sim Exp(\lambda_i)$. A TOA measurement collected by sensor s_i may then be expressed as the sum of the theoretical deterministic time delay (see Equation 1) and the random variable $\delta_{\tau i}$:

$$\tau_i = \overbrace{\frac{\|\boldsymbol{r}_e - \boldsymbol{r}_i\|}{c_0}}^{\text{deterministic}} + \overbrace{\delta_{\tau i}}^{\text{random}}. \tag{56}$$

The resulting noisy TOA measurement is a random variable with mean

$$\mu_{\tau i} = \frac{\|\boldsymbol{r}_e - \boldsymbol{r}_i\|}{c_0} + \frac{1}{\lambda_i} \tag{57}$$

and standard deviation

$$\sigma_{\tau i} = \frac{1}{\lambda_i}. \tag{58}$$

Indeed, the exponential distribution is a rough first approximation of the time-domain noise effects on a TOA beacon signal. Still, it provides a suitable first approximation of the stochastic properties associated with atmospheric propagation and noise without introducing excessive complexity into the problem. In light of this assumption, we emphasize the additive random nature of the noise parameter used in this model. This modular design easily allows for future modifications. If another PDF—defined either analytically or empirically—is found to better suit the propagation model, one need simply replace the PDF description and re-execute the simulations included in this research. Alternative distributions that have found applications in the wireless environment are the Rayleigh, Rician, and lognormal distributions [20]. Future work might explore the incorporation of these distributions in this geolocation model.

2. TDOA Noise Model

The TDOA noise model is largely built upon the TOA noise model. The TDOA measurement is defined as the difference between the two distinct arrival times at sensors s_i and s_j (see Equation 3). The arrival times τ_i and τ_j may be decomposed into one deterministic and one random-valued term, as in (56) with the TOA model. We thus express the TDOA measurement as

$$\tau_{ij} = \left(\frac{\|\boldsymbol{r}_e - \boldsymbol{r}_i\|}{c_0} + \delta_i \right) - \left(\frac{\|\boldsymbol{r}_e - \boldsymbol{r}_j\|}{c_0} + \delta_j \right) = \overbrace{\frac{1}{c_0}\left(\|\boldsymbol{r}_e - \boldsymbol{r}_i\| - \|\boldsymbol{r}_e - \boldsymbol{r}_j\| \right)}^{\text{deterministic}} + \overbrace{\left(\delta_{\tau i} - \delta_{\tau j} \right)}^{\text{random}}. \tag{59}$$

Let us assume the random noise parameters $\delta_{\tau i}$ and $\delta_{\tau j}$ are independent and identically distributed (IID) exponential random variables, implying $\lambda_i = \lambda_j$. When computing the difference between two independent exponential random variables, we subtract the respective means and add the respective variances to characterize the resulting distribution. If the random variables are further identically distributed, the resulting distribution has mean $\mu_x - \mu_x = 0$ and variance ${\sigma_x}^2 + {\sigma_x}^2 = 2{\sigma_x}^2$. Applying this to (59), we find that the TDOA measurement τ_{ij} is a random variable with mean

$$\mu_{\tau ij} = \frac{1}{c_0}\left(\left\|\boldsymbol{r}_e - \boldsymbol{r}_i\right\| - \left\|\boldsymbol{r}_e - \boldsymbol{r}_j\right\|\right) \tag{60}$$

and standard deviation

$$\sigma_{\tau ij} = \frac{\sqrt{2}}{\lambda_i}. \tag{61}$$

Note how the same time delay distribution characterized by the parameter λ_i causes a factor of $\sqrt{2}$ increase in the TDOA measurement standard deviation compared against the TOA measurement standard deviation.

3. FDOA Noise Model

Since the FDOA algorithm is built upon variations in the Doppler shift, we must consider the effect of environmental and system noise on the Doppler shift of a given signal. In the frequency domain, a propagating signal does not have the same restrictions as in the time delay model, where there is a hard minimum delay associated with the free-space propagation speed. Rather, it is equally likely that the observed frequency of arrival at a given sensor will be less than or greater than the anticipated center frequency. As such, we choose to model the Doppler shift noise as a Gaussian-distributed random variable, which is symmetric about its mean value. To be explicit, a generic Gaussian random variable X, with mean μ and standard deviation σ, is characterized with the PDF [19]

$$f_X(x) = \frac{1}{\sigma\sqrt{2\pi}} e^{-\frac{(x-\mu)^2}{2\sigma^2}}. \tag{62}$$

We introduce the condensed notation which alternatively defines the same Gaussian random variable $x \sim N\left(\mu, \sigma^2\right)$.

Recall that the FDOA measurement is the difference in Doppler shift experienced by the emitter beacon signal upon arrival at sensor s_i and s_j (see Equation 36). Let us model the Doppler shift observed at sensor s_i as the sum of the theoretical Doppler shift due to the radial component of the relative velocity of the emitter (see Equation 32) and a Gaussian-distributed random variable $\delta_{fi} \sim N\left(\mu_{\delta fi}, {\sigma_{\delta fi}}^2\right)$:

$$\Delta f_i = \frac{f_0}{c_0}\left(v_{ei}^{\hat{i}}\right) + \delta_{fi}. \tag{63}$$

We similarly model the Doppler shift observed at sensor s_j in terms of the Gaussian-distributed random variable $\delta_{fj} \sim N\left(\mu_{\delta fj}, {\sigma_{\delta fj}}^2\right)$:

$$\Delta f_j = \frac{f_0}{c_0}\left(v_{ej}^{\hat{i}}\right) + \delta_{fj}. \tag{64}$$

The FDOA measurement $\Delta f_{ij} = \Delta f_i - \Delta f_j$ computed between sensors s_i and s_j may now be expressed as the sum of the deterministic FDOA value predicted by (41) and a random noise component:

$$\Delta f_{ij} = \overbrace{\frac{f_0}{c_0}\left(v_{ei}^{\hat{i}} - v_{ej}^{\hat{i}}\right)}^{\text{deterministic}} + \overbrace{\left(\delta_{fi} - \delta_{fj}\right)}^{\text{random}}. \tag{65}$$

The random noise component of the FDOA measurement, given by $\left(\delta_{fi} - \delta_{fj}\right)$, is the difference of two Gaussian distributions; to characterize the resulting distribution, we subtract the means and add the variances. The resulting random variable is Gaussian-distributed as $\left(\delta_{fi} - \delta_{fj}\right) \sim N\left(\mu_{\delta fi} - \mu_{\delta fj}, {\sigma_{\delta fi}}^2 + {\sigma_{\delta fj}}^2\right)$. Considering the deterministic FDOA value as a bias, the total FDOA measurement is Gaussian-distributed according to

$$\Delta f_{ij} \sim N\left(\left[\frac{f_0}{c_0}\left(v_{ei}^{\hat{i}} - v_{ej}^{\hat{i}}\right) + \mu_{\delta fi} - \mu_{\delta fj}\right], \left({\sigma_{\delta fi}}^2 + {\sigma_{\delta fj}}^2\right)\right). \tag{66}$$

This is a generalized form of the FDOA noise model. We assume the Doppler shifts Δf_i and Δf_j are IID and zero-mean. In this case, ${\sigma_{\delta fi}}^2 = {\sigma_{\delta fj}}^2 = {\sigma_{\delta f}}^2$, and (66) reduces to the more manageable form

$$\Delta f_{ij} \sim N\left(\frac{f_0}{c_0}\left(v_{ei}^{\hat{i}} - v_{ej}^{\hat{i}} \right), 2{\sigma_{\delta f}}^2 \right). \tag{67}$$

Notice that the standard deviation of the FDOA measurement is scaled by the factor $\sqrt{2}$ when compared with the Doppler shift observed at an individual sensor. Like in TDOA, an FDOA measurement is the difference of two independent random variables; as such the total variance is larger than that of either individual random variable.

C. NOISE PARAMETER ESTIMATION

To complete the TOA, TDOA, and FDOA noise models, parameter values are needed for the time delay and Doppler shift noise profiles. Two broad cases are considered. First, the sensors are modeled as high-altitude geolocation satellites. Second, the sensors are modeled as low-altitude UAVs. Depending on the altitude, the time delay and Doppler shift profiles are significantly different.

1. High-altitude Sensors

A significant source of signal deterioration in high-altitude satellite communications is propagation through the ionosphere. The ionosphere is a series of layers in the Earth's upper atmosphere with characteristically high concentrations of ionized particles and free electrons. The altitude boundaries of the ionosphere are highly variable, depending on solar weather conditions and the time of day. Typically, the ionospheric layer ranges from a lower altitude of 50–600 km to an upper altitude of 600–2,000 km [21]. All altitudes are referenced to the Earth's surface unless otherwise stated. An electromagnetic (EM) signal passing through this thick ionized medium may experience significant degradation from propagation effects including attenuation, Faraday rotation, group delay, scintillations, and refraction [22]. The task here is to determine the aggregate impact of such ionospheric effects on the time delay and Doppler shift of a transiting beacon signal.

The following discussion uses the orbital and communications figures attending to the Global Navigation Satellite System (GNSS) satellite constellation. The orbital altitude is 19,100 km, the orbital speed is 3.95×10^3 m/s, and the primary communications operating frequency is within the L1 band at 1575.42 MHz [23], [24]. The emitter is assumed to be stationary.

a. Time Delay Variation Characterization

Let us begin our time delay variation discussion with a brief review of EM wave propagation theory. The following is adapted from the extensive treatment given to Maxwell's equations and plane-wave propagation in [25]. As with any electromagnetic field, Maxwell's equations govern a satellite communication signal transiting the ionosphere. The homogeneous wave equation is a solution to the time-harmonic Maxwell's equations and gives

$$\nabla^2 \tilde{\boldsymbol{E}} + \omega^2 \mu \varepsilon \tilde{\boldsymbol{E}} = 0, \tag{68}$$

where ω is the angular frequency of the oscillating field; μ and ε are the magnetic permeability and electric permittivity, respectively, of the medium; and $\tilde{\boldsymbol{E}}$ is the monotonic electric field vector in phasor form. The wave equation is frequently expressed in terms of the wavenumber

$$k = \omega \sqrt{\mu \varepsilon}. \tag{69}$$

Often, the permeability is written in terms of the relative permeability μ_r and the free-space permeability μ_0:

$$\mu = \mu_r \mu_0. \tag{70}$$

The permittivity is likewise written in terms of a relative and free-space value as

$$\varepsilon = \varepsilon_r \varepsilon_0. \tag{71}$$

We may also define the index of refraction n such that

$$n^2 = \mu_r \varepsilon_r. \tag{72}$$

Except for very rare types of materials, $n > 0$ and the positive root of (72) is used. Noting that the speed of light is defined as $c_0 = 1 \big/ \sqrt{\mu_0 \varepsilon_0}$, the phase velocity of the electric field is

$$v_p = \frac{c_0}{\sqrt{\mu_r \varepsilon_r}} = \frac{c_0}{n}. \tag{73}$$

This is the velocity of the constant-phase points of the traveling EM wave and may exceed the speed of light in a vacuum c_0 in some instances without violating physical laws.

When an information signal is modulated onto an EM carrier, the result is no longer monotonic, and the bandwidth is nonzero. Consequently, the information propagates through the medium at what is termed the group velocity v_g, which is not necessarily equivalent to the phase velocity v_p and is bounded by c_0 as a maximum value. The net result is a delay in the arrival of the information signal that is termed the group delay $\Delta\tau_g$. The analytical solution for the group delay involves the use of the Appleton-Hartree equation and is too involved for the scope of our present discussion; see the chapters entitled “Plane Waves” and “Ionospheric Propagation” in [22] for an extensive treatment of the group delay. Instead, we use the final approximate result for group delay when propagating through an ionized medium:

$$\Delta\tau_g \simeq \frac{1}{8\pi^2}\left(\frac{e^2}{\varepsilon_0 m_e c_0}\right)\frac{T_{ec}}{f^2}, \tag{74}$$

where e is the fundamental charge of an electron, m_e is the mass of an electron, f is the frequency of the EM wave, and T_{ec} is the total electron content of the transmission path [22]. We use the average group delay as the statistical mean of the time delay noise profile in our noise model, but first we must solve for all variables in (74).

The approximate group delay result above is based upon a model of the ionosphere as a Lorentz plasma with volumetric electron density N_e [22], [26]. The total electron content is defined as the path integral of the electron density:

$$T_{ec} \equiv \int_s N_e \, ds. \tag{75}$$

Let us assume the electron density is given by the simple piecewise expression

$$N_e = \begin{cases} 0, & h < h_{ion}^- \\ N_{ion}, & h_{ion}^- \le h \le h_{ion}^+ \\ 0, & h > h_{ion}^+ \end{cases}, \tag{76}$$

where N_{ion} is the constant electron density within the ionosphere and h_{ion}^- and h_{ion}^+ are the lower and upper altitude limits of the ionosphere. If we further assume vertical propagation from an emitter entirely below the ionosphere $\left(h < h_{ion}^-\right)$ to a satellite beyond the ionosphere $\left(h > h_{ion}^+\right)$, the total electron density reduces to

$$T_{ec} = N_{ion}\left(h_{ion}^+ - h_{ion}^-\right). \tag{77}$$

Recall from above that the lower altitude limit of the ionosphere typically ranges from 50–600 km; let us choose 325 km as the average value of h_{ion}^-. The upper altitude limit ranges from 600–2,000 km; choose 1,300 km as the average value of h_{ion}^+. We thus say, on average, the thickness of the ionosphere is $\left(h_{ion}^+ - h_{ion}^-\right) = 975\text{ km}$.

We determine an electron density of the ionosphere from computer prediction models. One model of interest is the Global Assimilation of Ionospheric Measurements (GAIM) developed at Utah State University. Recent simulation run results are made available to the public by the CCMC [18]. Consider a typical simulation forecast run for January 2, 2012. For an altitude of 844 km, the electron density N_e is forecasted at 15-minute intervals for all latitude and longitude coordinates. The simulation results for 00:00:00 UTC are shown in Figure 21. Here, the electron density is plotted in electrons/cm^3 with a colorbar on the right side of the figure for scaling purposes.

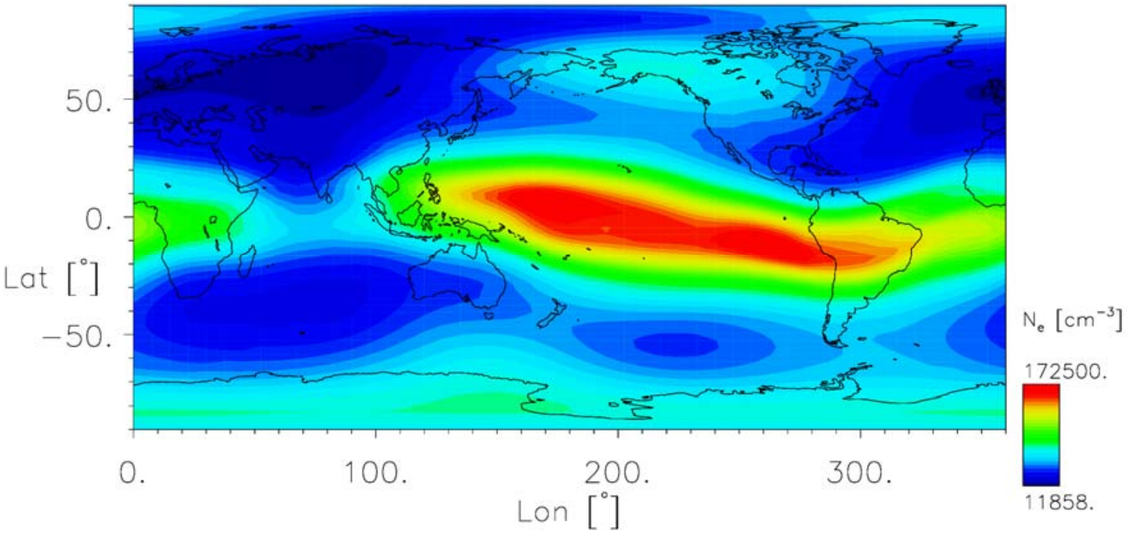

Figure 21. The electron density of the ionosphere at altitude 844 km varies with latitude and longitude on January 2, 2012 at 00:00:00 UTC. From [27].

Results from 12 hours later at 12:00:00 UTC are shown in Figure 22. Again, the electron density is plotted in electrons/cm^3 and a colorbar is provided.

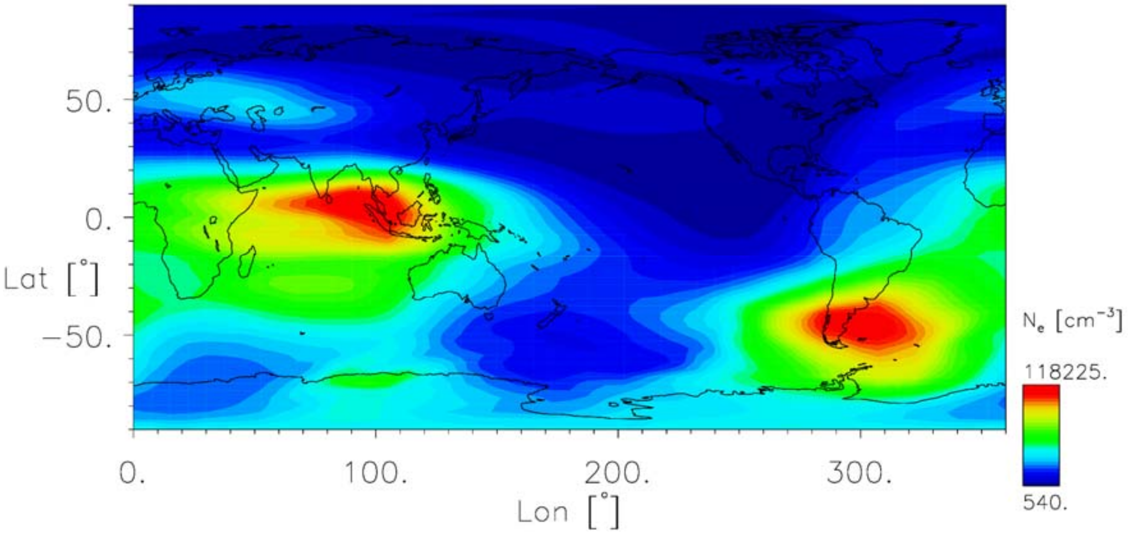

Figure 22. The electron density of the ionosphere at altitude 844 km varies with latitude and longitude on January 2, 2012 at 12:00:00 UTC. From [27].

Notice the severe dependency of N_e on the time of day. As the Earth rotates a half-revolution in the 12-hour interval between these two snapshots, those longitudes with areas of high electron density (red) shift to areas of low electron density (blue), and vice versa. Note further that high electron density regions are mostly grouped around equatorial latitudes. Since there are such large variations in N_e, we design for the worst-case scenario. Here, the highest electron density induces the longest group delay, so we select the highest measured electron density in either sample to characterize the ionosphere, namely $N_e = 172500\ \text{cm}^{-3} = 1.725\times10^{11}\ \text{m}^{-3}$.

Under these basic assumptions, the average total electron content of the ionosphere is evaluated from (77) as

$$T_{ec} = \left(1.725\times10^{11}\ \text{m}^{-3}\right)\left(975\times10^{3}\ \text{m}\right) = 1.682\times10^{17}\ \text{m}^{-2}. \tag{78}$$

We now evaluate (74) for the average group delay due to ionospheric propagation at the GPS L1-band operating frequency of 1575.42 MHz:

$$\begin{aligned}\Delta\tau_g &\simeq \frac{1}{8\pi^2}\left(\frac{e^2}{\varepsilon_0 m_e c_0}\right)\frac{T_{ec}}{f^2}\\ &= \frac{1}{8\pi^2}\left[\frac{\left(1.602\times10^{-19}\ \text{C}\right)^2}{\left(8.854\times10^{-12}\ \text{F/m}\right)\left(9.109\times10^{-31}\ \text{kg}\right)\left(2.998\times10^{8}\ \text{m/s}\right)}\right]\times\\ &\qquad\left[\frac{\left(1.682\times10^{17}\ \text{m}^{-2}\right)}{\left(1.57542\times10^{9}\ \text{Hz}\right)^2}\right]\\ &= 9.110\ \text{ns}.\end{aligned} \tag{79}$$

This average group delay is used to characterize the exponentially-distributed time delay noise $\delta_{\tau i} \sim Exp\left(\lambda = \left(9.110\ \text{ns}\right)^{-1}\right)$.

We now complete the time-domain noise model for high-altitude satellites. The noisy TOA equation given in (56) may be expressed as

$$\tau_i = \frac{\overbrace{\left\|\boldsymbol{r}_e - \boldsymbol{r}_i\right\|}^{\text{deterministic}}}{c_0} + \overbrace{Exp\left(\lambda = \left(9.110\ \text{ns}\right)^{-1}\right)}^{\text{random}}. \tag{80}$$

Similarly, the noisy TDOA equation given in (59) may be expressed as

$$\tau_{ij} = \overbrace{\frac{1}{c_0}\left(\left\|\boldsymbol{r}_e - \boldsymbol{r}_i\right\| - \left\|\boldsymbol{r}_e - \boldsymbol{r}_j\right\|\right)}^{\text{deterministic}} + \overbrace{\left(Exp\left(\lambda = (9.110\text{ ns})^{-1}\right) - Exp\left(\lambda = (9.110\text{ ns})^{-1}\right)\right)}^{\text{random}}. \quad (81)$$

b. Doppler Variation Characterization

The ionosphere also impacts the Doppler shift of a beacon signal via two primary mechanisms: refraction and phase alterations due to the complex refractive index of the ionosphere as detailed by the Appleton-Hartree equation. In fact, the frequency shift exerted by the ionosphere on a signal may be expressed in similar terms as the previously-discussed group delay $\Delta\tau_g$ (see Equation 74) [28]:

$$\Delta f_{ion} \simeq -\frac{1}{8\pi^2}\left(\frac{e^2}{\varepsilon_0 m_e c_0}\right)\left(\frac{1}{f_0}\right)\frac{d}{dt}\left(T_{ec}\right). \quad (82)$$

The time-derivative of the total electron content implies that the ionospheric Doppler shift is nonzero only when T_{ec} is a time-varying quantity. We also note that Δf_{ion} is inversely proportional to the operating frequency f_0. Thus, ideally, higher operating frequencies will suffer less from ionospheric Doppler shifts.

Willman has collected experimental data on the ionospheric Doppler shift due to refraction. For a satellite signal transiting the ionosphere at an operating frequency of 54 MHz, he recorded a maximum Doppler shift of 40 Hz [29]. This is the worst-case scenario he recorded. We scale this error to the GPS operating frequency of 1575.42 MHz according to the inverse-frequency dependency of (82):

$$\Delta f'_{ion} = \left(\frac{f''_0}{f'_0}\right)\Delta f''_{ion} = \left(\frac{54\text{ MHz}}{1575.42\text{ MHz}}\right)\left(40\text{ Hz}\right) = 1.371\text{ Hz}. \quad (83)$$

Let us assume this ionospheric Doppler shift is the standard deviation of the zero-mean Doppler shift noise variables δ_{fi} in (63) and δ_{fj} in (64).

We complete the frequency-domain noise model for high-altitude satellite sensors. The noisy FDOA equation given in (65) may be expressed as

$$\Delta f_{ij} = \overbrace{\frac{f_0}{c_0}\left(v_{ei}^{\hat{i}} - v_{ej}^{\hat{i}}\right)}^{\text{deterministic}} + \overbrace{\left(N\left(0,\left(1.371\text{ Hz}\right)^2\right) - N\left(0,\left(1.371\text{ Hz}\right)^2\right)\right)}^{\text{random}}. \tag{84}$$

The noisy FDOA measurement may be alternatively expressed in condensed notation as

$$\Delta f_{ij} \sim N\left(\frac{f_0}{c_0}\left(v_{ei}^{\hat{i}} - v_{ej}^{\hat{i}}\right), 2\left(1.371\text{ Hz}\right)^2\right). \tag{85}$$

2. Low-altitude Sensors

An alternative to deploying a permanent satellite constellation is using mobile UAVs or other airborne platforms as geolocation sensors. While such systems do not have the longevity or coverage area of a satellite constellation, low-altitude sensors have the advantage in flexibility and maneuverability. If the ionosphere was the main propagation concern for GHz-range satellite links, multipath fading is the primary mechanism of signal degradation for low-altitude sensors. As with all wireless communications links, the unique characteristics of the environment have a severe impact on signal propagation. Unlike ionospheric distortion, which was highly variable yet relatively predictable using forecast models like GAIM, multipath fading is highly variable and very difficult to predict. Significant research has been directed toward modeling multipath effects on delay spread and Doppler spread. Analytical solutions are far too complicated for practical usage. Instead, numerical computations or empirical approximations are typically used to estimate multipath effects [20]. Here, we turn to the literature to gather reasonable multipath parameters for low-altitude UAV communications links.

For the following discussion, we assume all sensors are UAVs at an altitude of 10,000 ft (3,048 m) and traveling at a cruising speed of 100 knots (51.44 m/s). All pertinent sensor communications operate within the unlicensed industrial, scientific, and medical (ISM) band at 2.4 GHz. The emitter is assumed stationary.

a. Time Delay Variation Characterization

As a signal propagates radially from a transmitter, some portion of the signal power propagates along the LOS path and some is lost due to spherical spreading of the wave in the medium. When the environment is filled with objects to reflect, scatter, and diffract this wayward signal power, some may be redirected back toward the intended receiver. Upon arrival, there will be an associated time delay due to the circuitous path taken en route. The resulting difference in propagation delay between the LOS signal and the multipath signal is termed the delay spread. Let us define the root-mean-square (RMS) delay spread as [30]

$$\Delta\tau_s = \sqrt{\frac{\sum_{n=1}^{N} \beta_n \left(\tau_{s,n} - \overline{\tau}_s\right)^2}{\sum_{n=1}^{N} \beta_n}}, \tag{86}$$

where τ_s is the delay spread, β is the signal power versus delay profile, and $\overline{\tau}_s$ is the mean delay spread value defined as [30]

$$\overline{\tau}_s = \frac{\sum_{n=1}^{N} \beta_n \tau_{s,n}}{\sum_{n=1}^{N} \beta_n}. \tag{87}$$

Newhall et al. collected experimental data for delay spread of a 2 GHz signal versus elevation angle above the horizon. They found that delay spread falls off significantly as the elevation angle increases, suggesting a large dependence on the high concentration of particulate matter in the atmosphere at low altitudes. At a maximum elevation angle of 30° above the horizon, they observed an average RMS delay spread of 18.3 ns [30]. For this model, we shall exclude such low elevation angles for the sake of accuracy. At higher elevation angles—nearer to vertical-path propagation than 30°—the delay spread is assumed to further decrease. Accordingly, we choose an average RMS delay spread of $\Delta\tau_s = 10 \text{ ns}$ to characterize the time domain signal delay variation.

For low altitude UAVs, the noisy TOA equation given in (56) may then be expressed as

$$\tau_i = \overbrace{\frac{\left\|\boldsymbol{r}_e - \boldsymbol{r}_i\right\|}{c_0}}^{\text{deterministic}} + \overbrace{Exp\left(\lambda = \left(10 \text{ ns}\right)^{-1}\right)}^{\text{random}}. \tag{88}$$

The noisy TDOA equation given in (59) may be similarly expressed as

$$\tau_{ij} = \overbrace{\frac{1}{c_0}\left(\left\|\boldsymbol{r}_e - \boldsymbol{r}_i\right\| - \left\|\boldsymbol{r}_e - \boldsymbol{r}_j\right\|\right)}^{\text{deterministic}} + \overbrace{\left(Exp\left(\lambda = (10\text{ ns})^{-1}\right) - Exp\left(\lambda = (10\text{ ns})^{-1}\right)\right)}^{\text{random}}. \tag{89}$$

b. Doppler Variation Characterization

Consider a UAV with onboard accelerometers and inertial navigation equipment that has a speed estimation tolerance of $\pm 0.1\ \%$. At a cruising speed of 100 knots (51.44 m/s), this corresponds to a speed uncertainty of $\pm 0.0514\text{ m/s}$. If we assume the worst-case scenario where the sensor is moving directly toward or away from the stationary emitter, (32) gives an average Doppler variation due to speed uncertainty of

$$\Delta f_D = \frac{f_0}{c_0}\left(v_{tr}^{\hat{i}}\right) = \frac{\left(2.4\times 10^9\text{ Hz}\right)}{\left(2.998\times 10^8\text{ m/s}\right)}\left(\pm 0.0514\text{ m/s}\right) = \pm 0.412\text{ Hz}. \tag{90}$$

As discussed previously, we assume the Doppler variation about the deterministic mean value to be Gaussian-distributed. Let us use this Doppler variation as the standard deviation of the zero-mean IID random variables δ_{fi} and δ_{fj}.

We may thus rewrite the noisy FDOA equation given in (65) as

$$\Delta f_{ij} = \overbrace{\frac{f_0}{c_0}\left(v_{ei}^{\hat{i}} - v_{ej}^{\hat{i}}\right)}^{\text{deterministic}} + \overbrace{\left(N\left(0,(0.412\text{ Hz})^2\right) - N\left(0,(0.412\text{ Hz})^2\right)\right)}^{\text{random}}. \tag{91}$$

If the deterministic FDOA component is considered a constant bias, the total FDOA measurement may also be expressed in condensed notation as

$$\Delta f_{ij} \sim N\left(\frac{f_0}{c_0}\left(v_{ei}^{\hat{i}} - v_{ej}^{\hat{i}}\right), 2\left(0.412\text{ Hz}\right)^2\right). \tag{92}$$

THIS PAGE INTENTIONALLY LEFT BLANK

VI. SYNTHETIC APERTURE: TOA

A. OVERVIEW

The principle of a synthetic aperture is straightforward. A series of measurements or data samples in time are compiled together in such a way as to yield a refined high-resolution measurement. The implementation of the synthetic aperture concept is often more nuanced. Significant research in the past fifty years has been devoted to using synthetic apertures in various fields. Airborne radar systems implement SAR techniques as they fly over a target of interest [31]. Synthetic aperture sonar (SAS) is used in maritime environments to generate high-quality underwater imagery. As a vessel travels along the ocean, it collects sonar returns at either regular or irregular intervals. These returns are subsequently synthesized using a SAS algorithm to provide a refined image of the underwater environment [32]. The synthetic aperture concept has made inroads as well with the medical ultrasound imaging field. Synthetic aperture ultrasound images are refined enough to capture blood flow within an organism [33]. We aim to replicate the synthetic aperture principle in geolocation algorithms.

B. SOLUTION STRATEGY

Recall from Chapter II that two TOA sensors in three-dimensional space can localize an emitter position to a circular curve, namely the intersection curve between the two TOA spheres (see Figure 5). The TOA algorithm is unique in this sense; for any spatial sensor orientation, the circular solution curve may always be defined analytically. We exploit this fact in the following heuristic solution strategy for the synthetic aperture TOA problem.

1. Parametric Circular Solutions

An analytically-defined curve may be efficiently adapted to a discrete numerical computation environment through parametric expression. As discussed above, at any given time step, two TOA sensors can localize an emitter to a circular curve in three-dimensions. Thus, one must know the parametric equation governing the circular emitter curve.

A circle with center coordinates given by the position vector $\boldsymbol{r}_c$ and radius ρ may be expressed in terms of the parameter t by the three-dimensional position vector

$$\boldsymbol{p}(t) = \boldsymbol{r}_c + \rho\cos(t)\hat{\boldsymbol{u}} + \rho\sin(t)\hat{\boldsymbol{v}}, \tag{93}$$

where $\hat{\boldsymbol{u}}$ and $\hat{\boldsymbol{v}}$ are arbitrary orthogonal unit vectors parallel with the plane in which the circle lies [34]. Let this plane be characterized by the unit normal vector $\hat{\boldsymbol{k}}$. It then follows that

$$\hat{\boldsymbol{k}} = \pm(\hat{\boldsymbol{u}} \times \hat{\boldsymbol{v}}), \tag{94}$$

where the $(\cdot)\times(\cdot)$ operator denotes the cross product. Note that (93) is periodic with respect to parameter t. Thus, we can fully define the circle while restricting t to the domain $[0°, 360°)$. A generic diagram of such a parameterized circle is given in Figure 23.

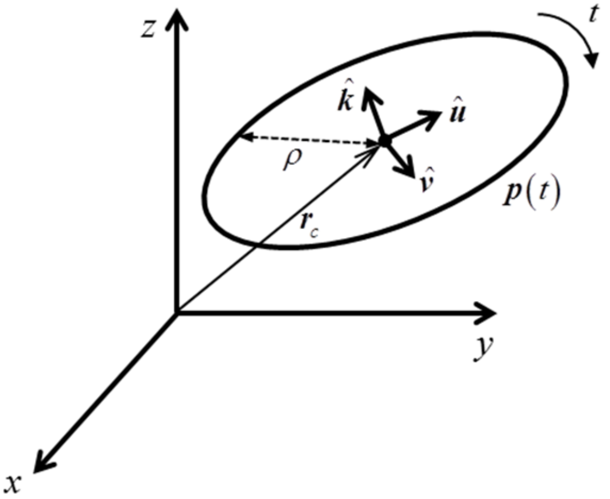

Figure 23. A generic circle in three dimensions is shown as the parametrically-defined position vector $\boldsymbol{p}(t)$.

The next task is to generally express the two-sensor TOA solution in its parametric form. Accordingly, the circle radius, center coordinates, and unit vectors are required. Consider the following noise-free scenario. Two TOA sensors s_1 and s_2 are located at the three-dimensional coordinates specified by the position vectors $\boldsymbol{r}_1$ and $\boldsymbol{r}_2$, respectively. The unit vector $\hat{\boldsymbol{r}}_{21}$ points in the direction from sensor s_1 to sensor s_2. An emitter e generates a beacon signal while located at the coordinates specified by the position vector $\boldsymbol{r}_e$. The sensors receive the TOA signal and calculate the corresponding TOA spheres. From the TOA measurements, the scalar range values $\|\boldsymbol{r}_{e1}\|$ and $\|\boldsymbol{r}_{e2}\|$ are defined according to Equation 1. A cross-section of this three-dimensional scenario is taken such that the cross-sectional plane contains both sensors and the emitter. Such a plane is shown in Figure 24.

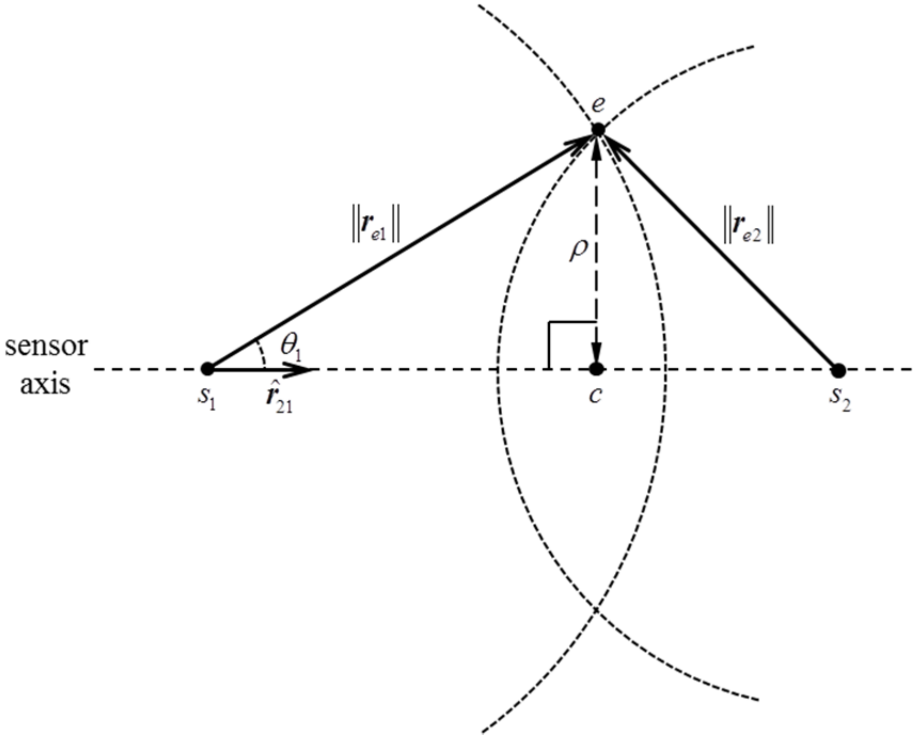

Figure 24. A cross-sectional plane of a two-sensor TOA solution is shown.

The circular solution is the path traced by the point e when revolved about the sensor axis. Therefore, ρ denotes the radius of the circular solution, and the point c denotes the center of the solution circle. To express these parameters in terms of known quantities, we first apply the law of cosines:

$$\|\boldsymbol{r}_{e2}\|^2 = \|\boldsymbol{r}_2 - \boldsymbol{r}_1\|^2 + \|\boldsymbol{r}_{e1}\|^2 - 2\|\boldsymbol{r}_{e1}\|\|\boldsymbol{r}_2 - \boldsymbol{r}_1\|\cos\left(\theta_1\right). \tag{95}$$

Bounded on the range $\left[0°,180°\right]$, the angle θ_1 may be expressed as

$$\theta_1 = \arccos\left(\frac{\|\boldsymbol{r}_2 - \boldsymbol{r}_1\|^2 + \|\boldsymbol{r}_{e1}\|^2 - \|\boldsymbol{r}_{e2}\|^2}{2\|\boldsymbol{r}_{e1}\|\|\boldsymbol{r}_2 - \boldsymbol{r}_1\|}\right). \tag{96}$$

The circular radius is then given as

$$\rho = \|\boldsymbol{r}_{e1}\|\sin\left(\theta_1\right), \tag{97}$$

and the position vector of the circle center is given as

$$\boldsymbol{r}_c = \boldsymbol{r}_1 + \left[\|\boldsymbol{r}_{e1}\|\cos\left(\theta_1\right)\right]\hat{\boldsymbol{r}}_{21}. \tag{98}$$

To define the required parameterization unit vectors, we first observe that the solution circle lies in the plane perpendicular to the sensor axis. Therefore, we choose

$$\hat{\boldsymbol{k}} = \hat{\boldsymbol{r}}_{21}. \tag{99}$$

We now must choose two additional unit vectors $\hat{\boldsymbol{u}}$ and $\hat{\boldsymbol{v}}$ that lie within the plane of the circle and are mutually orthogonal with $\hat{\boldsymbol{k}}$. There is an infinitude of such combinations, so we arbitrarily choose $\hat{\boldsymbol{u}}$ such that it has a *z*-component of zero. This implies that

$$\hat{\boldsymbol{u}} \cdot \hat{\boldsymbol{r}}_{21} = \left(\hat{u}_x\hat{\boldsymbol{x}} + \hat{u}_y\hat{\boldsymbol{y}} + 0\hat{\boldsymbol{z}}\right) \cdot \left(\hat{r}_{21x}\hat{\boldsymbol{x}} + \hat{r}_{21y}\hat{\boldsymbol{y}} + \hat{r}_{21z}\hat{\boldsymbol{z}}\right) = 0. \tag{100}$$

It may be shown (see Appendix) that one of two real roots for $\hat{\boldsymbol{u}}$ is given as

$$\hat{\boldsymbol{u}} = \left(-\sqrt{\frac{\hat{r}_{21y}{}^2}{\hat{r}_{21x}{}^2 + \hat{r}_{21y}{}^2}}\right)\hat{\boldsymbol{x}} + \left(\sqrt{\frac{\hat{r}_{21x}{}^2}{\hat{r}_{21x}{}^2 + \hat{r}_{21y}{}^2}}\right)\hat{\boldsymbol{y}} + \left(0\right)\hat{\boldsymbol{z}}. \tag{101}$$

Lastly, the unit vector $\hat{\boldsymbol{v}}$ may be defined as

$$\hat{\boldsymbol{v}} = \hat{\boldsymbol{u}} \times \hat{\boldsymbol{k}}, \tag{102}$$

where $\hat{\boldsymbol{k}}$ and $\hat{\boldsymbol{u}}$ are given in (99) and (101) in terms of known quantities. We can now fully express the parameterization of a circular TOA solution curve in the form of (93) using known, assumed, or measured quantities.

Recall that the discussion so far has pertained only to one single instance in time. If the position vector $\boldsymbol{p}_n$ describes the circular solution of two TOA measurements at a given time step n and no noise affects the system, then there is some parameter value t'_n for which $\boldsymbol{p}_n\left(t'_n\right)$ accurately specifies the emitter position. To determine the specific value of t'_n, we shall use the subsequent circular solution at time step $n+1$.

2. Circular Intersections

The synthetic aperture concept presupposes that data from two or more distinct instances in time may be compiled in such a way as to refine the overall solution. In the context of the TOA algorithm, this involves finding the intersection of two or more circles in three-dimensional space. With the known parametric equations of subsequent circular emitter curves in time, this is simply a matter of solving for the theoretical parameter values of t'_n and t'_{n+1} for which $\boldsymbol{p}_n\left(t'_n\right)=\boldsymbol{p}_{n+1}\left(t'_{n+1}\right)$.

The process is more complicated when noise is introduced into the system. Now, subsequent noisy circular emitter curves do not necessarily contain the exact coordinates of the emitter and do not necessarily intersect one another. We circumvent this issue in our algorithm by finding the nearest two points on the two circles. This is accomplished using numerical computation; we perform an exhaustive search through all values of t_n and t_{n+1} to find the parameter pair $\left(t''_n, t''_{n+1}\right)$ such that

$$\left\|\boldsymbol{p}_n\left(t''_n\right)-\boldsymbol{p}_{n+1}\left(t''_{n+1}\right)\right\|=\min\left[\left\|\boldsymbol{p}_n\left(t_n\right)-\boldsymbol{p}_{n+1}\left(t_{n+1}\right)\right\|\right]. \tag{103}$$

Note that we designate this parameter pair with double-primed notation to emphasize that the associated points do not necessarily intersect. There is some inherent quantization error introduced into the problem since this search is implemented numerically; however, if a sufficiently large number of samples is used to discretize the parameters t_n and t_{n+1}, then the quantization error becomes negligible compared with the effect of the noise due to time delay of the TOA beacon signal.

To compute the estimated position of the emitter, we now find the midpoint of the two nearest points on the two circles. Let us represent the estimated emitter coordinates based on measurements at time steps n and $n+1$ with the position vector $\boldsymbol{r}''_{e,n}$, defined as

$$\boldsymbol{r}''_{e,n} = \frac{\boldsymbol{p}_n\left(t''_n\right)+\boldsymbol{p}_{n+1}\left(t''_{n+1}\right)}{2}. \tag{104}$$

For a synthetic aperture composed of N time steps, the refined emitter location estimate $\boldsymbol{r}''_e$ is computed as the spatial centroid of all $N-1$ available $\boldsymbol{r}''_{e,n}$ estimates. Mathematically, we express the refined estimate as

$$\boldsymbol{r}''_e = \frac{1}{N-1}\sum_{n=1}^{N-1}\boldsymbol{r}''_{e,n}. \tag{105}$$

This refined emitter estimate is the result of the synthetic aperture TOA algorithm.

3. RMS Error

To assess the performance of the algorithm under various sensor orientations and synthetic aperture sizes, we must quantify the associated error performance for a given noise profile. The distance error of a single synthetic aperture estimate relative to the true emitter position is given as

$$d = \left\|\boldsymbol{r}''_e - \boldsymbol{r}_e\right\|. \tag{106}$$

To characterize the general noise performance, it is customary to consider the theoretical MSE of our estimator algorithm, which is defined as

$$\text{MSE} = E\left[d^2\right] = E\left[\left\|\boldsymbol{r}''_e - \boldsymbol{r}_e\right\|^2\right], \tag{107}$$

where $E\left[\cdot\right]$ denotes the expected value operator [35]. The MSE here carries the units of square meters and has limited physical significance. A quantity of more relevance is the root-mean-square error (RMSE) and is simply given by

$$\text{RMSE} = \sqrt{\text{MSE}} = \sqrt{E\left[d^2\right]}. \tag{108}$$

The RMSE carries units of meters and is more useful for physical reference.

Ideally, the RMSE of an estimator algorithm is determined analytically, and the expected value operation is evaluated in closed form. For complicated estimators, this is increasingly difficult. Instead, the expected value operation is frequently approximated by the average squared error over many independent trials. In our numerical computation, we assume the approximation

$$\mathrm{RMSE} \approx \sqrt{\frac{1}{M}\sum_{m=1}^{M} {d_m}^2} \tag{109}$$

holds for sufficiently large M.

C. RESULTS

Consider the following scenario. A stationary emitter e is located at the coordinate system origin and generates a TOA beacon signal. Two TOA sensors s_1 and s_2 are initially located at the Cartesian coordinates $(-b-\Delta b, -b, h)$ and $(-b, -b, h)$, respectively. Each sensor travels at the same speed v_s; the direction of the sensor velocities $\boldsymbol{v}_1$ and $\boldsymbol{v}_2$ may vary. Over time, the two sensors collect N total noisy TOA measurements for inclusion in the synthetic aperture estimate—we refer to this parameter as the size of the synthetic aperture. The time delay standard deviation $\sigma_{\tau 21}$ is incorporated into the TOA measurement as detailed in Chapter V. The constant time interval between measurements ΔT_{SA} is chosen such that, at the end of the total synthetic aperture time duration $T_{SA} = (N-1)\Delta T_{SA}$, the sensors have traveled distance $2b$. This necessitates that

$$b = \frac{v_s (N-1)\Delta T_{SA}}{2}. \tag{110}$$

Establishing a generalized setup geometry such as this allows us to maintain some comparability between the following simulations run against different system variables.

Three primary variables are considered in this discussion: the angular spread between sensor velocities $\boldsymbol{v}_1$ and $\boldsymbol{v}_2$, the size N of the synthetic aperture, and the altitude h of the geolocation sensors. Two distinct cases for sensor altitude—satellites at altitude 19,100 km and of UAVs at altitude 10,000 ft (3,048 m)—are simultaneously presented in the following two sections regarding sensor velocity angular spread and synthetic aperture size.

1. Sensor Velocity Angular Spread

The sensor velocity angular spread refers to the angle α between the sensor velocities $\boldsymbol{v}_1$ and $\boldsymbol{v}_2$. It may be defined in terms of a dot product as

$$\alpha = \arccos\left(\frac{\boldsymbol{v}_1 \cdot \boldsymbol{v}_2}{\|\boldsymbol{v}_1\|\|\boldsymbol{v}_2\|}\right) = \arccos\left(\frac{\boldsymbol{v}_1 \cdot \boldsymbol{v}_2}{{v_s}^2}\right), \tag{111}$$

if α is confined to the range $[0°, 180°]$. Thus, to sweep through a range of spread angles, we must vary one or both of the sensor velocity directions.

Let us choose a fixed sensor velocity $\boldsymbol{v}_1 = v_s \hat{\boldsymbol{y}}$. To vary the spread angle, we define the variable sensor velocity

$$\boldsymbol{v}_2 = v_s \sin(\alpha)\, \hat{\boldsymbol{x}} + v_s \cos(\alpha)\, \hat{\boldsymbol{y}}, \tag{112}$$

with α set to vary on the range $[0°, 90°]$. A top-down view of this scenario is diagramed for illustrative purposes in Figure 25.

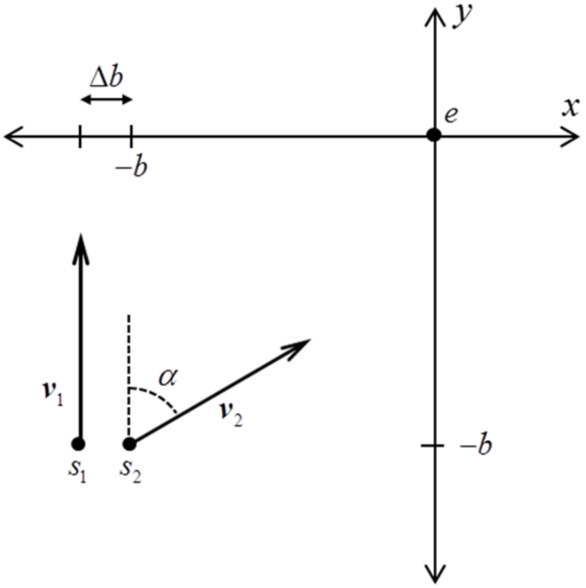

Figure 25. The generic sensor velocity angular spread scenario is diagramed.

The TOA circular emitter curve generated from each pair of TOA measurements collected at a given time step is discretized using 20,000 sample points. To further boost the resolution of the estimated position and improve on computation time, we impose a maximum altitude $h_{\max}$ on the emitter search domain. This constraint effectively condenses the 20,000 sample points on the TOA circle to the region of interest rather than wasting computation time by considering points known to be very far from the true solution. If the emitter is known to be at high altitudes, $h_{\max}$ and the number of sample points may be increased at the expense of computational efficiency. The principle is illustrated in Figure 26; black dots represent discretized sample points on the TOA circle, and the red dot is the true emitter position.

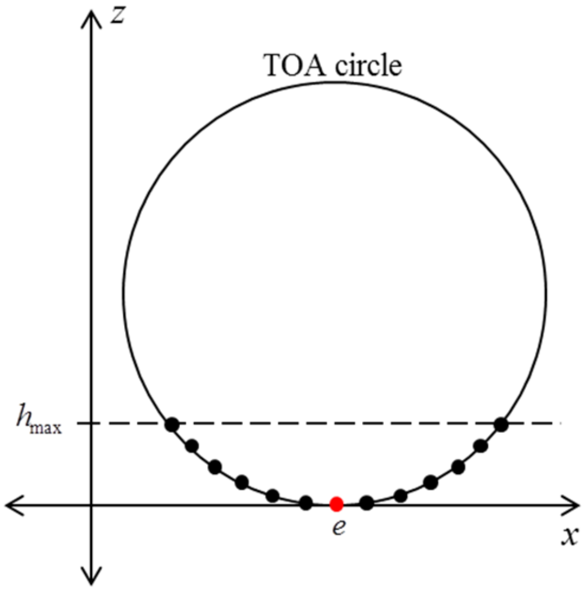

Figure 26. An altitude constraint is imposed on the TOA emitter search, condensing the search to an area of interest.

The synthetic aperture time intervals ΔT_{SA} were chosen according to the following process. A maximum total synthetic aperture duration time T_{SA} for satellite sensors was set to 15 minutes. With $N = 5$ aperture samples, we find that $\Delta T_{SA} = 225$ seconds for satellite sensors. To ensure that the system geometry is comparable for UAV sensors, the time interval was scaled according to sensor altitude and velocity to keep the swath angle of the sensors constant (see Appendix for details on scaling and swath angle). The result is that, for $N = 5$ aperture samples, ΔT_{SA} is 2.72 seconds for UAV sensors. Other pertinent simulation parameters have been collected and organized below in Table 1.

Table 1. Angular spread simulation parameters are given for the synthetic aperture TOA algorithm.

Parameter (units)	**Satellite Sensors**	**UAV Sensors**
h (m)	19.10×10^6	3.048×10^3
v_s (m/s)	3.889×10^3	51.44
α (degrees)	variable on [0,90]	variable on [0,90]
N (samples)	5	5
ΔT_{SA} (s)	225	2.72
b (m)	1.750×10^6	280.1
Δb (m)	1000	100
$\sigma_{\tau 21}$ (ns)	9.11	10.0
$h_{\max}$ (m)	5000	1000

Each simulation was run under two noise conditions. A high-noise environment was simulated using the time delay standard deviation $\sigma_{\tau 21}$ listed in Table 1. To model a low-noise environment, the standard deviation is reduced to 10% of the listed value. This can model a nighttime environment with minimal solar agitation and disturbance in the ionosphere for the satellite scenario. For the UAVs, at nighttime, thermal convection currents in the lower atmosphere may be less pronounced and, thus, have a smaller impact on the delay of a radio frequency (RF) signal. In all cases, we iterate the algorithm ten times to help generate an approximation of the RMSE. More iterations are preferable, but the significant computation time of the algorithm made this prohibitive.

a. Satellite Sensors

The RMSE for the synthetic aperture TOA algorithm applied to satellite sensors is plotted against sensor velocity spread angle α in Figure 27. All data points are plotted as circles centered on the data value, and all traces between data points are generated using basic linear interpolation. We do not apply any regression analysis since the sample size is so limited.

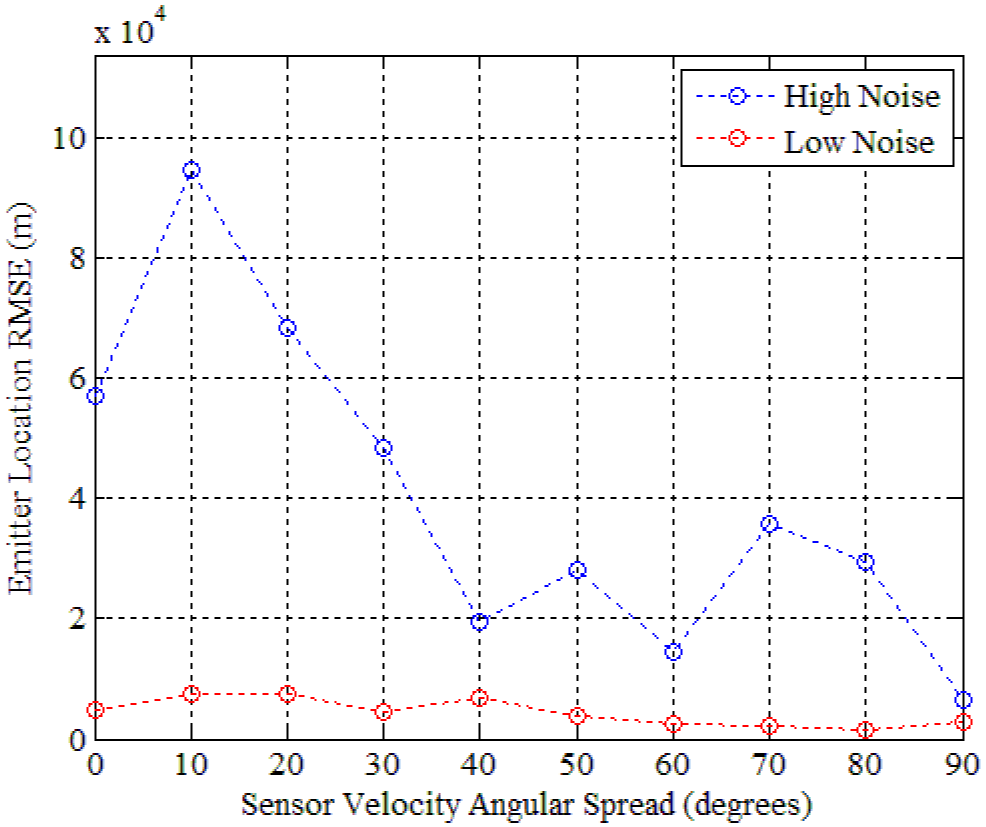

Figure 27. RMSE is plotted against sensor velocity angular spread α for satellite sensors. Dashed traces are linear interpolations between adjacent data points.

These satellite sensor simulation results highlight several important characteristics of the synthetic aperture TOA algorithm. Note the order of magnitude variation in the high-noise trials as the sensor velocity spread angle is varied. Also, observe the general trend of decreasing RMSE with increasing spread angle. This suggests a significant algorithm dependency on the spatial orientation and movement of the TOA sensors. On the whole, a large spread angle between the sensors is preferable. This brings the sensor paths closer to orthogonal directions, boosting the potential spatial resolution of the TOA measurements.

It should be mentioned that an RMSE on the order of 10^4 m renders the emitter estimate effectively useless for any high-accuracy geolocation applications. We suspect that the variability in the TOA measurements due to ionospheric propagation is simply too large for accurate estimation. For beacon signal propagation over distances of more than 19,100 km, small measurement deviations of 9.11 ns are amplified significantly. This speculation is validated by the drastic reduction in RMSE for the low-noise trials with 10% of the time delay standard deviation. This low-noise condition may be the result of atmospheric conditions, such as nighttime operation, or may be the result of time delay variation compensation. Systems such as the GNSS use the secondary L2 band at 1227.6 MHz to boost the accuracy of the TOA measurement [23]. The overall effect is a reduction in the random nature of the TOA measurement, corresponding to a lower time delay standard deviation and lower RMSE. Such compensation techniques may be incorporated into this model in the future using forecast models such as those hosted by the CCMC to predict the true time delay characteristics of the ionosphere [18]. Rather than aggregating all ionospheric effects simultaneously in a single worst-case random variable, the system could be modified to adapt and dynamically calibrate in response to current ionospheric conditions.

An inherent source of error in these results follows from the discretized parametric solution strategy used. Each TOA circle was discretized below the set maximum altitude $h_{\max} = 5{,}000$ m using 20,000 sample points. As with any numerical solution, we have a small-scale variation due to quantization and rounding errors. We consider this as a minor effect in the above satellite sensor results in light of a final source of uncertainty.

A final consideration that applies to all results included in this research is that the RMSE is approximated here using ten independent trials. Ideally, to approximate the expected value operation embedded within the RMSE definition (see Equations (108) and (109)), something on the order of 10^5 or 10^6 independent trials should be used. Here, due to the practical limitations of long compute times, we were only able to simulate ten trials. Practically, this implies that the RMSE traces given in Figure 27 contain some undesired variation in the data due to the limited sample size of this stochastic process. This is the likely cause of the small-scale variations between data points. If more computational resources—including both hardware and time—were available to increase the number of iterations as well as decrease the spread angle step size, we anticipate that curves above would be smoother and lack the high-frequency deviations seen between adjacent data points.

b. UAV Sensors

The RMSE for the synthetic aperture TOA algorithm applied to UAV sensors is plotted against sensor velocity spread angle α in Figure 28.

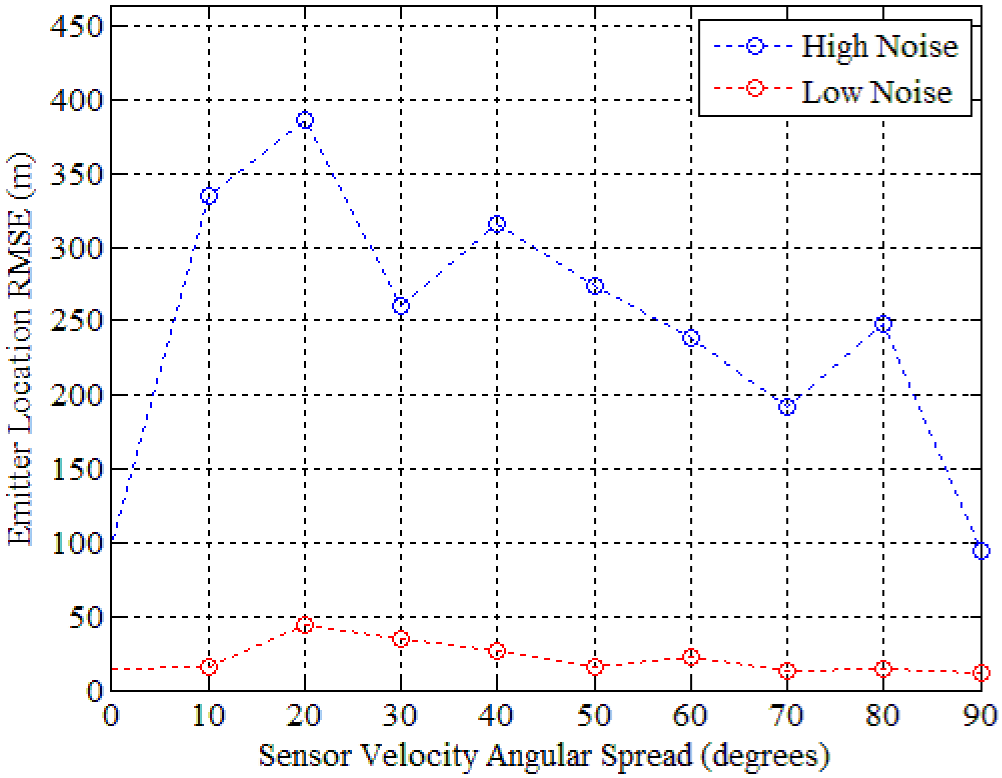

Figure 28. RMSE is plotted against sensor velocity angular spread α for UAV sensors. Dashed traces are linear interpolations between adjacent data points.

The simulation results for UAV sensors maintain similar characteristics with the satellite sensor results. Both contain uncertainties arising from inherent quantization errors and the practical computational limits of the simulation. On the whole, as with the satellites, a larger spread angle α corresponds to a lower RMSE. The one notable anomaly is at $\alpha = 0°$, which corresponds to the case when the sensors travel parallel to one another. It is unclear what part of the synthetic aperture TOA algorithm would favor system performance at such a condition over and against the case with $\alpha = 10°$. Further investigation of this phenomenon is needed.

Again, we see a pronounced drop in the RMSE for the low-noise condition. For the UAV scenario, we observe an RMSE below 50 m for all spread angles. At a minimum, the RMSE drops to 12.0 m when $\alpha = 90°$. Even without specific time delay variation compensation measures, geolocation estimates accurate to within 12.0 m are very useful. Certainly for applications such as personal navigation or altitude estimation, this accuracy rating is sufficient.

2. Aperture Size

We next consider the performance of the synthetic aperture algorithm against the size of the aperture. The number of aperture samples is varied from $N = 2$—the minimum requirement to generate an emitter estimate—up to a maximum aperture size $N = N_{\max}$. As the number of aperture samples N increases, the time interval between samples ΔT_{SA} is reduced so as to hold the swath angle traced by the sensors constant. Mathematically, we may write

$$\Delta T_{SA} = \left(\frac{N_{\max} - 1}{N - 1} \right) \Delta T_{SA,\min}, \tag{113}$$

where $\Delta T_{SA,\min}$ is the minimum aperture time interval associated with the largest number of aperture samples $N_{\max}$. A diagram illustrating the variable synthetic aperture size is given in Figure 29. In the diagram, black dots represent the sample times.

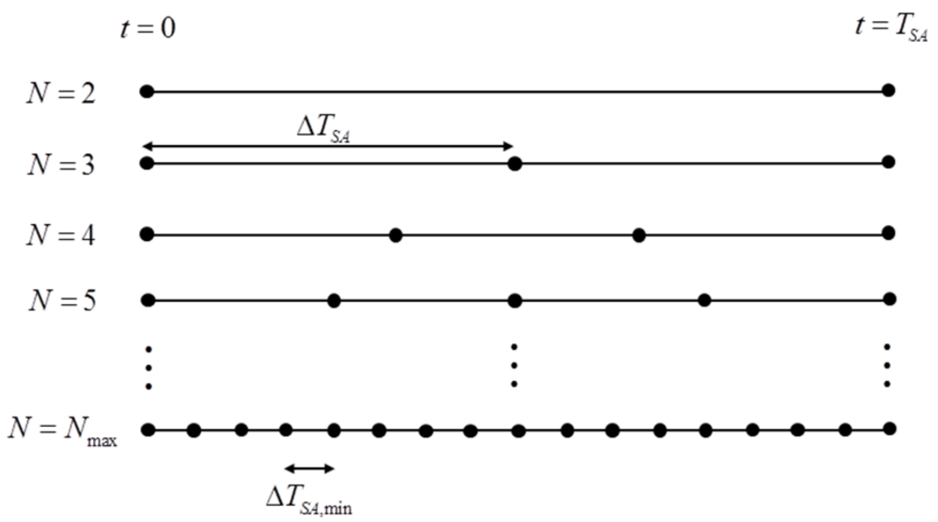

Figure 29. The synthetic aperture time interval ΔT_{SA} decreases with increasing synthetic aperture size N . Black dots represent sample times.

As before, 20,000 sample points are used to discretize each TOA solution circle. An altitude constraint is applied for the sake of estimate resolution and reduced computation time. The low-noise condition again corresponds to a time delay standard deviation equal to 10% of the high-noise condition value σ_τ . Other pertinent simulation parameters are listed in Table 2.

Table 2. Aperture size simulation parameters are given for the synthetic aperture TOA algorithm.

Parameter (units)	**Satellite Sensors**	**UAV Sensors**
h (m)	19.10×10^{6}	3.048×10^{3}
v_s (m/s)	3.889×10^{3}	51.44
α (degrees)	45	45
$N_{\max}$ (samples)	50	50
N (samples)	variable on [2,15]	variable on [2,15]
$\Delta T_{SA,\min}$ (s)	64.3	0.778
b (m)	1.750×10^{6}	280.1
Δb (m)	1000	100
$\sigma_{\tau 21}$ (ns)	9.11	10.0
$h_{\max}$ (m)	5000	1000

a. Satellite Sensors

The RMSE for the synthetic aperture TOA algorithm applied to satellite sensors is plotted against synthetic aperture size N in Figure 30. Note that we do not plot results for synthetic aperture size $N < 2$. Recall that the minimum requirement for the synthetic aperture algorithm is to have more than one measurement in time. With only one sample point in the aperture, we have a single TOA circle at that given time. We know the emitter lies somewhere on the circle in the noiseless case, or near the circle in the noisy case, but we cannot refine the search beyond this. There is insufficient data. Thus, we begin all plots with the synthetic aperture size with $N = 2$.

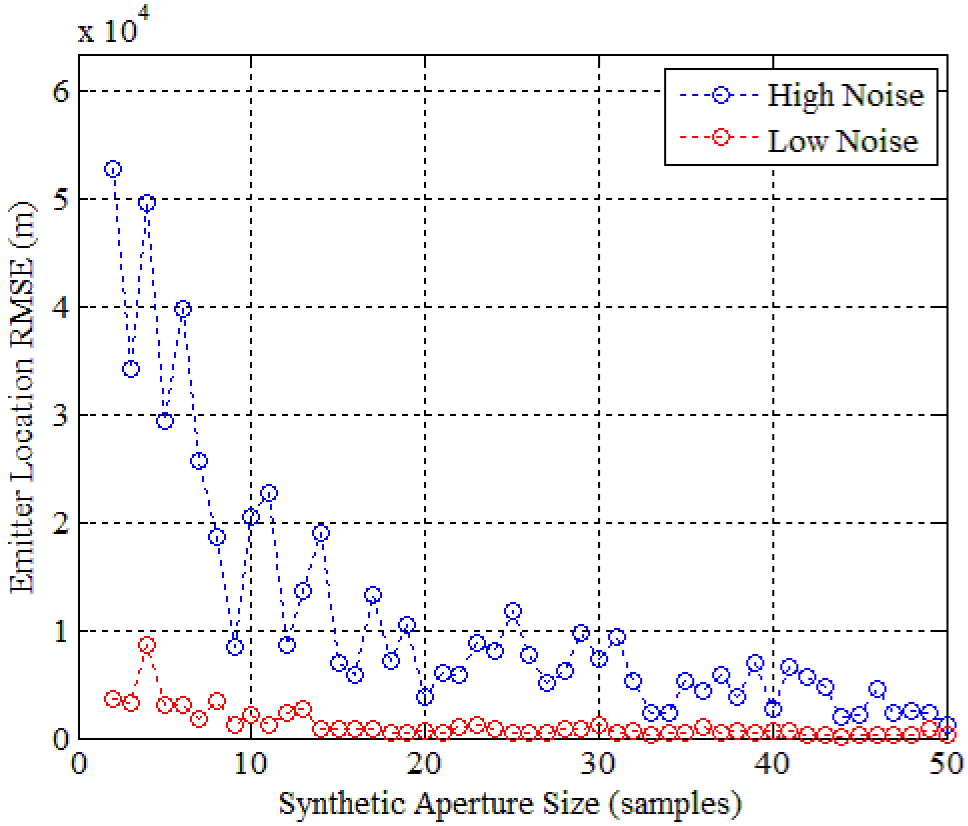

Figure 30. RMSE is plotted against synthetic aperture size N for satellite sensors. Dashed traces are linear interpolations between adjacent data points.

As when we plotted the RMSE versus spread angle, we must mention the very large amplitude RMSE observed when using satellite sensors. For the sake of brevity, we will not reiterate the discussion on mitigating noise effects using time delay variation compensation techniques. Instead, let us highlight the overall trend clearly seen with increasing synthetic aperture size. For the high-noise condition, we observe a minimum RMSE of 1166 m for $N = 50$; for the low-noise condition, the minimum RMSE is 125.8 m for $N = 44$. On the whole, a larger synthetic aperture corresponds to lower RMSE and a better emitter location estimate. Intuitively, this makes sense. If we collect more data concerning a random process within a given time interval, the refined aggregate estimate should improve. There are some small-scale deviations from this overall trend; however, due to the small number of iterations, we do not recommend significant conclusions be drawn from such small-scale variations. Significantly more than ten iterations of the program are necessary before drawing small-scale inferences from the data. Still, the overall trend seems valid.

b. UAV Sensors

The RMSE for the synthetic aperture TOA algorithm applied to UAV sensors is plotted against synthetic aperture size N in Figure 31. Minimum RMSE values of 55.8 m ($N = 16$) and 2.89 m ($N = 29$) were observed for the high- and low-noise conditions, respectively. The most notable feature of these results is the anomalous trend seen for the high-noise condition, namely that the RMSE seems to increase with the synthetic aperture size beyond the local minimum at $N = 16$. This is certainly a counterintuitive finding, especially since the trend is reversed for the low-noise condition. It appears that for low-altitude UAV sensors, increasing the synthetic aperture size allows a more significant degradation of the emitter location estimate due to high noise. We speculate that there is a point of diminishing return with the synthetic aperture principle. If, for a given altitude, the time delay variation is below a certain threshold standard deviation value, the synthetic aperture algorithm will indeed improve the estimate (see the low-noise data). Alternatively, if the time delay variation exceeds that standard deviation threshold, it seems that increasing the number of aperture samples actually degrades the accuracy of the emitter location estimate. Granted, these RMSE results are approximations based on ten iterations, and a program with a larger sample size will reveal the true theoretical trend for RMSE versus aperture size. Still, we conclude that this is a very significant result.

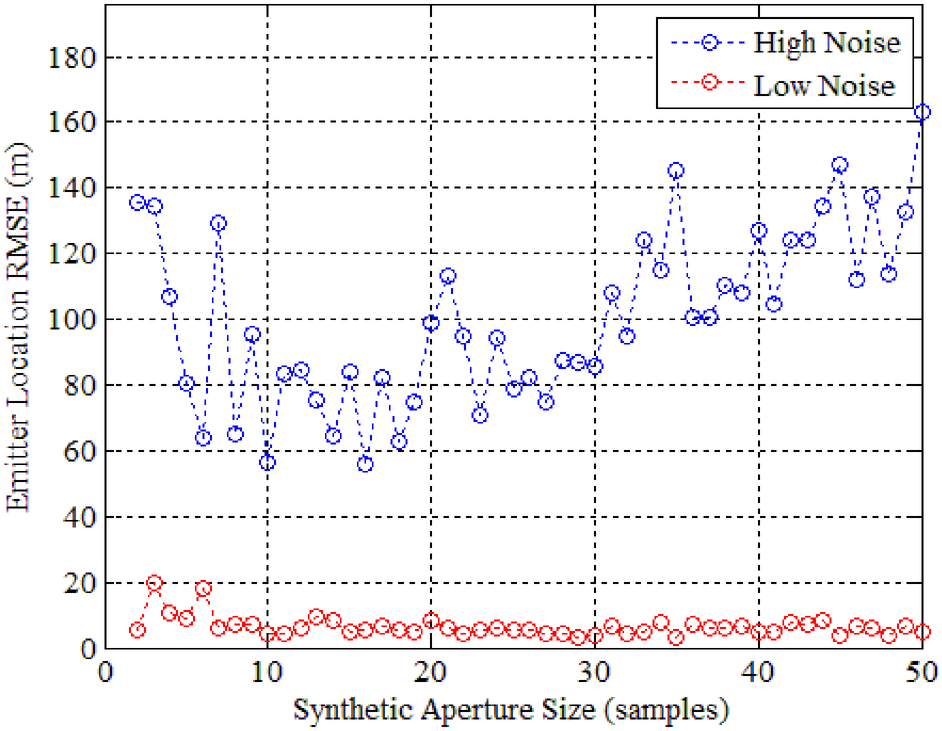

Figure 31. RMSE is plotted against synthetic aperture size N for UAV sensors. Dashed traces are linear interpolations between adjacent data points.

D. SUMMARY

Overall, the synthetic aperture concept was successful in enabling geolocation estimates to be formed using only two airborne sensors. For satellite sensors, future implementations of this synthetic aperture TOA algorithm require some form of time delay variation compensation techniques in order to deliver results with a useful degree of accuracy. For UAV sensors, the RMSE performance under low-noise conditions was quite acceptable. Overall, the system accuracy tends to improve when the sensors travel with a spread angle near $\alpha = 90°$, with the curious anomaly of high-performance with parallel sensor motion. For normal to low noise conditions, increasing the number of aperture samples N results in improved RMSE performance. An interesting exception to this trend arose for high-noise conditions with UAV sensors. Here, it seems that increasing the number of aperture samples actually worsened the emitter location estimate.

VII. SYNTHETIC APERTURE: TDOA-FDOA FUSION

A. OVERVIEW

With the TOA algorithm, the three-dimensional intersection curve of two emitter surfaces at a given time is always a circle that may be parametrically defined. When we move to consider the fusion of one TDOA and one FDOA emitter surface at a given time, we are not so fortunate as to have a simply-defined analytical solution. Recall that for TOA, we generate one emitter surface per sensor, whereas for TDOA and FDOA, we only generate one emitter surface per two sensors. As such, with two airborne sensors equipped with TDOA and FDOA systems, we can calculate a maximum of two emitter surfaces at any given point in time. The TDOA governing equation (see Equation 2) and the FDOA governing equation (see Equation 41) are very difficult to combine. Most of this difficulty arrives from the complexity of the three-dimensional FDOA emitter surface. With TDOA, the solution is always one half of a hyperboloid of two sheets; this is relatively simple to define analytically. Unfortunately, the FDOA surface is defined by the solution to a first-order differential equation; the governing FDOA equation relates the difference in arriving frequency with the vector forms of each sensor velocity—the first-order derivative of the sensor position. The practical consequence is that we require a very different solution strategy for the synthetic aperture TDOA-FDOA fusion algorithm than was used for the synthetic aperture TOA algorithm.

B. SOLUTION STRATEGY

Since an analytical solution is too complicated, an exhaustive search solution is selected as an alternative. Whereas the parametric TOA solution considers the discretized geolocation solution curve derived from the TOA measurements and calculates the spatial coordinates of the estimate, this TDOA-FDOA fusion solution considers a discretized region of spatial coordinates and determines which coordinates best satisfy the geolocation measurements. This strategy may be seen as iteratively reverse-engineering the problem.

1. Bounding Box Definition

To begin, we select a region of three-dimensional space where we expect the emitter to be located. For the sake of computational implementation and simplicity, consider this region to be a cubic volume centered around the initial seed coordinates $S(x_S, y_S, z_S)$ with side length equal to $2g$. We shall iteratively search this volume to find the most-likely emitter location. Since this region is cubic, it shall be referred to as the algorithm's bounding box. A basic diagram of the bounding box is given in Figure 32 when the point of origin is selected for the seed coordinates.

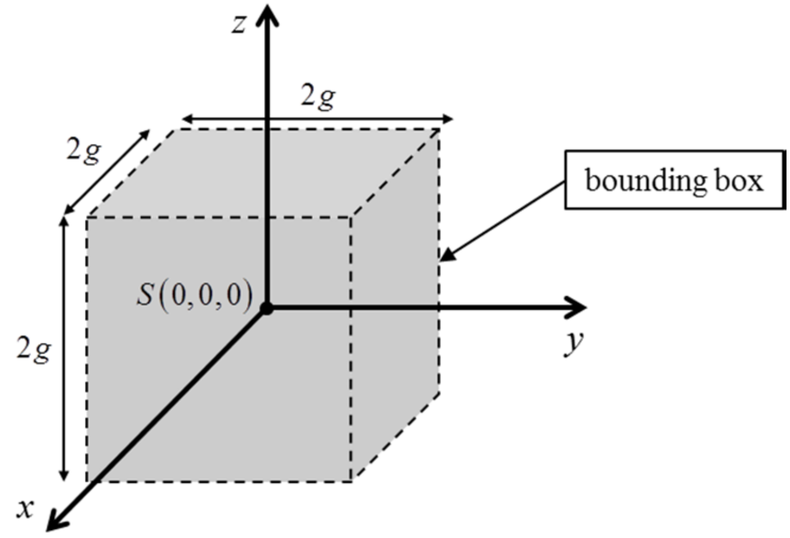

Figure 32. A bounding box is centered about the coordinate system origin.

2. Discretization Technique

Next, the bounding box is discretized into a three-dimensional constellation of sample points. For this algorithm, we apply a uniform sampling density function, meaning we sample the bounding box in each dimension with K points at a constant spatial interval equal to $(2g)/(K-1)$. The result is a uniformly-dense constellation consisting of K^3 total sample points. We map the coordinates (x, y, z) of each constellation point to a set of matrix indices (i, j, k), where i, j, and k are bounded on the range $[1, K]$.

3. TDOA and FDOA Metric

The algorithm then iterates through each point in the bounding box matrix for each time step. For each sample point, we compute the TDOA and FDOA values that would theoretically be received by sensors s_1 and s_2 if an emitter were located at that point. The result is two $K \times K \times K$ matrices of TDOA and FDOA measurements. We then apply a normalized Gaussian metric to each of these matrices. Based upon the TDOA measurement matrix M_T, we populate the TDOA metric matrix $\tilde{M}_T$ for all indices (i, j, k):

$$\tilde{M}_T(i, j, k) = \exp\left[\frac{-\left(M_T(i, j, k) - \tau_{21}\right)^2}{2\left(\sigma_{TDOA}\right)^2}\right], \tag{114}$$

where τ_{21} is the actual received noisy TDOA measurement and σ_{TDOA} is an empirically-defined parameter. The metric is thus bounded in the range $(0, 1]$. For a relatively small σ_{TDOA} value, the metric value falls off rapidly toward zero as $M_T(i, j, k)$ deviates from the TDOA measurement τ_{21}. Conversely, a relatively large σ_{TDOA} value assigns metric values close to unity even for substantial deviations of $M_T(i, j, k)$ from τ_{21}. In this algorithm, we select

$$\sigma_{TDOA} = \left(\frac{1}{20}\right)\left[\max(M_T) - \min(M_T)\right]. \tag{115}$$

The $1/20$ factor is a tunable decision parameter. For applications with a fine spatial sampling interval, a smaller factor $(< 1/20)$ is recommended and vice versa for applications with coarse sampling.

A similar metric matrix $\tilde{M}_F$ is populated based on the FDOA measurement matrix M_F as a function of indices (i, j, k):

$$\tilde{M}_F(i,j,k) = \exp\left[\frac{-\left(M_F(i,j,k) - \Delta f_{21}\right)^2}{2\left(\sigma_{FDOA}\right)^2}\right], \tag{116}$$

where Δf_{21} is the received noisy FDOA measurement and σ_{FDOA} is chosen to be

$$\sigma_{FDOA} = \left(\frac{1}{20}\right)\left[\max\left(M_F\right) - \min\left(M_F\right)\right]. \tag{117}$$

Each element in the FDOA metric matrix $\tilde{M}_F$ is bounded on the range $\left(0,1\right]$.

A composite metric $\tilde{M}_n$ is defined as the sum of the TDOA and FDOA metrics for a given time step n. Over a total of N synthetic aperture samples, we express the aggregate composite metric as

$$\tilde{M} = \sum_{n=1}^{N} \tilde{M}_n = \sum_{n=1}^{N} \left(\tilde{M}_{T,n} + \tilde{M}_{F,n}\right). \tag{118}$$

Preserving our double-primed notation from Chapter VI, the estimated emitter position is chosen to be the coordinates $\left(x'', y'', z''\right)$ that are mapped to the matrix indices $\left(i'', j'', k''\right)$ at which the aggregate composite metric is maximized. Mathematically, the estimated emitter position vector $\boldsymbol{r}_e'' = x''\hat{\boldsymbol{x}} + y''\hat{\boldsymbol{y}} + z''\hat{\boldsymbol{z}}$ is chosen such that

$$\tilde{M}\left(i'', j'', k''\right) = \max\left[\tilde{M}\left(i, j, k\right)\right]. \tag{119}$$

4. RMS Error

For the synthetic aperture TDOA-FDOA fusion algorithm, we again use the RMSE as our performance metric. The RMSE is defined identically as in Equations (106)-(109) in Chapter VI regarding the synthetic aperture TOA algorithm. To avoid redundancy, we shall not repeat the same discussion.

C. RESULTS

The following results are generated based on the same scenario as considered in Chapter VI, with the following modifications. The stationary emitter e generates a combined TDOA and FDOA beacon signal that is received by the sensors s_1 and s_2, which both are equipped with TDOA and FDOA receiver systems. The TDOA measurement is randomly affected according to a time delay standard deviation $\sqrt{2}\sigma_{\tau 21}$. Additionally, the deterministic FDOA measurement is affected by additive zero-mean Gaussian noise with standard deviation $\sqrt{2}\sigma_{\delta f}$, as discussed in Chapter V.

1. Sensor Velocity Angular Spread

For RMSE simulations against the sensor velocity angular spread α, we vary the sensor velocity $\boldsymbol{v}_2$ as detailed in our Chapter VI discussion. The primary difference between the TOA and TDOA-FDOA algorithms here is that we do not use the maximum altitude $h_{\max}$ constraint. Instead, the TDOA-FDAO search requires delineation of the bounding box defined in terms of the seed coordinates $S(x_S, y_S, z_S)$ and the side half-length g. For low-noise trials, we use 25% of the high-noise g value listed in Table 3, since it is assumed that the low-noise TDOA and FDOA measurements are more accurate. We thus limit the search to a smaller region to boost resolution. Pertinent simulation parameters are listed in Table 3 for both satellite and UAV sensors.

Table 3. Angular spread simulation parameters are given for the synthetic aperture TDOA-FDOA fusion algorithm.

Parameter (units)	**Satellite Sensors**	**UAV Sensors**
h (m)	19.10×10^{6}	3.048×10^{3}
v_s (m/s)	3.889×10^{3}	51.44
α (degrees)	variable on [0,90]	variable on [0,90]
N (samples)	5	5
ΔT_{SA} (s)	225	2.72
b (m)	1.750×10^{6}	280.1
Δb (m)	1000	100
$\sigma_{\tau 21}$ (ns)	9.11	10.0
$\sigma_{\delta f}$ (Hz)	1.371	0.412
$S(x_S, y_S, z_S)$ (m)	$(0,0,0)$	$(0,0,0)$
g (m)	4×10^{5}	2×10^{3}
K (samples)	151	151

The values selected for g in these trials were chosen based on the order of magnitude of the RMSE observed for similar TOA simulations (see Chapter VI, Section C). If a tracking algorithm is implemented along with this system that is able to predict future emitter position and if it is known that the emitter is in a smaller region, the bounding box specified by half side-length g may be reduced in size. As well, if more computational resources are available, the number of one-dimensional bounding box samples K may also be increased.

a. Satellite Sensors

We have plotted the RMSE of the synthetic aperture TDOA-FDOA fusion algorithm for satellite sensors against sensor velocity spread angle α in Figure 33.

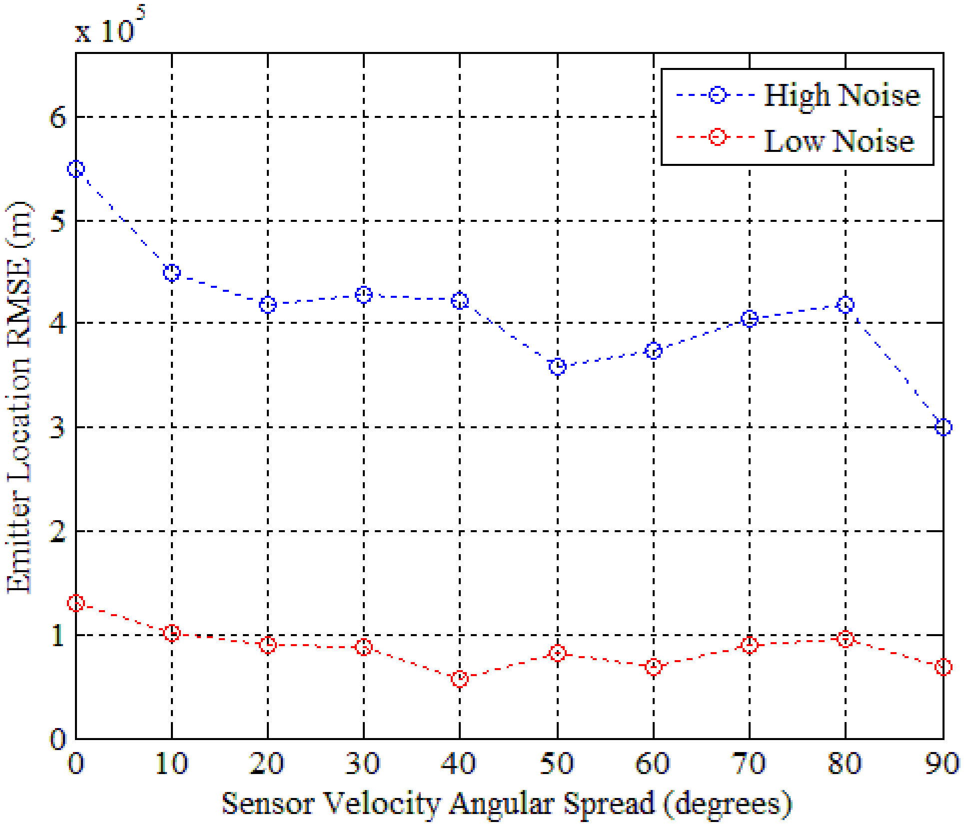

Figure 33. RMSE is plotted against sensor velocity angular spread α for satellite sensors. Dashed traces are linear interpolations between adjacent data points.

Regarding these results, first note that the RMSE for both high-noise and low-noise conditions is similar in magnitude to the associated bounding box side half-length g. Recall that for low-noise, the bounding box is restricted to 25% of the high-noise linear dimension size. This suggests that there is significant variation regarding the emitter estimate within the bounding box with limited accuracy. We attribute this poor performance to the extremely large quantization errors associated with the bounding box search. The spatial sampling interval was set to be $(2g)/(K-1)$ in each dimension. For the satellite sensors that function at extremely high altitudes, the associated bounding box, and thus g, must be very large to accommodate the geometry. As g becomes very large, the spatial sampling interval likewise increases. Similar to the Nyquist sampling criterion in digital communications, if our sampling interval becomes too large, we lose the ability to discern high-frequency variations in the associated data. In this case, as the spatial sampling interval increases, the discretized TDOA and FDOA measurement matrices M_T and M_F lose the ability to discern small-scale variations in the TDOA and FDOA equations. The attendant consequence is that spatial resolution decays. As spatial resolution decreases, this quantization error likely masks any otherwise prominent trends in the data, as is verified by the RMSE measurements presented in Figure 33.

The obvious caveat to this degradation of spatial resolution is that we may increase the number of sample points K to counteract the effects of a large bounding box. The practical drawback is that the iterative synthetic aperture algorithm execution time is on the order of $O\left(NK^3\right)$; we exhaustively compute the associated M_T and M_F matrix values for each of K^3 matrix entries and then iterate the process for each of the N synthetic aperture samples. In short, the computation time is prohibitive for high-resolution searches of large bounding boxes. Note that for this simulation, K was chosen as 151. This may seem curiously small, but consider that the simulation was run within a shell script which iterates the algorithm for ten different spread angles, each of which is iterated ten times to compute approximate the RMSE value. Altogether, it required over seven hours of computation time to generate each of the high-noise and low-noise data sets in Figure 33. We see here an immediate problem with a non-analytical solution strategy for large-scale geolocation problems; the computation time rapidly becomes the primary limiting factor. Some potential improvements on this point are discussed below following the data presentation.

The significant impact of the quantization error on these results tempers the conclusions that might be drawn from the data regarding the impact of sensor velocity spread angle. Still, though mitigated in its accuracy, we see a similar trend as with the synthetic aperture TOA algorithm. There is slight improvement in RMSE performance as the spread angle closes toward $\alpha = 90°$.

b. UAV Sensors

The UAV sensor results for the similar case of RMSE as a function of spread angle is given in Figure 34.

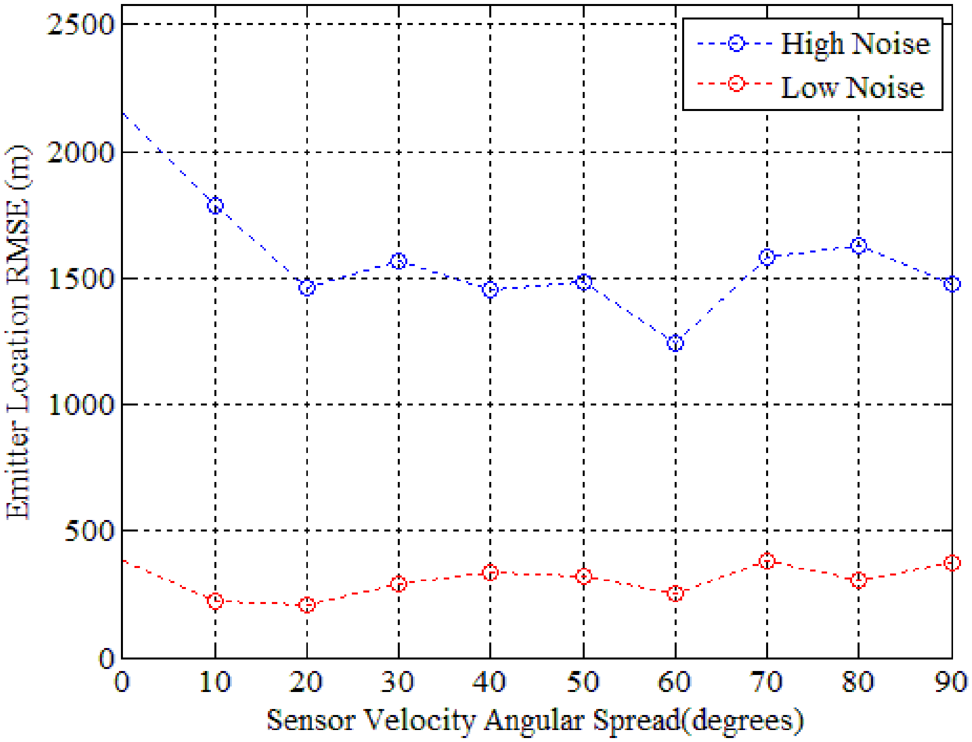

Figure 34. RMSE is plotted against sensor velocity angular spread α for UAV sensors. Dashed traces are linear interpolations between adjacent data points.

With a smaller system geometry, we note that with UAV sensors the RMSE data falls further below the g threshold (2,000 m for high-noise and 500 m for low-noise). For the low-noise condition, we see a minimum RMSE of 210.8 m at the spread angle of $\alpha = 20°$; this is less than 50% of the bounding box side half-length and suggests that the algorithm is indeed gaining some information on the location of the emitter within the bounding box. This is an encouraging result, yet the algorithm is still seriously limited by the spatial resolution of the bounding box. Unfortunately, the data does not show significant trends relating to sensor velocity spread angle α. We hesitate to draw further conclusions based on small-scale variations due to our sampling error.

2. Aperture Size

Here again, we assess the algorithm performance against the synthetic aperture size N as detailed in Chapter VI. We vary the synthetic aperture time interval ΔT_{SA} in accordance with N to maintain a constant swath angle. All pertinent simulation parameters used to generate the following results are presented in Table 4.

Table 4. Aperture size simulation parameters are given for the synthetic aperture TDOA-FDOA fusion algorithm.

Parameter (units)	Satellite Sensors	UAV Sensors
h (m)	19.10×10^6	3.048×10^3
v_s (m/s)	3.889×10^3	51.44
α (degrees)	45	45
$N_{\max}$ (samples)	15	15
N (samples)	variable on [2,15]	variable on [2,15]
$\Delta T_{SA,\min}$ (s)	64.3	0.778
b (m)	1.750×10^6	280.1
Δb (m)	1000	100
$\sigma_{\tau 21}$ (ns)	9.11	10.0
$\sigma_{\delta f}$ (Hz)	1.371	0.412
$S(x_S, y_S, z_S)$ (m)	$(0,0,0)$	$(0,0,0)$
g (m)	4×10^5	2×10^3
K (samples)	151	151

a. Satellite Sensors

As with the satellite sensor RMSE results as a function of spread angle, the data for RMSE versus synthetic aperture size presented in Figure 35 is dominated by quantization error due to sampling and computational resource limitations. For a point of reference, the total execution time for each of the high- and low-noise data sets shown in Figure 35 was over 16 hours. Accordingly, we do not see the appreciable improvement in estimate accuracy that was achieved for the analogous case with the synthetic aperture TOA algorithm (see Figure 30). Still, there are interesting features in the data that merit discussion.

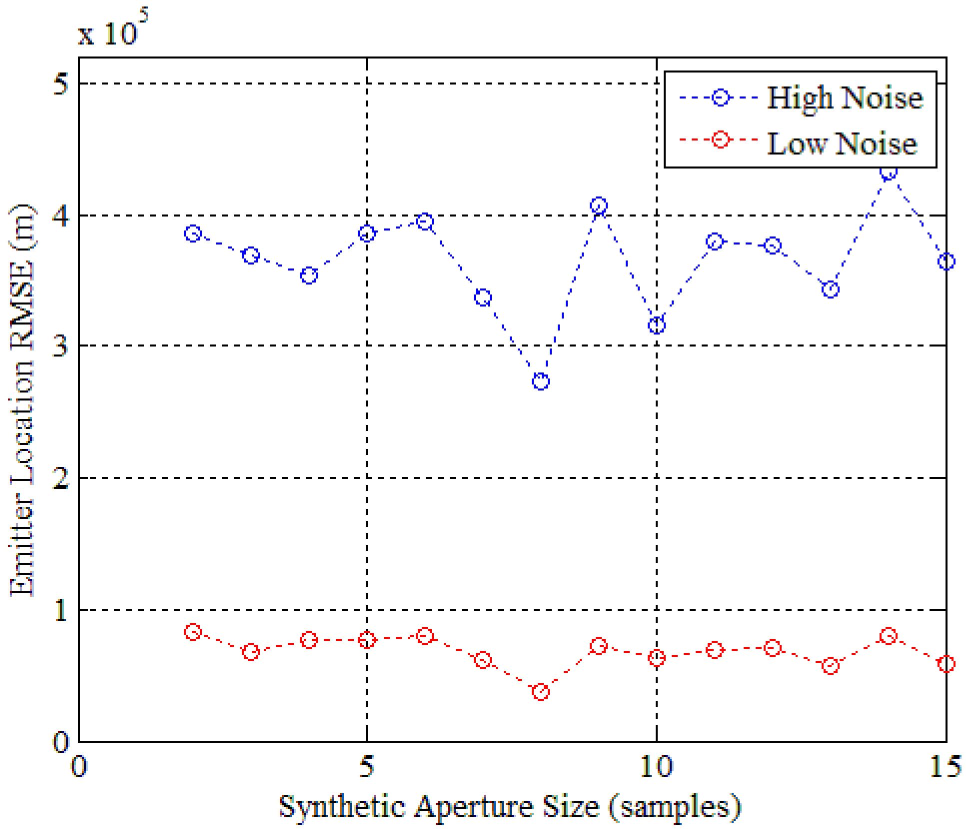

Figure 35. RMSE is plotted against synthetic aperture size N for satellite sensors. Dashed traces are linear interpolations between adjacent data points.

Note the nearly point-for-point match in trend between the low-noise and high-noise data sets. We observe local maxima at $N = 2, 6, 9$, and 14 and local minima at

$N = 8,10,13,$ and 15. Intuitively, we expect the RMSE to monotonically decrease for larger N; as we include more data in the synthetic aperture, the estimate accuracy should improve. Since all data was collected based on a series of independent trials, we cannot easily attribute this repeated oscillatory behavior to stochastic causes. Rather, we speculate that this predictability is a vestige of quantization errors associated with the discrete search algorithm. Since the emitter estimate is chosen from a finite set of spatial coordinates within the bounding box, some of the small-scale random nature of the noisy TDOA and FDOA measurements is absorbed by the rounding process associated with quantization.

b. UAV Sensors

The RMSE results for UAV sensors are plotted against the aperture size in Figure 36.

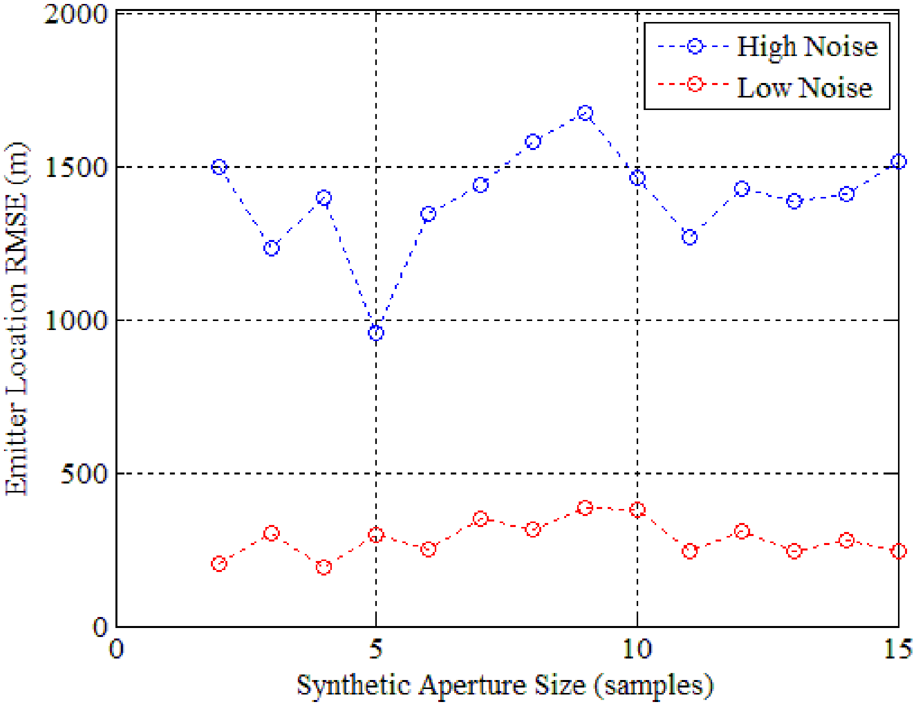

Figure 36. RMSE is plotted against synthetic aperture size N for UAV sensors. Dashed traces are linear interpolations between adjacent data points.

Here, as before, we see some improvement in the RMSE as compared with the bounding box side half-length g; however, the overall absence of a discernable trend suggests minimal correlation between the RMSE and aperture size for the algorithm as described in this chapter. We had expected to see some improvement with larger aperture size, as was seen for the low-noise UAV sensor scenario with the synthetic aperture TOA algorithm. Unfortunately, the sampling limitations likely masked any such trends. The primary implication to draw from these TDOA-FDOA fusion results is that the sampling constraints must be addressed if the algorithm performance is to be refined to a practical level.

D. POTENTIAL IMPROVEMENTS

To that end, we offer some ideas for potential improvements of the TDOA-FDOA fusion algorithm that we could not implement for want of time. One technique would be to manipulate the quantization method used on the bounding box to group more samples near the seed coordinates $S(x_S, y_S, z_S)$ and fewer near the perimeter of the box. If the seed value is near the emitter, this will boost the spatial resolution of the iterative search in the local region surrounding the seed. This effectively focuses the samples within a subregion of the bounding box. The drawback to this technique is if the seed coordinate is far from the true emitter position, the sample density surrounding the emitter may actually become sparser than with a uniform sample density. Such a sample density is given as a red trace in Figure 37. For comparison, the uniform sample density used in the above model is given as a black trace.

A more sophisticated alternative is to use an adaptive sampling technique that dynamically redefines the sampling density function at each time step in the aperture. Based on received measurements, the algorithm might focus the sample density on different regions of the bounding box. Such a technique may improve the spatial resolution and mitigate quantization errors, but it alone will not reduce the computational demands of the iterative search algorithm.

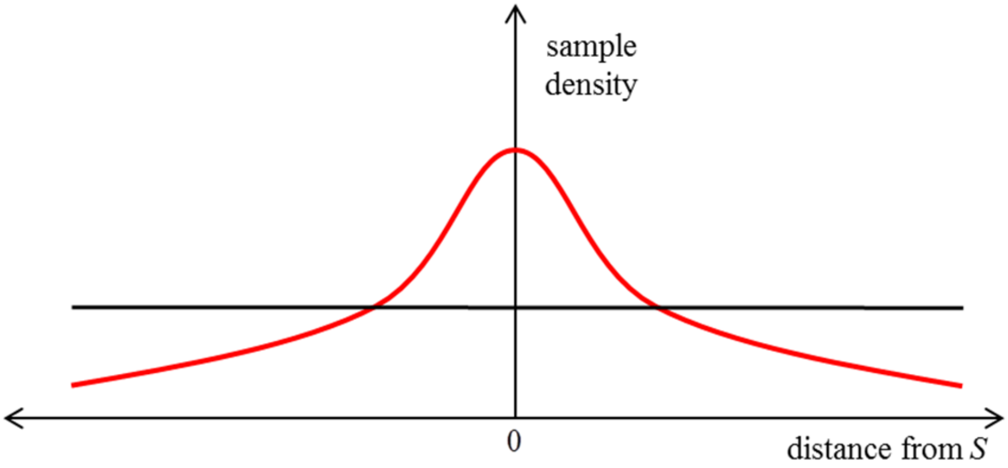

Figure 37. A manipulated sample density function (red trace) condenses more samples near the seed coordinates than a uniform density function (black trace).

A second possible improvement is to implement an adaptive telescopic zoom that progressively tightens the bounding box to a smaller and smaller region of interest. With each telescopic iteration, the spatial resolution of the algorithm improves. A two-dimensional illustration of such an algorithm is given in Figure 38. For each iteration in this example, the algorithm selects a subregion with 1/9 the total area of the current bounding box. Still, this does not ease the demand on computational resources.

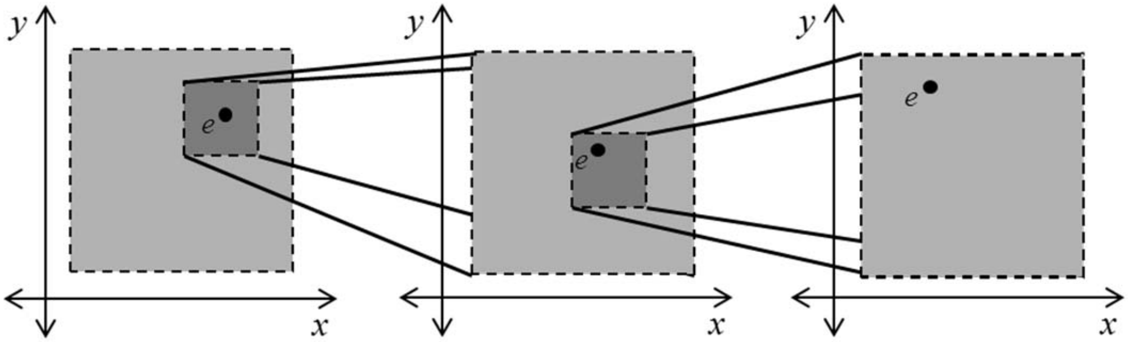

Figure 38. An adaptive zoom technique iteratively reduces the size of the bounding box.

To improve the algorithm in regards to execution time, an effort must be made to apply loop-flattening techniques. A program with execution time on the order of

$O\left(NK^3\right)$ is extremely difficult to scale. If some inherent matrix operations native to the MATLAB® software library that was used in this research can be applied to flatten one of the internal loops of the iterative search, the runtime might be reduced to the order of $O\left(NK^2\right)$. This would likely yield significant reduction in runtime, allowing smaller sampling intervals and better spatial resolution. In broad terms, the algorithm's computational efficiency must be improved, regardless of other modifications, if it is to be implemented as a viable real-time geolocation algorithm.

E. SUMMARY

Unlike the synthetic aperture TOA algorithm, we did not consider an analytical solution to the synthetic aperture TDOA-FDOA fusion problem. Rather, we adopted an exhaustive search solution strategy within a certain bounding box region. Results from our simulations suggested that the quantization errors associated with our sampling constraints were too large to yield useful results for high-accuracy geolocation. As a result, we offered several options for future improvements to the algorithm to help overcome the limitations due to excessive execution times. Altogether, the complicated nature of the TDOA and FDOA geolocation equations necessitated a computationally-intensive solution strategy which exhausted our computational resources before the algorithm could converge to a useful solution.

VIII. CONCLUSION

A. RESEARCH CONTRIBUTIONS

The initial goal of this research was to investigate the feasibility of two-sensor synthetic aperture geolocation techniques. The driving motivation was to reduce the physical resource requirements for successful geolocation from three or four airborne sensors down to only two. We speculated that the use of a synthetic aperture principle similar to that used in radar, sonar, and medical imaging, might be helpful. To begin, we laid the groundwork of establishing the theoretical two- and three-dimensional solutions for the TOA, TDOA, and FDOA geolocation methods. When possible, analytical solutions were given to define the emitter curves and surfaces resulting from a given geolocation estimate.

Subsequently, three separate noise models were developed for TOA, TDOA, and FDOA measurements for two distinct cases. First, time delay and Doppler shift variation parameters were determined based on the assumption that ionospheric signal degradation was the primary mechanism of TOA, TDOA, and FDOA measurement variation about the deterministic value calculated based on the geometry of the problem. Ionospheric forecast models and measurements were considered in the determination of the noise parameters. Second, time delay and Doppler shift variation parameters were estimated for a geolocation system onboard a UAV. We turned to literature resources to estimate the time delay standard deviation and assumed that the Doppler shift variation in the lower atmosphere would mainly result from instrumental uncertainties rather than the nonlinearity or inhomogeneity of the propagation medium. Together, these parameters contributed to a basic noise model for incorporation in our later simulations.

Regarding the heart of our work—the synthetic aperture algorithms—we first investigated the homogenous algorithm consisting of two TOA measurements per time step in the synthetic aperture. Using a parametric solution strategy to find the intersection points of subsequent TOA emitter circles, we found that the algorithm requires some form of time delay variation compensation to function with reasonable accuracy for satellite sensors. Conversely, for UAV sensors the algorithm has promising levels of accuracy, especially in low-noise environments. A primary finding is that the RMSE of the emitter estimate tended to decrease with increasing synthetic aperture size, except perhaps for particularly high noise levels relative to the system geometry. This helped validate the general principle of using a synthetic aperture in time to refine the final emitter location estimate.

Applying the synthetic aperture concept to a heterogeneous combination of TDOA and FDOA measurements was far more challenging from a solution strategy perspective. We were forced to consider an exhaustive search solution strategy in lieu of a straightforward analytical solution as for TOA. The results collected from our simulations highlighted the practical limitations of an exhaustive search in three-dimensions; the computation time required to search a large spatial region with fine resolution can rapidly become unmanageable. We are thus faced with a trade-off between computation time and spatial resolution of the algorithm. More focused research is required in this area before the synthetic aperture TDOA-FDOA algorithm can be useful in real-time applications.

On the whole, we recommend use of the synthetic aperture TOA algorithm for use with small-scale UAV geolocation networks. The mathematical solution for the homogeneous TOA problem is a distinct advantage over the heterogeneous TDOA-FDOA problem. Yet, if the issues related to sampling intervals in the TDOA-FDOA algorithm can be solved or mitigated, then it may be found to have advantages over the TOA algorithm with respect to RMSE performance as a function of sensor spatial orientation or other system variables.

B. OPPORTUNITIES FOR FUTURE WORK

In broad terms, the foreseeable opportunities for future work on this two-sensor synthetic aperture geolocation problem may be grouped into three categories. First, a more robust consideration of noise effects and associated noise mitigation techniques will be helpful. Second, the proposed algorithms offered in this work are heuristic in nature; work should be directed toward developing optimal estimators for the TOA and TDOA-

FDOA cases. Third, more concentrated research should be directed toward determining optimal synthetic aperture configuration. Other opportunities for further work do exist, but we have tried to highlight those most prominent areas.

1. Noise Effects and Mitigation

Although reasonable for initial consideration, the treatment given to noise modeling in Chapter V was simplistic. It is unlikely that all atmospheric effects on a geolocation signal can be folded into one single random variable with a high degree of fidelity. Modifying the time delay noise models to include more generalized PDFs such as the Rayleigh, Rician, and lognormal distributions may offer a more robust time-domain model. Experimental data should be collected to help validate such models.

Certainly, work should be done to incorporate the available ionospheric forecast models into geolocation systems. Based on the latitude, longitude, and time of day, we can much more accurately predict the time delay and Doppler shift associated with ionospheric propagation for satellite-based systems. Moreover, we might consider out-of-band signaling with known ground stations to sample the channel. Depending on the real-time channel condition, appropriate compensations may be incorporated into the emitter estimation algorithm. All this is in an effort to reduce the degree of randomness associated with the propagation of an emitter's beacon signal.

2. Optimal Estimators

As previously mentioned, the heuristic algorithms presented herein are not optimal. That is, they have not been compared against the CRLB. For resources concerning optimal estimators, see [35] and [36]. Optimization research directed toward finding an efficient estimator for both the synthetic aperture TOA and TDOA-FDOA problems may give further insight into methods to refine the computational efficiency of these algorithms. In practical terms, the crux of the issue is being able to implement a synthetic aperture algorithm in a real-time system that boasts high spatial resolution and manageable computation time.

3. Optimal Synthetic Aperture Configuration

Moving forward with the synthetic aperture geolocation concept, we must determine what sensor orientation, velocity angle, swath angle, and aperture sample size achieve optimal results for both the TOA and TDOA-FDOA algorithms. Our results showed notable variation in system performance with each of these variables; the next step is to find an optimal set of all variables to achieve the most consistent, accurate systems performance. This information will guide the implementation tactics of any future synthetic aperture geolocation system and, as such, is a significant next step in the development process.

APPENDIX. MISCELLANEOUS DERIVATIONS

A. THREE-DIMENSIONAL TDOA EQUATION

The following derivation follows very closely that given in Chapter III for the two-dimensional TDOA solution, which is in turn based on the proof given in [16]. Let us begin by restating the governing TDOA equation:

$$\|\boldsymbol{r}_e-\boldsymbol{r}_2\|-\|\boldsymbol{r}_e-\boldsymbol{r}_1\|=c_0\tau_{21}. \tag{120}$$

Expressing this vector equation in terms of its Cartesian components, we have

$$\sqrt{\left(x-x_2\right)^2+\left(y-y_2\right)^2+\left(z-z_2\right)^2}-\sqrt{\left(x-x_1\right)^2+\left(y-y_1\right)^2+\left(z-z_1\right)^2}=c_0\tau_{21}, \tag{121}$$

where the two sensors s_1 and s_2 are located at the generic positions $\left(x_1,y_1,z_1\right)$ and $\left(x_2,y_2,z_2\right)$. For the specific case when sensors s_1 and s_2 are positioned at coordinates $\left(-d,0,0\right)$ and $\left(d,0,0\right)$, we have

$$\sqrt{\left(x-d\right)^2+y^2+z^2}-\sqrt{\left(x+d\right)^2+y^2+z^2}=c_0\tau_{21}. \tag{122}$$

Rearranging and squaring gives

$$\left(\sqrt{\left(x-d\right)^2+y^2+z^2}\right)^2=\left(c_0\tau_{21}+\sqrt{\left(x+d\right)^2+y^2+z^2}\right)^2. \tag{123}$$

Expanding both sides fully gives

$$\begin{aligned}&x^2-2dx+d^2+y^2+z^2\\&\qquad=\left(c_0\tau_{21}\right)^2+2c_0\tau_{21}\sqrt{x^2+2dx+d^2+y^2+z^2}+x^2+2dx+d^2+y^2+z^2.\end{aligned} \tag{124}$$

We cancel terms and rearrange to get

$$-4dx-\left(c_0\tau_{21}\right)^2=2\left(c_0\tau_{21}\right)\sqrt{x^2+2dx+d^2+y^2+z^2}. \tag{125}$$

In terms of the parameter $a=c_0\tau_{21}/2$, (125) simplifies to

$$-dx-a^2=a\sqrt{x^2+2dx+d^2+y^2+z^2}. \tag{126}$$

We square to get

$$d^2x^2 + 2da^2x + a^4 = a^2\left(x^2 + 2dx + d^2 + y^2 + z^2\right). \tag{127}$$

Collecting terms and factoring leaves

$$\left(d^2 - a^2\right)x^2 - a^2y^2 - a^2z^2 = a^2\left(d^2 - a^2\right). \tag{128}$$

Dividing through by $a^2\left(d^2 - a^2\right)$ leaves

$$\frac{x^2}{a^2} - \frac{y^2}{d^2 - a^2} - \frac{z^2}{d^2 - a^2} = 1. \tag{129}$$

From here, the equation may be cast in terms of the traditional hyperbolic parameter $b = \sqrt{d^2 - a^2}$ to give

$$\frac{x^2}{a^2} - \frac{y^2}{b^2} - \frac{z^2}{b^2} = 1, \tag{130}$$

or we may substitute out the intermediate parameter a to give the final three-dimensional hyperboloidal TDOA equation

$$\frac{4x^2}{\left(c_0\tau_{21}\right)^2} - \frac{4y^2}{4d^2 - \left(c_0\tau_{21}\right)^2} - \frac{4z^2}{4d^2 - \left(c_0\tau_{21}\right)^2} = 1. \tag{131}$$

B. PARAMETERIZING A CIRCLE: ORTHOGONAL UNIT VECTORS

Two orthogonal unit vectors $\hat{\boldsymbol{u}}$ and $\hat{\boldsymbol{r}}_{21}$ are known to satisfy the dot-product criterion

$$\hat{\boldsymbol{u}} \cdot \hat{\boldsymbol{r}}_{21} = \left(\hat{u}_x\hat{\boldsymbol{x}} + \hat{u}_y\hat{\boldsymbol{y}} + 0\hat{\boldsymbol{z}}\right) \cdot \left(\hat{r}_{21x}\hat{\boldsymbol{x}} + \hat{r}_{21y}\hat{\boldsymbol{y}} + \hat{r}_{21z}\hat{\boldsymbol{z}}\right) = 0. \tag{132}$$

This implies that unit vector $\hat{\boldsymbol{u}}$ lies entirely within the *x*-*y* plane. Evaluating the dot product gives

$$\hat{u}_x\hat{r}_{21x} + \hat{u}_y\hat{r}_{21y} = 0. \tag{133}$$

Rearranging and squaring gives

$$\hat{u}_x{}^2\hat{r}_{21x}{}^2 = \hat{u}_y{}^2\hat{r}_{21y}{}^2. \tag{134}$$

By virtue of $\hat{\boldsymbol{u}}$ being a unit vector, we know

$$\left\|\hat{\boldsymbol{u}}\right\| = \hat{u}_x{}^2 + \hat{u}_y{}^2 = 1, \tag{135}$$

and thus,

$$\hat{u}_x{}^2 = 1 - \hat{u}_y{}^2. \tag{136}$$

Substituting (136) into (134) gives

$$\left(1 - \hat{u}_y{}^2\right)\hat{r}_{21x}{}^2 = \hat{u}_y{}^2\hat{r}_{21y}{}^2. \tag{137}$$

We then distribute terms and factor to get

$$\hat{r}_{21x}{}^2 = \left(\hat{r}_{21x}{}^2 + \hat{r}_{21y}{}^2\right)\hat{u}_y{}^2. \tag{138}$$

Retaining the root ambiguity, we have

$$\hat{u}_y = \pm\sqrt{\frac{\hat{r}_{21x}{}^2}{\hat{r}_{21x}{}^2 + \hat{r}_{21y}{}^2}}. \tag{139}$$

Equation 133 may be solved solve for $\hat{u}_x$ such that

$$\hat{u}_x = -\left(\frac{\hat{r}_{21y}}{\hat{r}_{21x}}\right)\hat{u}_y = \mp\left(\frac{\hat{r}_{21y}}{\hat{r}_{21x}}\right)\sqrt{\frac{\hat{r}_{21x}{}^2}{\hat{r}_{21x}{}^2 + \hat{r}_{21y}{}^2}} = \mp\sqrt{\frac{\hat{r}_{21y}{}^2}{\hat{r}_{21x}{}^2 + \hat{r}_{21y}{}^2}}. \tag{140}$$

Finally, we may express the unit vector $\hat{\boldsymbol{u}}$ in the three-dimensional Cartesian coordinate system as

$$\hat{\boldsymbol{u}} = \left(\mp\sqrt{\frac{\hat{r}_{21y}{}^2}{\hat{r}_{21x}{}^2 + \hat{r}_{21y}{}^2}}\right)\hat{\boldsymbol{x}} \pm \left(\sqrt{\frac{\hat{r}_{21x}{}^2}{\hat{r}_{21x}{}^2 + \hat{r}_{21y}{}^2}}\right)\hat{\boldsymbol{y}} + (0)\hat{\boldsymbol{z}}. \tag{141}$$

C. SCALED APERTURE INTERVAL FOR CONSTANT SWATH ANGLE

Consider the generalized flat-earth diagram for a single geolocation sensor s_1 at altitude h passing over an emitter e given in Figure 39. The sensor travels at constant speed v_s parallel to the ground. Over the time period T_{SA} associated with the synthetic aperture, the sensor traces out an associated swath angle ψ .

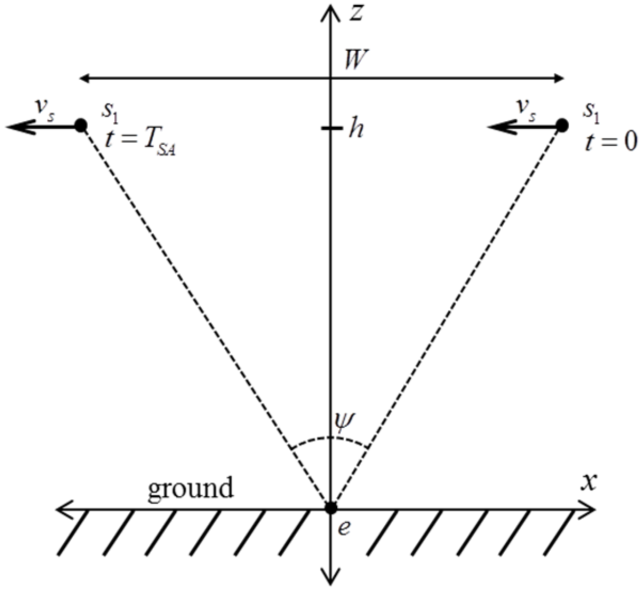

Figure 39. A geolocation sensor traces out a swath angle ψ relative to an emitter.

The length of the aperture traced by the sensor can be written as

$$W = v_s T_{SA}. \tag{142}$$

If the synthetic aperture is composed of N individual, regularly-spaced measurements, then we may write

$$T_{SA} = \left(N - 1\right)\Delta T_{SA}. \tag{143}$$

Substituting (143) into (142) gives

$$W = v_s \left(N - 1\right)\Delta T_{SA}. \tag{144}$$

From basic trigonometric relationships, we see that

$$\tan\left(\frac{\psi}{2}\right) = \frac{W}{2h} = \frac{v_s\left(N-1\right)\Delta T_{SA}}{2h}. \tag{145}$$

We aim to scale the synthetic aperture time interval ΔT_{SA} such that the swath angle is held constant for an arbitrary sensor velocity and altitude. If the swath angle is fixed, (145) is likewise a fixed constant. Accordingly, all scaled values (primed notation) are valid so long as we satisfy

$$\left(\frac{v_s \left(N - 1 \right) \Delta T_{SA}}{h} \right) = \left(\frac{v_s' \left(N' - 1 \right) \Delta T_{SA}'}{h'} \right) = \text{constant.} \tag{146}$$

To specifically scale our aperture time interval for satellite sensors to the appropriate value for UAV sensors, we simply solve for the scaled synthetic aperture time interval:

$$\begin{aligned} \Delta T_{SA}' &= \left[\frac{v_s \left(N - 1 \right)}{v_s' \left(N' - 1 \right)} \right] \left(\frac{h'}{h} \right) \Delta T_{SA} \\ &= \left[\frac{\left(3889 \text{ m/s} \right) \left(5 - 1 \right)}{\left(51.44 \text{ m/s} \right) \left(5 - 1 \right)} \right] \left(\frac{3,048 \text{ m}}{19.10 \times 10^6 \text{ m}} \right) \left(225 \text{ s} \right) \\ &= 2.72 \text{ s}. \end{aligned} \tag{147}$$

THIS PAGE INTENTIONALLY LEFT BLANK

LIST OF REFERENCES

[1] P. L. Massoglia, M. T. Pozesky, and G. T. Germana, “The use of satellite technology for oceanic air traffic control,” in *Proc. IEEE*, vol. 77, no. 11, pp. 1695–1708, Nov. 1989.

[2] R. L. Dowden, J. B. Brundell, and C. J. Rodger, “VLF lightening location by time of group arrival (TOGA) at multiple sites,” in *Journal of Atmospheric and Solar-Terrestrial Physics*, vol. 64, no. 7, pp. 817–830, May 2002.

[3] M. Manzo, P. Berardino, M. Bonano, F. Casu, R. Lanari, A. Manconi, M. Manunta, A. Pepe, S. Pepe, E. Sansosti, G. Solaro, P. Tizzani, and G. Zeni, “Full exploitation of the SBAS-DInSAR algorithm in active seismogenetic scenarios,” in *Proc. IEEE Int. Geoscience and Remote Sensing Symp.*, pp. 1206–1209, July 25–30, 2010.

[4] J. H. Reed, K. J. Krizman, B. D. Woerner, and T. S. Rappaport, “An overview of the challenges and progress in meeting the E-911 requirement for location service,” in *IEEE Communications Mag.*, vol. 36, no. 4, pp. 30–37, Apr. 1998.

[5] A. G. Dempster, “Dilution of precision in angle-of-arrival positioning systems,” in *Electronics Letters*, vol. 42, no. 5, pp. 291–292, Mar. 2006.

[6] C. Gentile, N. Alsindi, R. Raulefs, and C. Teolis, *Geolocation Techniques: Principles and Applications*. New York, NY: Springer, 2013.

[7] D. J. Torrieri, “Statistical theory of passive location systems,” in *IEEE Trans. on Aerospace and Electronics Systems*, vol. AES-20, no. 2, pp. 183–198, Mar. 1984.

[8] D. Musicki and W. Koch, “Geolocation using TDOA and FDOA measurements,” in *Proc. 11th Int. Conf. on Information Fusion*, pp. 1–8, June 30–July 3, 2008.

[9] C. O. Savage, R. L. Cramer, and H. A. Schmitt, “TDOA geolocation with the Unscented Kalman Filter,” in *Proc. IEEE Conf. on Networking, Sensing and Control*, pp. 602–606, Apr. 23–25, 2006.

[10] B. Ristic, S. Arulampalam, and N. Gordon, *Beyond the Kalman Filter: Particle Filters for Tracking Applications*. Boston, MA: Artech House, 2004.

[11] J. A. Cho, H. Na, S. Kim, and C. Ahn, “Moving-target tracking based on particle filter with TDOA/FDOA measurements,” in *ETRI Journal*, vol. 34, no. 2, pp. 260–263, Apr. 2012.

[12] K. C. Ho and Y. T. Chan, “Geolocation of a known altitude object from TDOA and FDOA measurements,” in *IEEE Trans. on Aerospace and Electronic Systems*, vol. 33, no. 3, pp. 770–783, July 1997.

[13] P. Davidson, M. A. Vazquez, and R. Piche, "Uninterrupted portable car navigation system using GPS, map and inertial sensors data," in *Proc. 13th IEEE Symp. on Consumer Electronics*, pp. 836–840, May 25–28, 2009.

[14] F. Fletcher, B. Ristic, and D. Musicki, "Recursive estimation of emitter location using TDOA measurements from two UAVs," in *Proc. 10th Int. Conf. on Information Fusion*, pp. 1–8, July 9–12, 2007.

[15] B. Spain, *Analytical Conics*. New York, NY: Pergamon Press, 1957.

[16] W. S. Rickman. (n.d.). *Proofs for the hyperbola* [Online]. Available: http://www2.seminolestate.edu/srickman/Proofs/Proofs%20for%20the%20hyperbola.pdf.

[17] S. K. Berberian, *Linear Algebra*. Oxford, England: Oxford University Press, 1992.

[18] Community Coordinated Modeling Center. (n.d.). *CCMC Hosted Models at a Glance* [Online]. Available: http://ccmc.gsfc.nasa.gov/models/models_at_glance.php.

[19] H. J. Larson, *Introduction to the Theory of Statistics*. New York, NY: John Wiley & Sons, 1973.

[20] V. K. Garg, *Wireless Communications and Networking*. Amsterdam, Netherlands: Morgan Kaufmann Publishers, 2007.

[21] N. Blaunstein and C. Christodoulou, *Radio Propagation and Adaptive Antennas for Wireless Communication Links: Terrestrial, Atmospheric and Ionospheric*. Hoboken, NJ: John Wiley & Sons, 2007.

[22] C. A. Levis, J. T. Johnson, and F. L. Teixeira, *Radiowave Propagation: Physics and Applications*. Hoboken, NJ: John Wiley & Sons, 2010.

[23] International Civil Aviation Organization. (2005). *Global Navigation Satellite System (GNSS) Manual* [Online]. Available: http://www.icao.int/Meetings/PBN-Symposium/Documents/9849_cons_en[1].pdf.

[24] Dept. of Defense, Dept. of Homeland Security, and Dept. of Transportation. (2012). *Federal Radionavigation Plan* [Online]. Available: http://www.navcen.uscg.gov/pdf/2012_FRP_Final_Signed.pdf.

[25] F. T. Ulaby, E. Michielssen, and U. Ravaioli, *Fundamentals of Applied Electromagnetics, 6th Ed.* Boston, MA: Prentice Hall, 2010.

[26] D. C. Jenn, *Radar and Laser Cross Section Engineering, Second Edition*. Reston, VA: American Institute of Aeronautics and Astronautics, 2005.

[27] Community Coordinated Modeling Center, USU-GAIM. (n.d.). *Runs on Request: Ionosphere/Thermosphere Simulation Results* [Online]. Available: http://ccmc.gsfc.nasa.gov/ungrouped/IT/IT_db.php.

[28] R. S. Lawrence, C. G. Little, and H. J. A. Chivers, "A survey of Ionospheric effects upon Earth-space radio propagation," in *Proc. IEEE*, vol. 52, no. 1, pp. 4–27, Jan. 1964.

[29] J. F. Willman, "Frequency-dependent ionospheric refraction effects on the Doppler shift of satellite signals," in *IEEE Trans. on Aerospace and Electronic Systems*, vol. AES-1, no. 3, pp. 283–289, Dec. 1965.

[30] W. G. Newhall, R. Mostafa, C. Dietrich, C. R. Anderson, K. Dietze, G. Joshi, and J. H. Reed, "Wideband air-to-ground radio channel measurements using an antenna array at 2 GHz for low-altitude operations," in *Proc. IEEE Military Communications Conf.*, vol. 2, pp. 1422–1427, Oct. 13–26, 2003.

[31] C. W. Sherwin, J. P. Ruina, and R. D. Rawcliffe, "Some early developments in synthetic aperture radar systems," in *IRE Trans. on Military Electronics*, vol. MIL-6, no. 2, pp. 111–115, Apr. 1962.

[32] M. P. Hayes and P. T. Gough, "Synthetic aperture sonar: a review of current status," in *IEEE Journal of Oceanic Eng.*, vol. 34, no. 3, pp. 207–224, Jul. 2009.

[33] S. I. Nikolov, J. Kortbek, and J. A. Jensen, "Practical applications of synthetic aperture imaging," in *Proc. IEEE Int. Ultrasonics Symp.*, pp. 350–358, Oct. 11–14, 2010.

[34] J. Feldman. (n.d.). *Parameterizing Circles* [Online]. Available: http://www.math.ubc.ca/~feldman/m317/circle.pdf.

[35] S. M. Kay, *Fundamentals of Statistical Signal Processing: Estimation Theory*. Upper Saddle River, NJ: Prentice Hall PTR, 1993.

[36] S. A. Zekavat and R. M. Buehrer, Eds., *Handbook of Position Location: Theory, Practice, and Advances*. Hoboken, NJ: John Wiley & Sons, 2012.

THIS PAGE INTENTIONALLY LEFT BLANK

INITIAL DISTRIBUTION LIST

1. Defense Technical Information Center
   Ft. Belvoir, Virginia

2. Dudley Knox Library
   Naval Postgraduate School
   Monterey, California